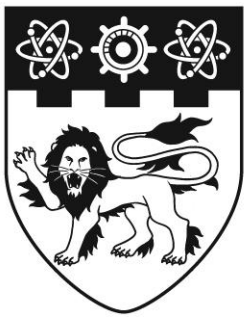

NANYANG TECHNOLOGICAL UNIVERSITY

Cavity QED of Superradiant Phase Transition in Two Dimensional Materials

Li Benliang

School of Electrical & Electronic Engineering

2018

Cavity QED of Superradiant Phase Transition in Two Dimensional Materials

Li Benliang

School of Electrical & Electronic Engineering and

Optoelectronics Research Centre

A thesis submitted to the Nanyang Technological University

and Southampton University in partial fulfillment of the requirements for the

joint degree of Doctor of Philosophy

2018

ACKNOWLEDGEMENT

First and foremost, I'd like to gratefully acknowledge my supervisor Prof. Wang Qijie in Nanyang technological university and my senior colleague Dr. Liu Tao for their patience and insightful guidance along the way. I would also like to thank my supervisor Prof. Dan Hewak in Southampton University for his generous support that made my research life in Southampton University an enjoyable experience; I could not finish the second part in this thesis without all his support.

At last, I'd like to thank my parents, Mr Li Zhentao and Mrs Zhang Xueying, who always stand by me and encourage me to overcome any obstacles in my life.

Table of Contents

Acknowledgement 1
Summary 3
List of Figures 6
1. Introduction 8
1.1 Superradiant Phase Transiton of Single-Mode Dicke Model 9
1.2 Superradiant Phase Transiton of Multi-Mode Dicke Model 11
1.3 Polariton and Ultrstrong Light-Matter Coupling For 2D Electron Gas 12
1.4 Polariton and Superradiant Phase Transition of Graphene in a Cavity 15
1.5 Polarition, Superradiant phase transition and their applications 19
1.6 Summary and Motivation 19
1.7 Thesis Overview 20
2. Polariton and superradiant phase transition in monolayer MoS2 22
2.1 Theoretical Formulations 22
2.2 Numerical Results and Discussions 39
3. cavity qed of black phosphorene 44
3.1 Theoretical Formulations 44
3.2 Numerical Results and Discussions 50
4. multi-mode superradiant phase transition in graphene 53
4.1 Theoretical Formulations 53
4.2 Numerical Results and Discussions 58
5. theoretical study of aharonov-bohm effect from quantum field theory approach 64
5.1 Review of AB Effect From One Particle Quantum Mechanics 64
5.2 Study of AB Effect Based on Quantum Field Theory 67
6. Conclusions 80
Appendix A 81
Appendix B 84
Appendix C 85
Appendix D 89
Publications 95
Bibliography 96

SUMMARY

In modern physics, the investigation of the interaction between light and matter is important from both a fundamental and an applied point of view. Cavity quantum electrodynamics (cavity QED) is the study of the interaction between light confined in a reflective cavity and atoms or other particles where the quantum nature of light photons is significant. The strong interaction between an exciton and cavity photon in a high-finesse microcavity can induce a hybrid light-matter eigenstate which is usually named as polariton in solid-state systems. This strong light-matter interaction can be achieved when this interaction is larger than all broadenings caused by other various factors e.g. electron phonon scattering and cavity loss. The polariton is now stimulating tremendous research interests due to its high potential in cavity quantum electrodynamics (QED) and the achievement of polaritonic devices. Moreover, when the interaction strength between an excitation and the cavity photon, quantified by vacuum Rabi frequency, becomes comparable to or larger than the corresponding electronic transition frequency in a cavity, the system can enter an ultrastrong coupling regime, which has been experimentally observed. In this regime, the standard rotating-wave approximation is no longer valid and the antiresonant term of the interaction Hamiltonian starts to play an important role, giving rise to exciting effects in cavity QED.

The Aharonov-Bohm (AB) effect is a fundamental quantum phenomenon that bears the significance of the nature of electromagnetic fields and potentials. Besides its fundamental significance in quantum theory, its importance for applications in interferometric devices is omnipresent. Recently, since the 2D materials have triggered immense interest, some work has been done to integrate the AB effect with the electronic and transport properties of 2D materials.

This thesis consists of two parts. In the first part, the light-matter coupling between cyclotron transition and photon is theoretically investigated in some 2-D materials such as the monolayer MoS_2, graphene and monolayer black phosphorene (BP) systems. The results show that, in these 2-D materials, the ultrastrong light-matter coupling can be achieved at a high filling factor of Landau levels. Furthermore, we show that, in contrast to the case for conventional semiconductor resonators, the MoS_2 system shows a vacuum instability. In monolayer MoS_2 resonator, the

diamagnetic term can still play an important role in determining magnetopolariton dispersion which is different from monolayer graphene system. The diamagnetic term arises from electron-hole asymmetry which indicates that electron-hole asymmetry can influence the quantum phase transition. Meanwhile, we show that, similar with some other 2D materials such as graphene and MoS_2, the monolayer BP system shows a vacuum instability. However, in contrast with other 2D materials, the BP system displays a large energy gap between three branches of polaritons because of its strong anisotropic behavior in the eigenstates of the band structures. For the graphene system, we investigate the coupling of cyclotron transition and a multimode cavity described by a multimode Dicke model. This model exhibits a superradiant quantum phase transition, which we describe exactly in an effective Hamiltonian approach. The complete excitation spectrum in both the normal phase and superradiant phase regimes is given. At last, in contrast to the single mode case, multimode coupling of cavity photon and cyclotron transition can greatly reduce the critical vacuum Rabi frequency required for quantum phase transition, and dramatically enhance the superradiant emission by fast modulating the Hamiltonian. Our study provides new insights in cavity-controlled magneto-transport in these 2-D systems, which could lead to the development of polariton-based devices.

The second part is a diversion from the main content of this thesis; readers who are not interested in foundational issues of physics can skip this part. For one charged quantum particle P moving in an electromagnetic vector potential $\hat{A}_\mu = (\hat{\phi}, -\hat{\mathbf{A}})$ created by some other charged particles, we can either use the framework of one particle quantum mechanics (OPQM) to calculate the evolutions of P, or we can treat this as an multi-particles problem in the framework of quantum field theory and calculate the evolution of P. These two methods need to be equavalent, i.e., they produce the same result for the evolution of P. One open question is how to describe the evolution of P within the framework of quantum field theory and show that these two methods yield the same result? In chapter 5, we are going to derive the OPQM from the quantum field theory, i.e., the quantum electrodynamics (QED) to be specific. We start with the discussions on the AB effect then raise a plausible interpretation within the QED framework. We provide a quantum treatment of the source of the electromagnetic potential and argue that the underlying mechanism in

AB effect can be viewed as interactions between electrons described by QED theory where the interactions are mediated by virtual photons. On further analysis, we show that the framework of one particle quantum mechanics (OPQM) can be given, in general, as a mathematically approximated model which is reformulated from QED theory while the AB effect scheme provides a platform for our derivations. In addition, the classical Maxwell equations are derived from QED scattering process while both classical electromagnetic fields and potentials serve as mathematical tools that are constructed to approximate the interactions among elementary particles described by QED physics. This work opens up a new perspective on the nature of electromagnetic fields and potentials.

Thesis Supervisors: Wang Qijie (Nanyang Associate Professor) and
Daniel W. Hewak (Professor in Southampton University)

LIST OF FIGURES

Figure 1-1. Sketch of a cavity resonator embedding a bilayer graphene. A uniform and static magnetic field B is applied perpendicular to the graphene layer.. 16
Figure 1-2. Normalized frequencies of branches of magnetopolaritons as a function of doping density ρ ... .18
Figure 2-1. Sketch of a cavity resonator embedding a monolayer MoS2 with an uniform and static magnetic field B applied perpendicular to the material.. 26
Figure 2-2. The MoS2 cyclotron transition between conduction band LLs $n = v$ and $n = v - 1$ is quasi-resonant to a confined cavity photon mode.. 26
Figure 2-3. The dimensionless vacuum Rabi frequency Ω_2 / ω_{eg} versus the doping density ρ 40
Figure 2-4. Normalized frequencies of LP and UP branches of magnetopolariton as a function of doping density for $\eta = 1$ and $\eta = 2$ 40
Figure 2-5. Normalized frequencies of LP and UP branches of magnetopolariton as a function of doping density with and without the diamagnetic term for the second mode $\eta = 2$. 41
Figure 2-6. (a) Normalized frequencies of LP and UP branches of magnetopolariton as a function of magnetic field B, doping density is $\rho = 2.81 \times 10^{12} cm^{-2}$ (b) Normalized frequencies of LP and UP branches of magnetopolariton as a function of magnetic field B, doping density is $\rho = 1.42 \times 10^{13} cm^{-2}$ 42
Figure 3-1. Sketch of a cavity resonator embedding a monolayer BP material with a uniform and static magnetic field B applied perpendicular to the material. 48
Figure 3-2. The dimensionless vacuum Rabi frequency Ω_1 / ω_e versus the doping density ρ 51
Figure 3-3. (a) Normalized frequencies of the lower branch of magnetopolariton as a function of doping density (b) Normalized frequencies of one upper and one middle branches of magnetopolariton as a function of doping density 51
Figure 3-4. (a) Normalized frequencies of the lower branch of magnetopolariton as a function of magnetic field B (b) Normalized frequencies of one upper and one middle branches of magnetopolariton as a function of magnetic field B 52
Figure 4-1. Sketch of a one dimensional cavity embedding graphene sheet, a uniform and static magnetic field B is applied along the z axis 55
Figure 4-2. (a) Normalized frequencies of magnetopolariton both in normal and superradiant phases as a function of doping density ρ with $B = 8mT$. (b) Normalized frequencies of magnetopolariton both in normal and superradiant phases as a function of magnetic field B. (c) The scaled ground state energy both in normal and superradiant phases as a function of doping density ρ. (d) The scaled ground state energy both in

normal and superradiant phases as a function of magnetic field B with doping density ρ=2.40×10^{9}cm^{-2} 59
Figure 4-3. Normalized frequencies of magnetopolariton for multimode versus single-mode as a function of doping density ρ 60
Figure 4-4. (a) The scaled mean photon number as a function of doping density ρ. (b) electronic inversion as a function of doping density ρ. (c) The scaled mean photon number and the electronic inversion as a function of the magnetic field B with doping density ρ=2.40×10^{9}cm^{-2} 61
Figure 4-5. Normalized frequencies of magnetopolariton both in normal and superradiant phases as a function of cavity dimension L_z with $B=8mT$ and the doping density is ρ_c=1.06×10^{9}cm^{-2} 62
Figure 5-1. Sketch of a double-slit experiment in which the Aharonov-Bohm effect can be observed.. 67

1. INTRODUCTION

Cavity QED is to study the light-matter interaction in a reflective cavity where the quantum nature of light photons in the cavity is significant. Excitons are defined as the bond states between electrons and holes which are attacted to each other by the Coulomb force, they can be treated as quasiparticles that exist in solids and liquids. The strong interaction between an exciton and cavity photon in a high-finesse microcavity can induce a hybrid light-matter eigenstate which is usually named as polariton in solid-state systems [1]. This strong light-matter interaction can be achieved when this interaction is larger than all broadenings caused by other various factors e.g. electron phonon scattering and cavity loss. The polariton is now stimulating tremendous research interests due to its high potential in cavity quantum electrodynamics (QED) [2] and the achievement of polaritonic devices [3]–[5]. Moreover, when the interaction strength between an excitation and the cavity photon, quantified by vacuum Rabi frequency, becomes comparable to or larger than the corresponding electronic transition frequency in a cavity, the system can enter an ultrastrong coupling regime, which has been experimentally observed [6]. In this regime, the standard rotating-wave approximation is no longer valid and the antiresonant term of the interaction Hamiltonian starts to play an important role, giving rise to exciting effects in cavity QED [7], [8]. For the light-matter radiation, if the atoms were radiating coherently, the atomic ensemble spontaneously emits with an intensity proportional to the square of the number of the atoms, this gives the concept of super-radiance [9].

In this chapter, the background of the superradiant phase transition of Dicke model of single-mode will be introduced in the beginning, followed by a review of the theoretical work on multi-mode Dicke model with the emphasis of its difference and significance compared with the single-mode case. Meanwhile, the ultrastrong light-matter coupling for 2D electron gas in semiconductor quantum wells is discussed, we also show the superradiant quantum phase transition in cavity-graphene system despite the absence of superradiant phase transition in normal semiconductors. At last, we briefly highlight some motivations behind our work.

1.1 Superradiant Phase Transiton of Single-Mode Dicke Model

In this paragraph, we give a brief review of the theoretical formulation of the superradiant phase transition of single-mode Dicke model based on Ref. [9]–[11]. Indeed, the Dicke model allows us to investigate the superradiant phase of the system, a macroscopically excited and highly collective state that possesses the potential to super-radiant [12]–[20].

The single-mode Dicke Hamiltonian (DH) describes a collection of N two-level atoms interacting with a single bosonic mode via a dipole interaction; it was further shown to admit a second-order quantum phase transition at certain coupling strength Ω_c in the $N \to \infty$ limit [8]. The single-mode DH in terms of collective operators reads as

$$\frac{H}{\hbar} = \omega_0 J_z + \omega a^\dagger a + \frac{\Omega}{\sqrt{N}}(a^\dagger + a)(J_+ + J_-) \tag{1-1}$$

where J_+, J_- and J_z are the anguler momentum operators, ω_0 is the energy gap between the two energy levels of an atom. ω is the frequency of the bosonic mode and Ω is the coupling strength between the atoms with the bosonic mode. In order to show that the single-mode DH undergo a quantum phase transition at a critical value at $\Omega_c = \sqrt{\omega\omega_0}/2$, we need to apply the Holstein-Primakoff [21] representation of the angular-momentum operators in the following way

$$J_+ = b^\dagger\sqrt{N - b^\dagger b}, J_- = \sqrt{N - b^\dagger b}b \tag{1-2}$$

And $J_z = b^\dagger b - N/2$ where Bosonic operators obey the commutation relation $[b, b^\dagger] = 1$. Substituting Eq. (1-2) into Eq. (1-1), we get the Dicke Hamiltonian written in bosonic operators as

$$\frac{H}{\hbar} = \omega_0 b^\dagger b + \omega a^\dagger a + \Omega(a^\dagger + a)(b^\dagger\sqrt{1 - \frac{b^\dagger b}{N}} + \sqrt{1 - \frac{b^\dagger b}{N}}b) \tag{1-3}$$

In normal phase where $\frac{b^\dagger b}{N} \approx 0$, we get the effective Hamiltonian as

$$\frac{H}{\hbar} = \omega_0 b^\dagger b + \omega a^\dagger a + \Omega(a^\dagger + a)(b^\dagger + b) \tag{1-4}$$

Upon diagonalization of the above Hamiltonian, we get the eigen-frequencies as

$$E_\pm = \sqrt{\frac{1}{2}\{\omega^2 + \omega_0^2 \pm \sqrt{(\omega_0^2 - \omega^2)^2 + 16\Omega^2\omega\omega_0}\}} \tag{1-5}$$

Now we can see that E_- is real only when $\Omega \le \sqrt{\omega\omega_0}/2 \equiv \Omega_c$, therefore, the Eq. (1-5) remains valid under condition $\Omega \le \Omega_c$, i.e., in normal phase.

For the system passing the critical point $\Omega > \Omega_c$, both the atomic ensemble and the optical field can acquire macroscopic occupations. In order to describe this scenario, i.e., the superradiant phase, we can define new Holstein-Primakoff representation of the angular-momentum operators as

$$\tilde{a}^\dagger = a^\dagger - \sqrt{\alpha}, \tilde{b}^\dagger = b^\dagger + \sqrt{\beta} \tag{1-6}$$

Now we can substitute Eq. (1-6) into Eq. (1-3), in order to eliminate the terms that are linear in the bosonic operators, we get the solutions

$$\alpha = \frac{N(\Omega^2 - \Omega_c^2)}{\omega^2}, \beta = \frac{N(\Omega^2 - \Omega_c^2)}{2\Omega^2} \tag{1-7}$$

Therefore, the new effective Hamiltonian can be given as

$$\begin{aligned}\frac{H}{\hbar} &= \omega\tilde{a}^\dagger\tilde{a} + \frac{\omega_0(\Omega_c^2 + \Omega^2)}{2\Omega_c^2}\tilde{b}^\dagger\tilde{b} + \frac{\omega_0(\Omega^2 - \Omega_c^2)(3\Omega^2 + \Omega_c^2)}{8\Omega_c^2(\Omega^2 + \Omega_c^2)}(\tilde{b}^\dagger + \tilde{b})^2 \\ &+\Omega_c^2\sqrt{\frac{2}{\Omega^2 + \Omega_c^2}}(\tilde{a}^\dagger + \tilde{a})(\tilde{b}^\dagger + \tilde{b})\end{aligned} \tag{1-8}$$

Upon diagonalization of this new Hamiltonian, we get the eigen-frequencies in superradiant phase as

$$E_\pm = \sqrt{\frac{1}{2}[\omega^2 + \frac{\omega_0^2\Omega^4}{\Omega_c^4} \pm \sqrt{(\frac{\omega_0^2\Omega^4}{\Omega_c^4} - \omega^2)^2 + 4\omega^2\omega_0^2}\,]} \tag{1-9}$$

From Eq. (1-9), we see that E_- is real provided that $\Omega > \Omega_c$, therefore, Eq. (1-9) indeed describes the system in the superradiant phase, Eq. (1-5) and Eq. (1-9) altogether indeed describe the complete spectrum of the single-mode Dicke model.

1.2 Superradiant Phase Transiton of Multi-Mode Dicke Model

In this section, we are going to briefly review a more general Dicke model in which the two-level atomic transition system is coupled to an arbitrary set of optical modes with arbitrary coupling constants. This is motived by the fact that it is rather a tough problem in many circumstances to create an environment with a single optical mode. Following the Ref. [22], similar as Eq. (1-3), the Hamiltonian of the multi-mode Dicke model can be given as

$$\frac{H}{\hbar} = \sum_i \omega_i a_i^\dagger a_i + \omega_0 b^\dagger b + \sum_i \frac{\Omega_i}{\sqrt{N}} (a_i^\dagger + a_i)(b^\dagger \sqrt{N - b^\dagger b} + \sqrt{N - b^\dagger b} b) \tag{1-10}$$

In which Ω_i represents the coupling strength between the atomic system with the optical i-th mode with $i = 1, 2, \ldots, \mathrm{M}$. In normal phase which is similar as Eq. (1-4), we get the Hamiltonian as

$$\frac{H}{\hbar} = \sum_i \omega_i a_i^\dagger a_i + \omega_0 b^\dagger b + \sum_i \Omega_i (a_i^\dagger + a_i)(b^\dagger + b) \tag{1-11}$$

This Hamiltonian is quadratic and can be brought into the diagonal form by the Bogolubov transformation [23] by introducing a new set of Bosonic operators as

$$c_k = \sum_j (A_{kj} a_j + \tilde{A}_{kj} a_j^\dagger) \tag{1-12}$$

with $a_{j=0} \equiv b$ and $a_{j=i} \equiv a_i$. Upon diagonalization of the Hamiltonian using new defined operators, we can get the eigen-energies E of Eq. (1-11) that satisfy the below equation

$$4\omega_0 \sum_{i=1}^{\mathrm{M}} \frac{\Omega_i^2 \omega_i}{\omega_i^2 - E^2} + E^2 - \omega_0^2 = 0 \tag{1-13}$$

From the above expression, we can see that the eigen-energy E is real only when $\sum_i \Omega_i^2 / \omega_i < \omega_0 / 4$, this critical value defines the quantum phase transition point,

separating normal and superradiant phases. Passing the critical point $\sum_i \Omega_i^2 / \omega_i \geq \omega_0 / 4$, the system enters the super-radiant phase, which we will show below.

To get the effective Hamiltonian passing the critical point we displace all the bosonic modes in Eq. (1-10) by $\tilde{a}_i = a_i \pm \sqrt{\alpha_i}$ and $\tilde{b} = b \mp \sqrt{\beta}$ where α and β are some complex constants and eliminate the terms in Eq. (1-10) that are linear in the Bosonic operators by choosing $\beta = \frac{N}{2}(1-\eta)$ and $\alpha_i = \frac{4\beta(N-\beta)\Omega_i^2}{N\omega_i^2}$ where $\eta \equiv \frac{\omega_0}{4\sum_i \Omega_i^2 / \omega_i}$. The effective Hamiltonian beyond the phase transition point becomes

$$\frac{H_{SR}}{\hbar} = \sum_i \omega_i \tilde{a}_i^\dagger \tilde{a}_i + \tilde{\omega}_0 \tilde{b}^\dagger \tilde{b} + \sum_i \tilde{\Omega}_i (\tilde{a}_i^\dagger + \tilde{a}_i)(\tilde{b}^\dagger + \tilde{b}) + f(\tilde{b}^2 + \tilde{b}^{\dagger 2}) + const \tag{1-14}$$

where $\tilde{\omega}_0 = \frac{\omega_0(-\eta^2 + 6\eta + 3)}{4\eta(\eta+1)}$, $\tilde{\Omega}_i = \Omega_i \eta \sqrt{\frac{2}{1+\eta}}$ and $f = \frac{\omega_0(-3\eta^2 + 2\eta + 1)}{8\eta(\eta+1)}$.

Then the excitation spectrum $\tilde{E}$ passing the critical point can be given by solving the below equation

$$4(\tilde{\omega}_0 - 2f)\sum_i \frac{\omega_i \tilde{\Omega}_i^2}{\omega_i^2 - \tilde{E}^2} = \tilde{\omega}_0^2 - 4f^2 - \tilde{E}^2 \tag{1-15}$$

Therefore, Eq. (1-13) and Eq. (1-15) altogether give the complete spectrum of the multi-mode Dicke model for both normal phase and superradiant phase, from the spectrum of multi-mode Dicke model, we will see that the superradiant phase transition can be achieved with smaller value of Rabi frequencies compared with the single-mode case, this point will be more clearly illustrated in chapter 4.

1.3 Polariton and Ultrstrong Light-Matter Coupling For 2D Electron Gas

In the previous paragraph, we briefly reviewed the superradiant phase transition of the Dicke model, both in single-mode and multi-mode cases. However, a more

realistic model should include the quadratic field term A^2 ($\boldsymbol{A}$ is the vector potential of the electromagnetic field) which was absent in Dicke Hamiltonian that were introduced in chapters 1.1, 1.2. Meanwhile, some researchers showed that there is a no-go theorem which states the quantum critical point, which separate the normal phase and superradiant phase, disappears in presence of the A^2 term as a consequence of the TRK sum rule for the oscillator strength [24]. In addition, some combined systems, such as cyclotron transition of two-dimensional electron gas coupled with a cavity resonator or semiconductor intersubband transition coupled with a microcavity photon mode, were shown to present large diamagnetic term (A^2 term) which again prevent quantum instability from happening [7], [25].

In the work published in year 2010 [21], researchers investigated the coupling of the magnetic cyclotron transition of the 2D electron gas to optical modes in a cavity resonator. They consider a system consisting of multiple doped semiconductor quantum wells (QWs) in presence of a magnetic field B that is perpendicular to the QW plane. The QWs are embedded in a wire-like cavity resonator in presence of a magnetic field, the electrons occupy highly degenerate Landau levels (LLs), separated by the cyclotron energy $\hbar\omega_0$ where $\omega_0 = \frac{eB}{m^* c}$ and m^* is the effective electron mass of the 2D electron gas. For the case of an integer filling factor v, the electrons fill completely the LLs from $n=0$ to $n=v-1$, therefore, only transitions between the level $n=v-1$ and $n=v$ need to be considered due to the Pauli blocking and harmonic oscillator selection rules. In this light-matter coupled system, the Hamiltonian consists of four parts, that is

$$H = H_L + H_{\text{int}} + H_{dia} + H_c \tag{1-16}$$

where $H_L = \sum_{q_x} \hbar\omega_0 b_{q_x}^{\dagger} b_{q_x}$ represents the Landau level Hamiltonian and $b_{q_x}^{\dagger}$ is the creation operators associated to the cyclotron transition between the Landau level $n=v-1$ and $n=v$, q_x is the wave vector of the cavity mode in x direction. The second term in Eq. (1-16) represents the light-matter coupling Hamiltonian which can be given as

$$H_{\text{int}} = \sum_{q_x} i\hbar\Omega_{q_x}[a_{q_x}(b^{\dagger}_{q_x} - b_{-q_x}) + a^{\dagger}_{q_x}(b^{\dagger}_{-q_x} - b_{q_x})] \tag{1-17}$$

where $a^{\dagger}_{q_x}$ represents creation operator of the optical modes with wave-vector q_x and Ω_{q_x} is the Rabi coupling frequency. The third term H_{dia} comes from the squared vector potential $\boldsymbol{A}^2_{em}$ of the optical modes in the cavity, it can be given as

$$H_{dia} = \sum_{q_x} \hbar D_{q_x}[a_{q_x}a_{-q_x} + a_{q_x}a^{\dagger}_{q_x} + a^{\dagger}_{q_x}a_{q_x} + a^{\dagger}_{q_x}a^{\dagger}_{-q_x}] \tag{1-18}$$

in which $D_{q_x} = \Omega^2_{q_x} / \omega_0$ is the diamagnetic coupling strength. The last term H_c is the Hamiltonian for the optical modes in the cavity can be given as

$$H_c = \sum_{q_x} \hbar\omega_{q_x} a^{\dagger}_{q_x} a_{q_x} \tag{1-19}$$

Since the overall Hamiltonian is quadratic in terms of a_{q_x} and b_{q_x} operators, therefore, it can be diagonalized by introducing the magneto-polariton operators $p^{(i)}_{q_x}$ defined as

$$p^{(i)}_{q_x} = W^{(i)}_{q_x} a_{q_x} + X^{(i)}_{q_x} b_{q_x} + Y^{(i)}_{q_x} a^{\dagger}_{q_x} + Z^{(i)}_{q_x} b^{\dagger}_{-q_x} \tag{1-20}$$

where the index i indicate the polariton branches. The magneto-polariton operators also satisfy the Bose commutation relation as $[p^{(i)}_{q_x}, p^{\dagger(j)}_{q'_x}] = \delta_{i,j}\delta_{q_x,q'_x}$. Therefore, by using Eq. (1-20), the Hamiltonian of Eq. (1-16) can be written in a form as

$$H = \sum_{i,q_x} \hbar\omega^{(i)}_{q_x} p^{\dagger(i)}_{q_x} p^{(i)}_{q_x} + const. \tag{1-21}$$

By calculating the commutation relation $[p^{(i)}_{q_x}, H] = \hbar\omega^{(i)}_{q_x} p^{(i)}_{q_x}$, we can get $\mathrm{M}_{q_x} v^{(i)}_{q_x} = \hbar\omega^{(i)}_{q_x} v^{(i)}_{q_x}$ in which $v^{(i)}_{q_x}$ is the vector $(W^{(i)}_{q_x}, X^{(i)}_{q_x}, Y^{(i)}_{q_x}, Z^{(i)}_{q_x})^{\mathrm{T}}$ and M_{q_x} is the matrix given as

$$\mathrm{M}_{q_x}=\begin{pmatrix} \omega_{q_x}+2D_{q_x} & i\Omega_{q_x} & -2D_{q_x} & i\Omega_{q_x} \\ -i\Omega_{q_x} & \omega_0 & i\Omega_{q_x} & 0 \\ 2D_{q_x} & i\Omega_{q_x} & -\omega_{q_x}-2D_{q_x} & -i\Omega_{q_x} \\ i\Omega_{q_x} & 0 & -i\Omega_{q_x} & -\omega_0 \end{pmatrix} \tag{1-22}$$

Upon diagonalization of this matrix, the eigenvalues as the magneto-polariton frequencies can be obtained. Note that the no-go theorem indicates that for a system with $D_{q_x} \geq \Omega_{q_x}^2 / \omega_0$ (note that D_{q_x} comes from the quadratic field term A^2), the eigenvalue of M_{q_x} never vanishes, therefore, in such cases, the superradiant quantum phase transitions for the vacuum have been prohibited.

1.4 Polariton and Superradiant Phase Transition of Graphene in a Cavity

The discovery of graphene has attracted a great deal of investigations into two dimensional (2D) materials due to a wide range of extraordinary electrical, optical, mechanical and thermal properties [26]. In the previous chapter, we discussed that in some doped semiconductor QWs the superradiant phase transition does not occur due to the no-go theorem. One intriguing question is whether it is possible to achieve the quantum phase transition in some 2D materials.

Recently, it has been predicted that graphene can enter the ultrastrong light-matter coupling regime under perpendicular magnetic field due to the negligible diamagnetic term D_{q_x} in Eq. (1-22) [27], [28]. In particular, a vacuum instability (phase transition) analogous to the one occurring in the Dicke model can also occur for graphene in this ultrastrong coupling regime, which is absent in the case of massive electrons in semiconductors. In this chapter, we are going to briefly review the graphene quantum phase transition following the Ref. [27].

In the work of Ref. [27], researchers theoretically investigate the magnetopolariton in bilayer graphene under a perpendicular magnetic field using the quantum field theory. When the trigonal warping is neglected, the low energy effective Hamiltonian in K valley can be given as

$$H=-\frac{1}{2m}\begin{pmatrix} 0 & (p^{\dagger})^2 \\ p^2 & 0 \end{pmatrix}-\frac{U}{2}\begin{pmatrix} 1 & 0 \\ 0 & -1 \end{pmatrix}+\frac{1}{2m}\frac{U}{\gamma_1}\begin{pmatrix} p^{\dagger}p & 0 \\ 0 & -pp^{\dagger} \end{pmatrix} \tag{1-23}$$

where $p = p_x + ip_y$. The effective mass is $m = \gamma_1 / 2v^2$ where γ_1 is the interlayer hopping amplitude and v is the single-layer Dirac velocity. The parameter U describes the asymmetry between the top and bottom layers. The cavity geometry that is considered has a dimension with a volume $V = L^2 L_z$, the graphene sheet is placed at the center of the cavity perpendicular to the z direction while the magnetic field is applied perpendicular to the graphene layer, as shown in Fig. 1-1 (more information can be seen in Appendix A). When the magnetic field is applied, the electrons occupy highly degenerate LLs, the Landau level spectrum can be solved by replacing the wave-vector $\boldsymbol{p}$ in Eq. (1-23) with $\boldsymbol{\Pi}_0 = \boldsymbol{p} + \frac{e}{c}\boldsymbol{A}_0$ where $A_0 = (-By, 0, 0)$ is the vector potential in Landau gauge. The cavity length L_z along the z direction is much smaller than the other two transverse size L.

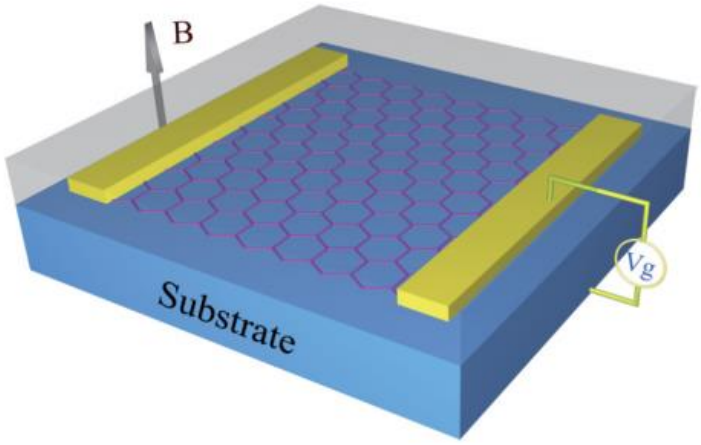

Fig. 1-1 Sketch of a cavity resonator embedding a bilayer graphene. A uniform and static magnetic field B is applied perpendicular to the graphene layer. (This figure is from Ref. [27])

With the considered cavity above, a cavity mode with the wave vector $\boldsymbol{q} = (q_x, q_y, q_z) = (\frac{2\pi}{L}, \frac{2\pi}{L}, \frac{2\pi}{L_z})$ is quasi-resonant with the active cyclotron transition. For this considered cavity mode, the electromagnetic vector potential can be given as

$$\boldsymbol{A}_{em}(r) = \sum_{\eta=1,2} \sqrt{\frac{2\pi\hbar c^2}{\varepsilon\omega_c V}} \mathbf{u}_{\boldsymbol{\eta}} (a_\eta + a_\eta^\dagger) \tag{1-24}$$

where a_η is the annihilation operator for a given photon mode $\eta = 1, 2$, ε is the cavity dielectric constant for bilayer graphene. The cavity frequency $\omega_c = [\pi c / (L_z \sqrt{\varepsilon})]\sqrt{1+8(L_z / L)^2}$ and the modes spatial profile $\mathbf{u}_\eta$ can be written as

$$u_1 = \begin{pmatrix} 2cos(2\pi x / L)sin(2\pi y / L)cos(\theta) \\ 2sin(2\pi x / L)cos(2\pi y / L)cos(\theta) \\ 0 \end{pmatrix} \tag{1-25}$$

$$u_2 = \begin{pmatrix} -2cos(2\pi x / L)sin(2\pi y / L) \\ 2sin(2\pi x / L)cos(2\pi y / L) \\ 0 \end{pmatrix} \tag{1-26}$$

where $cos(\theta) = 1/\sqrt{1+8(L_z / L)^2}$. The light-matter interaction can be described by the minimal coupling $\mathbf{\Pi}_0 \to \mathbf{\Pi}_0 + \frac{e}{c}\boldsymbol{A}_{em}$. Therefore, the bosonic mode annihilation operators between Landau level transitions $n \to n-1$ can be given as

$$\begin{aligned} d_1 &\equiv \sqrt{\frac{1}{n_B}} \sum_{k,\pm} \sin[\frac{2\pi l_B^2}{L}(k \pm \frac{\pi}{L}) \mp \frac{\pi}{4}] c^\dagger_{v-1,k} c_{v,k\pm\frac{2\pi}{L}} \\ d_2 &\equiv \sqrt{\frac{1}{n_B}} \sum_{k,\pm} \cos[\frac{2\pi l_B^2}{L}(k \pm \frac{\pi}{L}) \mp \frac{\pi}{4}] c^\dagger_{v-1,k} c_{v,k\pm\frac{2\pi}{L}} \end{aligned} \tag{1-27}$$

where $n_B = \frac{2L^2}{\pi l_B^2}$ is the Landau level degeneracy and $l_B = \sqrt{\frac{\hbar c}{eB}}$ is defined as the magnetic length. Starting from the bosonic mode operators, the bosonlized Hamiltonian for Eq. (1-23) can be given as three parts, which is

$$H = \sum_{\eta=1,2} \hbar[\omega_{eg} d_\eta^\dagger d_\eta + \Omega_\eta \chi_\eta (d_\eta + d_\eta^\dagger)(a_\eta^\dagger + a_\eta) + D_\eta (a_\eta + a_\eta^\dagger)^2 \ ] \tag{1-28}$$

in which the third term that comes from the $\boldsymbol{A}_{em}^2(r)$ in Eq. (1-24) is called the diamagnetic term. Indeed, for bilayer graphene in the cavity, we have $\frac{\Omega_2^2 / \omega_{eg}}{|D_2|} \gg 1$, therefore, the no-go theorem in Chapter 1.3 no longer applies in this case and we can neglect the third term in Eq. (1-28). While the Coulomb Hamiltonian can be given as

$$H_{Coul} = \sum_{\eta} V_c \chi_\eta (d_\eta + \chi_\eta d_\eta^\dagger)^2 \tag{1-29}$$

Adding Eq. (1-28) and Eq. (1-29) together, then we can diagonalize the total Hamiltonian by introducing the polariton operators as $p_j = X_j a_1 + Y_j a_2 + Z_j b + \tilde{X}_j a_1^\dagger + \tilde{Y}_j a_2^\dagger + \tilde{Z}_j b^\dagger$, therefore, the total Hamiltonian in polariton basis can be written as

$$H + H_{Coul} = \sum_{j=1,2} \hbar\omega_j p_j^\dagger p_j + const. \tag{1-30}$$

Here j indicates branches of polaritons and we have the commutation relation $[p_j, p_{j'}^\dagger] = \delta_{j,j'}$. By calculating the commutation relation $[p_j, H] = \hbar\omega_j p_j$, the polariton frequency ω_j can be obtained eventually given as Fig. 1-2

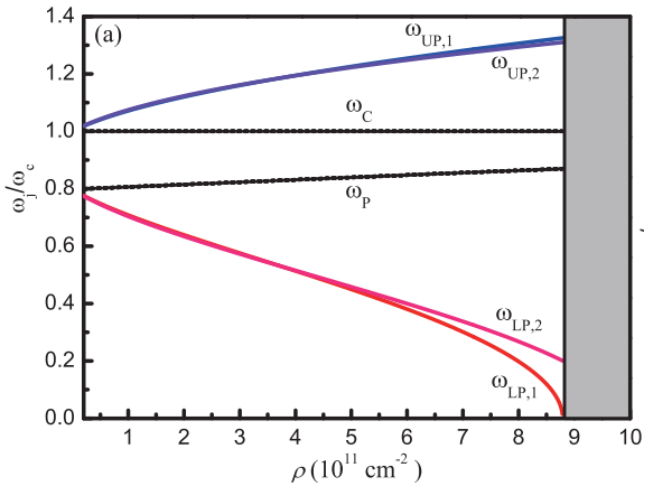

Fig. 1-2 Normalized frequencies of branches of magnetopolaritons as a function of doping density ρ . The critical density that separates the normal phase and superradiant phase is $\rho_c = 8.8\times10^{11} cm^{-2}$. (This figure is from Ref. [27])

Since the transition frequency ω_{eg} and the vacuum Rabi frequency Ω_η in Eq. (1-28) all depend on the doping density, the spectrums of different branches of magnetopolaritons in normal phase, which are shown as red and blue curves in Fig. 1-2, can be plotted as a function of doping density ρ . The critical point that separates

the normal phase and superradiant phase is $\rho_c = 8.8\times10^{11} cm^{-2}$ passing which the system will enter the superradiant phase.

1.5 Polarition, Superradiant phase transition and their applications

In this chapter, we are going to discuss some of the potential applications based on polaritons and superradiant phase transitions. As we discussed in previous chapters, if graphene or other semiconductor is enclosed within an optical cavity, the cyclotron transiton-photon interaction can give rise to some new sets of states, whose dispersion are given by polaritons. These resulting microcavity polaritons possess number of additional remarkable fascinating effects which have been observed in semiconductor polariton micro-cavities, such as superfluidity [29], [30], long-range spatial coherence [31]–[33] and many others [34]. Like traditional quantum optics, quantum polaritonics could have potential applications in cryptography, computation and simulation [35]. In previous chapters, we also showed that for increasing light-matter coupling strength, the Dicke model predicts a Superradiant phase transition, with a doubly degenerate ground state above a critical vacuum Rabi coupling. This so-called Superradiant phase is characterized by a spontaneous polarization of the atoms and a spontaneous coherence of the cavity optical field. The experimental realization of quantum phase transition from normal phase to superradiant phase is a mile-stone in this field [36], [37]. In a superradiant emission regime, the formation of a macroscopically ordered state shows that it is a different class of emission from conventional spontaneous or stimulated emission, which could lead to ultra-superluminal pulse propagations [38] and have potential applications in quantum information processing and quantum computings [39].

1.6 Summary and Motivation

In the above investigations of the magnetopolaritons in cavity, the effect of the electronic level broadening due to impurities is neglected. Normally the decay of Landau level excitation due to electron-impurity scattering can induce the electronic level broadening. If the decay rate is larger than the vacuum Rabi frequency, it will make the ultrastrong light-matter coupling not observable. For the sake of simplicity, in this thesis we have assumed zero temperature to ensure the cyclotron transition

energy larger than thermal energy and avoid the effect of impurity scattering in our calculation.

In chapter 1.1 and chapter 1.2, we briefly introduced the theoretical Dicke model in both single-mode and multi-mode cases, in particular the superradiant phase transition are discussed. In chapter 1.3, we point out that the superradiant phase transition does not occur in some doped semiconductor quantum wells due to the no-go theorem. In chapter 1.4, the calculations show that the superradiant phase transiton indeed occurs in graphene-cavity systems due to the negligiable diamagnetic term D_η and the spectrum of magnetopolaritons in normal phase is plotted. However, the spectrum in superrandiant phase is not investigated in graphene-cavity system; moreover, only the single-mode Dicke model is studied in graphene-cavity systems. Some open questions are whether some other 2D materials in the cavity will enter the superradiant phase by adjusting some parameters and can we obtain the spectrum of magnetopolartions in the superradiant phase regime based on the multi-mode Dicke model. Apart from the discussions in chapter 1.5, our theoretical study of polaritons and superradiant phase transition can also provide new insights in cavity-controlled magneto-transport in these 2D systems, which could lead to the development of some polariton-based devices [40].

1.7 Thesis Overview

This thesis consists of two parts. In the first part, which is from chapter 2 to chapter 4, the light-matter coupling between cyclotron transition and photon is theoretically investigated in some 2-D materials such as the monolayer MoS_2, monolayer BP systems and graphene. In chapter 2, we show that, in contrast to the case for conventional semiconductor resonators, the MoS_2 system show a vacuum instability. In monolayer MoS_2 resonator, the diamagnetic term can still play an important role in determining magnetopolariton dispersion which is different from monolayer graphene system. In chapter 3, we show that, similar with some other 2D materials such as graphene and MoS_2, the monolayer BP system shows a vacuum instability. However, in contrast with other 2D materials, the BP system displays a large energy gap between three branches of polaritons because of its strong anisotropic behavior in the eigenstates of the band structures. In chapter 4, we investigate the coupling of

cyclotron transition of LLs in monolayer graphene system with a multimode cavity described by a multimode Dicke model. This model exhibits a superradiant quantum phase transition, which we describe exactly in an effective Hamiltonian approach. The complete excitation spectrum in both the normal phase and superradiant phase regimes is given.

The second part is a diversion from the main part of this thesis, in chapter 5, we are going to investigate theoretically the Aharonov-Bohm (AB) effect from the quantum field theory approach, i.e., the quantum electrodynamics (QED) to be specific. We start with the discussions on the AB effect then raise a plausible interpretation within the QED framework. We provide a quantum treatment of the source of the electromagnetic potential and argue that the underlying mechanism in AB effect can be viewed as interactions between electrons described by QED theory where the interactions are mediated by virtual photons. On further analysis, we show that the framework of one particle quantum mechanics (OPQM) can be given, in general, as a mathematically approximated model which is reformulated from QED theory while the AB effect scheme provides a platform for our derivations. At last, the derivation of multi-particle classical fields and some discussions on the physical nature of fields and potentials are shown in Appendix C and Appendix D repectively.

2. POLARITON AND SUPERRADIANT PHASE TRANSITION IN MONOLAYER MOS2

In previous chapters, it has been shown that graphene can enter the ultrastrong light-matter coupling regime under perpendicular magnetic field. In particular, a vacuum instability (phase transition) analogous to the one occurring in the Dicke model can also occur for graphene in this ultrastrong coupling regime, which is absent in the case of massive electrons in semiconductors. In addition to graphene, monolayer group VI transition-metal dichalcogenides (e.g., $MoSe_2$ and WS_2) has emerged as a new class of 2D materials, which are being widely investigated. Due to their unique properties, MoS_2 and other TMDs have attracted great interest in the study of light-matter interactions. One important open question is whether MoS_2 and other TMDs systems can enter the ultrastrong coupling regime and whether a quantum phase transition (or vacuum instability) can occur. In this section, we theoretically study the magnetopolariton spectrum of the monolayer MoS2-cavity system, followed by an analysis of the difference with the magnetopolariton spectrum in the graphene-cavity system. Such novel difference can provides new insights in cavity-controlled magneto-transport in the MoS2 materials. The set up of the cavity-MoS2 system in this chapter follows the chapter 1-4. From the chapter 2 to chapter 4, for simplicity, we use the SI unit for theoretical derivations.

2.1 Theoretical Formulations

In addition to graphene, monolayer group VI transition-metal dichalcogenides (e.g. MoS_2, $MoSe_2$ and WS_2) has emerged as a new class of 2D materials, which are being widely investigated due to strong photoluminescence, excellent optical-electric properties and controllable valley polarization [41]–[55]. They have a direct bandgap in the visible range which is located at the K and K' points situated at the corners of the hexagonal first Brillouin zone with $K = (\frac{4\pi}{3\sqrt{3}a_0}, 0)$ and $a_0 = 1.84\,\text{Å}$. Optical selection rule in bulk crystals determines the optical transition between energy states. Valley angular momentum is associated with energy valleys in momentum space in monolayer MoS2. Bloch electrons have opposite signs of valley angular momentums in adjacent valleys and render a valley dependent optical selection rule. The inversion

symmetry is explicitly broken in monolayer MoS_2 and other transition-metal dichalcogenides (TMDs), giving rise to a valley-contrasting optical selection rule which allows optical pumping of valley-polarized carriers by circularly polarized light [56]. Due to their unique properties, MoS_2 and other TMDs have attracted great interest in the study of light-matter interactions. The strong light-matter coupling between an exciton and photon has been experimentally observed recently [57].

For the monolayer MoS_2 system, without an external field applied, the conduction and valence band edges are located at the two corners (i,e. K and K') of the first Brillion Zone. The first-principle calculation has shown that the main contributions to band edges near K and K' can be attributed to d_{z^2}, d_{xy} and $d_{x^2-y^2}$ orbitals of metal atoms and the low-energy band model has been constructed by using the $k \cdot p$ model [58]–[62]. Ignoring the trigonal warping effect, which can only provide small perturbation terms [63], [64], we can write two band Hamiltonian as [44], [64]

$$H_{\tau s} = t_0 a_0 \boldsymbol{k} \cdot \boldsymbol{\sigma_\tau} + \frac{\Delta}{2}\sigma_z + \lambda \tau s \frac{1-\sigma_z}{2} + \frac{\hbar^2 |\boldsymbol{k}|^2}{4m_0}(\alpha + \beta\sigma_z) \tag{2-1}$$

where the final term indicates the electron-hole asymmetry. m_0 is the free electron mass, $s = \pm$ indicates spin up and down respectively, $\tau = \pm$ indicates K and K' valley respectively, with Pauli matrices $\boldsymbol{\sigma}_\tau = \left(\tau\sigma_x, \sigma_y\right)$ and Bloch wavevector $\boldsymbol{k} = (k_x, k_y)$. The energy gap $\Delta = 1.9eV$ and the spin orbit coupling coefficient $\lambda = 80meV$. The other parameters are $t_0 = 1.68eV$, $\alpha = 0.43$, $\beta = 2.21$ and $a_0 = 1.84\,\text{Å}$ [64].

When a perpendicular magnetic field $\boldsymbol{B} = \nabla \times \boldsymbol{A}_0$ is applied to the MoS_2 plane, the electrons occupy highly degenerate LLs. Within the limit $a_0 / l_B \ll 1$, we can make the Landau-Peierls substitution $\boldsymbol{k} \to \boldsymbol{k} + e\boldsymbol{A}_0/\hbar$ to the Hamiltonian $H_{\tau s}$, where $l_B = \sqrt{\hbar/(eB)}$ is the magnetic length. Using the Landau gauge $\boldsymbol{A}_0 = \left(0, Bx, 0\right)$ and writing the wavefunction in K valley as

$$\phi_{n,k} = \left(a_n \,|\, n-1, k\rangle, b_n \,|\, n, k\rangle\right), n > 0 \tag{2-2}$$

$$\phi_{n=0,k} = \left(0, |0,k\rangle\right), n = 0 \tag{2-3}$$

with

$$a_n = \left(i\frac{\sqrt{2}}{l_B} a_0 t_0 \sqrt{n}\right) / N_o \tag{2-4}$$

$$b_n = [\frac{\Delta}{2} + \frac{\hbar^2}{2m_0 l_B^2}(n - \frac{1}{2})(\alpha + \beta) - E_{n,\tau=+}] / N_o \tag{2-5}$$

where $a_n a_n^* + b_n b_n^* = 1$ and N_o is the normalization factor. Note that $|n,k\rangle$ are LL states with quantum numbers n and k. In this work we assume the Fermi level is within the conduction band, and the eigen-energies are as follows [48]:

$$E_{n,\tau s} = \sqrt{\left[\frac{\Delta - \lambda\tau s}{2} + \hbar\omega_{cl}(\beta n - \frac{\alpha\tau}{2})\right]^2 + 2n(\frac{t_0 a_0}{l_B})^2} + \frac{\lambda\tau s}{2} + \hbar\omega_{cl}(\alpha n - \frac{\beta\tau}{2}) \tag{2-6}$$

where cyclotron frequency $\omega_{cl} = eB/2m_0$. In this work, we neglect the valley and spin splitting of LL energies which are small so as to have negligible effect on our results. Therefore, the LL degeneracy is $n_B = 4eBL^2/h$ where L is the cavity length. The first unoccupied LL index n is determined by the filling factor $\nu = \rho S / n_B$ (ρ is electron doping density) where $S = L^2$ being the monolayer MoS_2 surface area. For the sake of simplicity, we will consider the case of an integer filling factor ν. As we deal with the coupling between the light and high filling factor of LLs, we have to take into account the system at cryogenic temperature. Therefore, we assume cryogenic temperature in the rest of the calculations from chapter 2 to chapter 4 to ensure the cyclotron transition energy is larger than thermal energy. The loss of the 2D materials will not influence the excitation of spectrum of polariton. But large loss will prevent from observing the spectrum of polariton. The considered cryogenic temperature can ensure the loss smaller than Rabi frequency in our considered parameters.

We consider a rectangular cavity as depicted in Fig. 2-1 with perfectly conducting walls on all three sides and has the volume $V = L_z L^2$ with the monolayer MoS_2 material placed at the center of the cavity perpendicular to the z direction. The cavity

length L_z along the z direction is assumed to be much smaller than the cavity transverse size L. Therefore, we can restrict our study to the particular photon mode with $n_z = 1$, neglecting all the higher-lying modes $n_z > 1$, more information of this cavity can be found in case 3 of Appendix B. The electromagnetic vector potential can be written as

$$\boldsymbol{A}_{em}(r) = \sum_{\eta=1,2} \sqrt{\frac{\hbar}{2\varepsilon_0 \varepsilon \omega_c V}} \mathbf{u}_{\boldsymbol{\eta}} (a_\eta + a_\eta^\dagger) \tag{2-7}$$

where a_η is the annihilation operator for a given photon mode $\eta = 1, 2$, ε is the cavity dielectric constant and $\varepsilon = 4.2$ for monolayer MoS_2 [43]. Applying the cavity mode with wave vector $\boldsymbol{q} = (q_x, q_y, q_z) = (2\pi / L, 2\pi / L, \pi / L_z)$, the cavity frequency $\omega_c = [\pi c / (L_z \sqrt{\varepsilon})] \sqrt{1 + 8(L_z / L)^2}$ and the modes can be written as

$$u_1 = \begin{pmatrix} 2cos(2\pi x / L) sin(2\pi y / L) cos(\theta) \\ 2sin(2\pi x / L) cos(2\pi y / L) cos(\theta) \\ 0 \end{pmatrix} \tag{2-8}$$

$$u_2 = \begin{pmatrix} -2cos(2\pi x / L) sin(2\pi y / L) \\ 2sin(2\pi x / L) cos(2\pi y / L) \\ 0 \end{pmatrix} \tag{2-9}$$

where $cos(\theta) = 1 / \sqrt{1 + 8(L_z / L)^2}$.

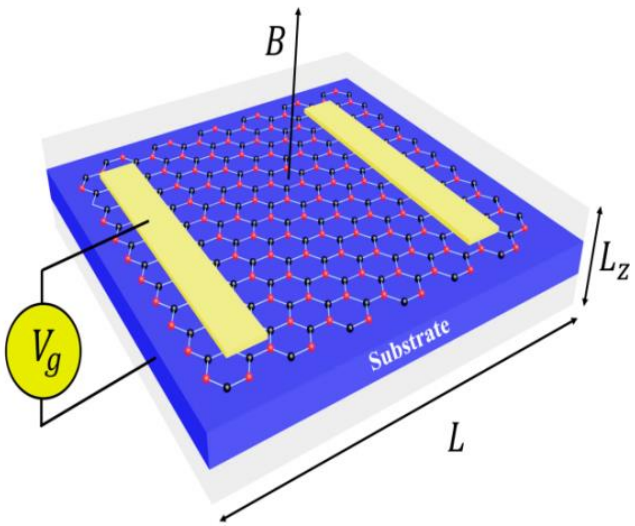

Fig. 2-1 Sketch of a cavity resonator embedding a monolayer MoS_2 with a uniform and static magnetic field B applied perpendicular to the material. Cavity walls in all three directions are perfectly conducting.

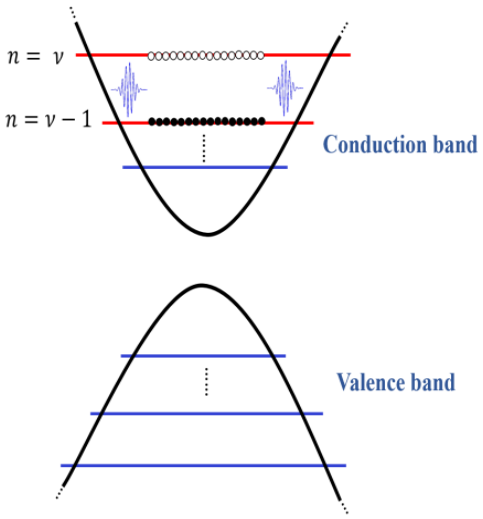

Fig. 2-2 The MoS_2 cyclotron transition between conduction band LLs $n = \nu$ and $n = \nu - 1$ is quasi-resonant to a confined cavity photon mode.

Now we can expand the total Hamiltonian of the MoS2-cavity system with respect to the wave-vector k up to second order as

$$H_{total} = H_1 + H_2 + H_{coul} \tag{2-10}$$

in which H_1 stands for the first order expansion of the Hamiltonian and likewise H_2 is the second order, plus, we also need to add H_{coul} which is the Coulomb potential into the total Hamiltonian of the system. In following paragraphs below we are going to analyze different meanings that they stand for and show detailed calculation techniques that we apply to obtain the second quantization form the total Hamiltonian. For the interaction part of the total Hamiltonian, neglecting the spin and valley splitting effects, the first order Hamiltonian including the light-matter interaction can be written as two parts $H_1 = H_{1,L} + H_{1,\text{int}}$, where the kinetic energy part reads

$$H_{1,L} = \begin{pmatrix} \frac{\Delta}{2} & 0 \\ 0 & -\frac{\Delta}{2} \end{pmatrix} + a_0 t_0 \begin{pmatrix} 0 & k_x + \frac{eA_{0,x}}{\hbar} - i(k_y + \frac{eA_{0,y}}{\hbar}) \\ k_x + \frac{eA_{0,x}}{\hbar} + i(k_y + \frac{eA_{0,y}}{\hbar}) & 0 \end{pmatrix} \tag{2-11}$$

And the light-matter interaction part reads

$$H_{1,\text{int}} = a_0 t_0 \begin{pmatrix} 0 & \frac{eA_{em,x}}{\hbar} - i\frac{eA_{em,y}}{\hbar} \\ \frac{eA_{em,x}}{\hbar} + i\frac{eA_{em,y}}{\hbar} & 0 \end{pmatrix} \tag{2-12}$$

Similarly, the second order Hamiltonian (electron-hole asymmetry term) including the light-matter interaction can be written as three parts $H_2 = H_{2,L} + H_{2,\text{int}} + H_{dia}$, where the kinetic energy part reads

$$H_{2,L} = \begin{pmatrix} (\alpha+\beta)\frac{\hbar^2}{4m_0}(\boldsymbol{k} + \frac{e\boldsymbol{A}_0}{\hbar})^2 & 0 \\ 0 & (\alpha-\beta)\frac{\hbar^2}{4m_0}(\boldsymbol{k} + \frac{e\boldsymbol{A}_0}{\hbar})^2 \end{pmatrix} \tag{2-13}$$

The light-matter interaction part reads

$$H_{2,\text{int}} = \begin{pmatrix} (\alpha+\beta)\frac{\hbar^2}{4m_0}[(\boldsymbol{k} + \frac{e\boldsymbol{A}_0}{\hbar})\cdot\frac{e\boldsymbol{A}_{em}}{\hbar} + \frac{e\boldsymbol{A}_{em}}{\hbar}\cdot(\boldsymbol{k} + \frac{e\boldsymbol{A}_0}{\hbar})] & 0 \\ 0 & (\alpha-\beta)\frac{\hbar^2}{4m_0}[(\boldsymbol{k} + \frac{e\boldsymbol{A}_0}{\hbar})\cdot\frac{e\boldsymbol{A}_{em}}{\hbar} + \frac{e\boldsymbol{A}_{em}}{\hbar}\cdot(\boldsymbol{k} + \frac{e\boldsymbol{A}_0}{\hbar})] \end{pmatrix}$$

(2-14)

And in addition we have the diamagnetic term which reads

$$H_{dia}=\begin{pmatrix}(\alpha+\beta)\dfrac{\hbar^2}{4m_0}(\dfrac{e\boldsymbol{A}_{em}}{\hbar})^2 & 0\\ 0 & (\alpha-\beta)\dfrac{\hbar^2}{4m_0}(\dfrac{e\boldsymbol{A}_{em}}{\hbar})^2\end{pmatrix} \tag{2-15}$$

where $\boldsymbol{A}_0=(0,Bx,0)$ and $\boldsymbol{A}_{em}$ is given by Eq. (2-7). In addition to the light-matter interaction, we should also include Coulomb interaction which plays an important role. Bearing these in mind, we can first deal with the Coulomb potential.

For the Coulomb potential H_{coul}, we need to consider the Coulomb interaction between transition $n=\nu-1$ and $n=\nu$ of LLs. Based on our cavity structure, we can write the Coulomb potential $V_c(\boldsymbol{r}-\boldsymbol{r}')=\dfrac{e^2}{4\pi\varepsilon_0\varepsilon|\boldsymbol{r}-\boldsymbol{r}'|}$ expanded in terms of 2D Fourier series as

$$V_c(\boldsymbol{r}-\boldsymbol{r}')=\sum_{n_x,n_y}\tilde{v}_{n_x,n_y}\cos[\frac{n_x\pi(x-x')}{L}]\cos[\frac{n_y\pi(y-y')}{L}] \tag{2-16}$$

where n_x and n_y runs over all positive integers. By the inverse Fourier transformation, we find

$$\begin{aligned}\tilde{v}_{n_x,n_y}&=\frac{C_{n_x,n_y}}{L^2}\int_0^L\int_0^L d\boldsymbol{r}V_c(\boldsymbol{r})\cos(\frac{n_x\pi x}{L})\cos(\frac{n_y\pi y}{L})\\&=\frac{C_{n_x,n_y}e^2}{8\pi\varepsilon_0\varepsilon L\sqrt{n_x^2+n_y^2}}\end{aligned} \tag{2-17}$$

Since we are only interested in the mode which is quasi-resonant to the transition energy of LLs, that is, $n_x=n_y=2$ with $C_{2,2}=4$. Therefore, we can neglect other Fourier modes which do not make any contributions to the LL transitions. We can write the mathematical expression $\cos[\dfrac{n_y\pi(x-x')}{L}]\cos[\dfrac{n_y\pi(y-y')}{L}]$ in Eq. (2-16) as

$$\cos[\frac{n_x\pi(x-x')}{L}]\cos[\frac{n_y\pi(y-y')}{L}]$$
$$=(\cos\frac{n_x\pi x}{L}\cos\frac{n_x\pi x'}{L}+\sin\frac{n_x\pi x}{L}\sin\frac{n_x\pi x'}{L})(\cos\frac{n_y\pi y}{L}\cos\frac{n_y\pi y'}{L}+\sin\frac{n_y\pi y}{L}\sin\frac{n_y\pi y'}{L})$$

(2-18)

This expression contains four major parts and they are symmetric in terms of $\boldsymbol{r}$ and $\boldsymbol{r}'$. Therefore, in order to obtain the second quantization form of the Coulomb potential, our aim is to express the cosine and sine functions in terms of bosonic operators. For example, we can write two cosine functions in LL basis as

$$\cos\frac{n_x\pi x}{L}\cos\frac{n_y\pi y}{L}=\sum_{n,k}\sum_{n',k'}(\phi^{\dagger}_{n,k}\cos\frac{n_x\pi x}{L}\cos\frac{n_y\pi y}{L}\phi_{n',k'})c^{\dagger}_{n,k}c_{n',k'}\equiv\Lambda_{cc} \qquad (2\text{-}19)$$

in which $\phi_{n,k}$ in K valley is just Eq. (2-2) and $c^{\dagger}_{n,k}$ is the creation operator for LL states $\phi_{n,k}$. Likewise, the cosine functions in prime coordinate systems can be given as

$$\cos\frac{n_x\pi x'}{L}\cos\frac{n_y\pi y'}{L}=\sum_{n,k}\sum_{n',k'}(\phi^{\dagger}_{n,k}\cos\frac{n_x\pi x'}{L}\cos\frac{n_y\pi y'}{L}\phi_{n',k'})c^{\dagger}_{n,k}c_{n',k'} \qquad (2\text{-}20)$$

Note that x (y) and x' (y') represents coordinate operators of two electrons here, thus, Eq. (2-19) is indeed equivalent to Eq. (2-20). Meanwhile, we can denote three other expressions in Eq. (2-18) as

$$\begin{aligned}
\cos\frac{n_x\pi x}{L}\sin\frac{n_y\pi y}{L}&=\sum_{n,k}\sum_{n',k'}(\phi^{\dagger}_{n,k}\cos\frac{n_x\pi x}{L}\sin\frac{n_y\pi y}{L}\phi_{n',k'})c^{\dagger}_{n,k}c_{n',k'}\equiv\Lambda_{cs}\\
\sin\frac{n_x\pi x}{L}\cos\frac{n_y\pi y}{L}&=\sum_{n,k}\sum_{n',k'}(\phi^{\dagger}_{n,k}\sin\frac{n_x\pi x}{L}\cos\frac{n_y\pi y}{L}\phi_{n',k'})c^{\dagger}_{n,k}c_{n',k'}\equiv\Lambda_{sc} \qquad (2\text{-}21)\\
\sin\frac{n_x\pi x}{L}\sin\frac{n_y\pi y}{L}&=\sum_{n,k}\sum_{n',k'}(\phi^{\dagger}_{n,k}\sin\frac{n_x\pi x}{L}\sin\frac{n_y\pi y}{L}\phi_{n',k'})c^{\dagger}_{n,k}c_{n',k'}\equiv\Lambda_{ss}
\end{aligned}$$

Put everything together, after divided by 2 due to the double counting of Coulomb potential between two electrons, we get the total Coulomb potential as

$$H_{coul} = \frac{1}{2}\tilde{v}_{n_x,n_y}(\Lambda_{cc}^2 + \Lambda_{cs}^2 + \Lambda_{sc}^2 + \Lambda_{ss}^2) \tag{2-22}$$

Thus, in order to obtain the second quantization form of the Eq. (2-22), we can write

$$\cos\frac{n_x\pi x}{L}\cos\frac{n_y\pi y}{L} = \frac{1}{4}[e^{i\frac{2\pi}{L}(x+y)} + e^{i\frac{2\pi}{L}(x-y)} + e^{-i\frac{2\pi}{L}(x-y)} + e^{-i\frac{2\pi}{L}(x+y)}] \tag{2-23}$$

Then plugging Eq. (2-23) into Eq. (2-20) we can first deal with the expression

$$\begin{aligned} &\phi_{n,k}^{\dagger} e^{i\frac{2\pi}{L}(x+y)} \phi_{n',k'} \\ &= a_n^* a_{n'} \langle n-1,k | e^{i\frac{2\pi}{L}(x+y)} | n'-1,k' \rangle + b_n^* b_{n'} \langle n,k | e^{i\frac{2\pi}{L}(x+y)} | n',k' \rangle \end{aligned} \tag{2-24}$$

Note that a_n and b_n in Eq. (2-24) are just coefficients in Eq. (2-2). Since we are dealing with low energy cavity modes, the LL mixing can be neglected and we have $\langle n,k|\exp(-i\boldsymbol{q}\cdot\boldsymbol{r})|n',k'\rangle = \exp\left(-i\frac{q_x(k+k')l_B^2}{2}\right)\chi_{n,n'}(ql_B)\delta_{k,k'+q_y}$ thanks to this condition $|\boldsymbol{q}|l_B \ll 1$, where $\chi_{n,n'}(ql_B) \equiv \Theta(n-n')G_{n,n'}(q^{\dagger}l_B) + \Theta(n'-n)G_{n',n}(ql_B)$, $G_{n,n'}(ql_B) = \sqrt{\frac{n'!}{n!}}(\frac{-iql_B}{\sqrt{2}})^{n-n'}\sum_{j=0}^{n'}\frac{n!}{(n'-j)!(n-n'+j)!}\frac{(-|ql_B|^2)^j}{2^j\, j!}$, $q = q_x + iq_y$, $q^{\dagger} = q_x - iq_y$ and $\Theta(n)$ is Heaviside step function [65]. Bearing in mind that we are dealing with the cyclotron transitions between the last occupied LL $\nu-1$ with the first unoccupied one ν. First, in case that $n = \nu-1$ and $n' = \nu$, we have

$$\begin{aligned} \langle n-1,k | e^{i\frac{2\pi}{L}(x+y)} | n'-1,k' \rangle &= \langle \nu-2,k | e^{i\frac{2\pi}{L}(x+y)} | \nu-1,k' \rangle \\ &= e^{i\frac{\pi(k+k')l_B^2}{L}} \chi_{\nu-2,\nu-1}(ql_B)\delta_{k,k'-2\pi/L} \\ &= e^{i\frac{\pi(k+k')l_B^2}{L}} \sqrt{\nu-1}(\frac{-iql_B}{\sqrt{2}})\delta_{k,k'-2\pi/L} \end{aligned} \tag{2-25}$$

Note that in the last step of Eq. (2-25), we neglected high orders of ql_B due to the fact that $|\boldsymbol{q}|l_B \ll 1$. Similarly, we can calculate the second term in Eq. (2-24) as

$$\begin{aligned}\langle n,k|e^{i\frac{2\pi}{L}(x+y)}|n',k'\rangle &= \langle v-1,k|e^{i\frac{2\pi}{L}(x+y)}|v,k'\rangle \\ &= e^{i\frac{\pi(k+k')l_B^2}{L}}\chi_{v-1,v}(ql_B)\delta_{k,k'-2\pi/L} \\ &= e^{i\frac{\pi(k+k')l_B^2}{L}}\sqrt{v}(\frac{-iql_B}{\sqrt{2}})\delta_{k,k'-2\pi/L}\end{aligned} \tag{2-26}$$

Therefore, in case that $n=v-1$ and $n'=v$, after some calculations we have

$$\begin{aligned}&\phi_{n,k}^{\dagger}\cos\frac{n_x\pi x}{L}\cos\frac{n_y\pi y}{L}\phi_{n',k'} \\ &= a_{v-1}^{*}a_v\langle v-2,k|\cos\frac{n_x\pi x}{L}\cos\frac{n_y\pi y}{L}|v-1,k'\rangle + b_{v-1}^{*}b_v\langle v-1,k|\cos\frac{n_x\pi x}{L}\cos\frac{n_y\pi y}{L}|v,k'\rangle \\ &= -\Upsilon[\sin(++)\delta_{k,k'-2\pi/L}+\sin(--)\delta_{k,k'+2\pi/L}]\end{aligned}$$

(2-27)

in which the coefficient $\Upsilon\equiv\frac{(a_{v-1}^{\dagger}a_v\sqrt{\frac{v-1}{v}}+b_{v-1}^{\dagger}b_v)\sqrt{v}l_B|\boldsymbol{q}|}{2\sqrt{2}}$, the simplified notations $\sin(++)\equiv\sin[\frac{2\pi l_B^2}{L}(k+\frac{\pi}{L})+\frac{\pi}{4}]$, $\sin(--)\equiv\sin[\frac{2\pi l_B^2}{L}(k-\frac{\pi}{L})-\frac{\pi}{4}]$ and we have applied the relation $\chi_{v-2,v-1}(ql_B)=\sqrt{\frac{v-1}{v}}\chi_{v-1,v}(ql_B)$ in the last step of Eq. (2-27). Similarly, in case that $n=v$ and $n'=v-1$, we have

$$\begin{aligned}&\phi_{n,k}^{\dagger}\cos\frac{n_x\pi x}{L}\cos\frac{n_y\pi y}{L}\phi_{n',k'} \\ &= a_{v}^{*}a_{v-1}\langle v-1,k|\cos\frac{n_x\pi x}{L}\cos\frac{n_y\pi y}{L}|v-2,k'\rangle + b_{v}^{*}b_{v-1}\langle v,k|\cos\frac{n_x\pi x}{L}\cos\frac{n_y\pi y}{L}|v-1,k'\rangle \\ &= -\Upsilon[\sin(+-)\delta_{k,k'-2\pi/L}+\sin(-+)\delta_{k,k'+2\pi/L}]\end{aligned}$$

(2-28)

in which the simplified notations $\sin(+-)\equiv\sin[\frac{2\pi l_B^2}{L}(k+\frac{\pi}{L})-\frac{\pi}{4}]$ and $\sin(-+)\equiv\sin[\frac{2\pi l_B^2}{L}(k-\frac{\pi}{L})+\frac{\pi}{4}]$. Put everything together, we get

$$\Lambda_{cc} = -\Upsilon\sum_k [\sin(++)c^\dagger_{\nu-1,k}c_{\nu,k+\frac{2\pi}{L}} + \sin(--)c^\dagger_{\nu-1,k}c_{\nu,k-\frac{2\pi}{L}}]$$
$$-\Upsilon\sum_k [\sin(+-)c^\dagger_{\nu,k}c_{\nu-1,k+\frac{2\pi}{L}} + \sin(-+)c^\dagger_{\nu,k}c_{\nu-1,k-\frac{2\pi}{L}}] \quad (2\text{-}29)$$

similarly, we obtain

$$\Lambda_{cs} = i\Upsilon\sum_k [\sin(++)c^\dagger_{\nu-1,k}c_{\nu,k+\frac{2\pi}{L}} - \sin(--)c^\dagger_{\nu-1,k}c_{\nu,k-\frac{2\pi}{L}}]$$
$$+i\Upsilon\sum_k [\sin(+-)c^\dagger_{\nu,k}c_{\nu-1,k+\frac{2\pi}{L}} - \sin(-+)c^\dagger_{\nu,k}c_{\nu-1,k-\frac{2\pi}{L}}]$$
$$\Lambda_{sc} = \Upsilon\sum_k [\sin(++)c^\dagger_{\nu,k}c_{\nu-1,k+\frac{2\pi}{L}} - \sin(--)c^\dagger_{\nu,k}c_{\nu-1,k-\frac{2\pi}{L}}]$$
$$+\Upsilon\sum_k [-\sin(+-)c^\dagger_{\nu-1,k}c_{\nu,k+\frac{2\pi}{L}} + \sin(-+)c^\dagger_{\nu-1,k}c_{\nu,k-\frac{2\pi}{L}}] \quad (2\text{-}30)$$
$$\Lambda_{ss} = i\Upsilon\sum_k [\sin(++)c^\dagger_{\nu,k}c_{\nu-1,k+\frac{2\pi}{L}} + \sin(--)c^\dagger_{\nu,k}c_{\nu-1,k-\frac{2\pi}{L}}]$$
$$-i\Upsilon\sum_k [\sin(+-)c^\dagger_{\nu-1,k}c_{\nu,k+\frac{2\pi}{L}} + \sin(-+)c^\dagger_{\nu-1,k}c_{\nu,k-\frac{2\pi}{L}}]$$

in which the summation of wave-vector k runs over all degenerate states in LL $n = \nu$. Introduce new bosonic operators

$$d_1 \equiv \sqrt{\frac{1}{n_B}}\sum_k [\sin(+-)c^\dagger_{\nu-1,k}c_{\nu,k+\frac{2\pi}{L}} + \sin(-+)c^\dagger_{\nu-1,k}c_{\nu,k-\frac{2\pi}{L}}]$$
$$d_2 \equiv \sqrt{\frac{1}{n_B}}\sum_k [\sin(++)c^\dagger_{\nu-1,k}c_{\nu,k+\frac{2\pi}{L}} + \sin(--)c^\dagger_{\nu-1,k}c_{\nu,k-\frac{2\pi}{L}}] \quad (2\text{-}31)$$

and

$$e_1 \equiv \sqrt{\frac{1}{n_B}}\sum_k [\sin(-+)c^\dagger_{\nu-1,k}c_{\nu,k-\frac{2\pi}{L}} - \sin(+-)c^\dagger_{\nu-1,k}c_{\nu,k+\frac{2\pi}{L}}]$$
$$e_2 \equiv \sqrt{\frac{1}{n_B}}\sum_k [\sin(++)c^\dagger_{\nu-1,k}c_{\nu,k+\frac{2\pi}{L}} - \sin(--)c^\dagger_{\nu-1,k}c_{\nu,k-\frac{2\pi}{L}}] \quad (2\text{-}32)$$

in which $n_B = 4eBL^2/h$ is the Landau level degeneracy. We can verify that the new defined bosonic operators satisfy the commutation relation in the ground state and dilute regime as $[d_\eta, d^\dagger_{\eta'}] = \delta_{\eta,\eta'}$ and $[e_\eta, e^\dagger_{\eta'}] = \delta_{\eta,\eta'}$ ($\eta = 1, 2$). With defined bosonic operators, we can finally write the Coulomb potential in Eq. (2-22) as

$$H_{coul} = \frac{1}{2}\tilde{v}_{n_x,n_y}\Upsilon^2 n_B \sum_{\eta}[\chi_\eta(d_\eta + \chi_\eta d_\eta^\dagger)^2 - \chi_\eta(e_\eta - \chi_\eta e_\eta^\dagger)^2] \tag{2-33}$$

where $\chi_1 = -1,\ \chi_2 = 1$. Later on we will see that d_η can be treated as the bosonic bright mode annihilation operators between the transitions $v \to v-1$ coupled to cavity modes $\eta = 1,2$ with the consideration of the condition $|\boldsymbol{q}| l_B \ll 1$ (for the photonic wave vector, this condition is always satisfied), and the dark mode bosonic operators e_η can be discarded since they are small in value and do not couple with the kinetic and interaction part of the total Hamiltonian of the system. Therefore, we obtain

$$H_{coul} = \sum_{\eta=1,2} \hbar V_c\ \chi_\eta(d_\eta + \chi_\eta d_\eta^\dagger)^2 \tag{2-34}$$

where $V_c = \frac{n_B e^2 l_B^2 v\pi}{8\sqrt{2}\varepsilon_0 \varepsilon L^3 \hbar}(a_v^* a_{v-1}\sqrt{\frac{v-1}{v}} + b_v^* b_{v-1})^2$.

Once we get the second quantization form of the Coulomb potential expressed by the Bosonic operators as Eq. (2-34), we can write the kinetic energy part of the Hamiltonian $H_L = H_{1,L} + H_{2,L}$ in LL basis, which is given by Eq. (2-2), as $H_L = \sum_{n,k} E_n c_{n,k}^\dagger c_{n,k}$, where E_n is given by Eq. (2-6) and $c_{n,k}^\dagger$ is Fermi creation operator for the eigenstates $\phi_{n,k}$ defined in Eq. (2-2). In order to obtain the bosonic form of the kinetic Hamiltonian H_L, we calculate the commutation relation $[H_L, d_\eta^\dagger] = \hbar\omega_{eg} d_\eta^\dagger$, where $\omega_{eg} \equiv (E_v - E_{v-1})/\hbar$ is the transition frequency between nearby LLs $n = v-1$ and $n = v$, and obtain the bosonic Hamiltonian as $H_L = \sum_{\eta=1,2} \hbar\omega_{eg} d_\eta^\dagger d_\eta$. Next we give the second quantization procedure for the first order interaction Hamiltonian $H_{1,\text{int}}$. First we write $H_{1,\text{int}}$ in LL basis as

$$H_{\text{int},1} = \sum_{n,n',k,k'} \frac{a_0 t_0 e}{\hbar} a_{n'} b_n^* \langle n,k|(\boldsymbol{A}_{em,x} + i\boldsymbol{A}_{em,y})|n'-1,k'\rangle c_{n,k}^\dagger c_{n',k'}$$
$$+ \sum_{n,n',k,k'} \frac{a_0 t_0 e}{\hbar} a_n^* b_{n'} \langle n-1,k|(\boldsymbol{A}_{em,x} - i\boldsymbol{A}_{em,y})|n',k'\rangle c_{n,k}^\dagger c_{n',k'}$$

(2-35)

meanwhile we can write $\boldsymbol{A}_{em,x}$ as

$$\boldsymbol{A}_{em,x}=\sqrt{\frac{2\hbar}{\varepsilon_0\varepsilon\omega_c V}}[\cos(\frac{2\pi x}{L})\sin(\frac{2\pi y}{L})\cos(\theta)(a_1+a_1^{\dagger})-\cos(\frac{2\pi x}{L})\sin(\frac{2\pi y}{L})(a_2+a_2^{\dagger})] \tag{2-36}$$

in case $n=v-1$, $n'=v$, the second term of Eq. (2-35) $\langle v-2,k|(\boldsymbol{A}_{em,x}-i\boldsymbol{A}_{em,y})|v,k'\rangle\approx 0$, for the first term we have

$$\begin{aligned}&\langle v-1,k|\cos(\frac{2\pi x}{L})\sin(\frac{2\pi y}{L})|v-1,k'\rangle\\&=-\frac{i}{2}\{\cos[\frac{2\pi l_B^2}{L}(k+\frac{\pi}{L})]\delta_{k,k+\frac{2\pi}{L}}-\cos[\frac{2\pi l_B^2}{L}(k-\frac{\pi}{L})]\delta_{k,k-\frac{2\pi}{L}}\}\end{aligned} \tag{2-37}$$

Similarly, we can write $\boldsymbol{A}_{em,y}$ as

$$\boldsymbol{A}_{em,y}=\sqrt{\frac{2\hbar}{\varepsilon_0\varepsilon\omega_c V}}[\sin(\frac{2\pi x}{L})\cos(\frac{2\pi y}{L})\cos(\theta)(a_1+a_1^{\dagger})-\sin(\frac{2\pi x}{L})\cos(\frac{2\pi y}{L})(a_2+a_2^{\dagger})] \tag{2-38}$$

And we have

$$\begin{aligned}&\langle v-1,k|\sin(\frac{2\pi x}{L})\cos(\frac{2\pi y}{L})|v-1,k'\rangle\\&=\frac{1}{2}\{\sin[\frac{2\pi l_B^2}{L}(k+\frac{\pi}{L})]\delta_{k,k+\frac{2\pi}{L}}+\sin[\frac{2\pi l_B^2}{L}(k-\frac{\pi}{L})]\delta_{k,k-\frac{2\pi}{L}}\}\end{aligned} \tag{2-39}$$

Put them together, we obtain

$$\begin{aligned}&\langle v-1,k|(\boldsymbol{A}_{em,x}+i\boldsymbol{A}_{em,y})|v-1,k'\rangle\\&=i\sqrt{\frac{\hbar}{\varepsilon_0\varepsilon\omega_c V}}\{(a_1+a_1^{\dagger})\cos(\theta)[\sin(+-)\delta_{k,k+\frac{2\pi}{L}}+\sin(-+)\delta_{k,k-\frac{2\pi}{L}}]\\&+(a_2+a_2^{\dagger})[\sin(++)\delta_{k,k+\frac{2\pi}{L}}+\sin(--)\delta_{k,k-\frac{2\pi}{L}}]\}\end{aligned} \tag{2-40}$$

in which $\sin(\pm\pm)$ are given by Eq. (2-27). In case of $n = v$, $n' = v-1$, the first term in Eq. (2-35) which is $\langle v,k|(\boldsymbol{A}_{em,x} + i\boldsymbol{A}_{em,y})|v-2,k'\rangle \approx 0$, for the second term we have

$$\begin{aligned}
&\langle v-1,k|(\boldsymbol{A}_{em,x} - i\boldsymbol{A}_{em,y})|v-1,k'\rangle \\
&= -i\sqrt{\frac{\hbar}{\varepsilon_0 \varepsilon \omega_c V}}\{(a_1 + a_1^\dagger)\cos(\theta)[\sin(++)\delta_{k,k+\frac{2\pi}{L}} + \sin(--)\delta_{k,k-\frac{2\pi}{L}}] \\
&+(a_2 + a_2^\dagger)[\sin(+-)\delta_{k,k+\frac{2\pi}{L}} + \sin(-+)\delta_{k,k-\frac{2\pi}{L}}]\}
\end{aligned} \tag{2-41}$$

Add Eq. (2-41) and Eq. (2-40) together, after some algebra we get the first order interaction Hamiltonian as

$$H_{int,1} = \sum_{\eta=1,2} \hbar\Omega_\eta^f (d_\eta + d_\eta^\dagger)(a_\eta + a_\eta^\dagger) \tag{2-42}$$

with $\Omega_1^f = \Omega_2^f cos(\theta)$ and the first order vacuum Rabi frequency of mode two $(\eta = 2)$ is

$$\Omega_2^f = \sqrt{\frac{1}{2\hbar\varepsilon_0 \varepsilon \omega_c V}} \frac{i\sqrt{2} a_v^* b_{v-1} a_0 t_0 e\sqrt{n_B}}{\hbar} \tag{2-43}$$

For the second order interaction Hamiltonian, we can transform the expression

$$\begin{aligned}
k_x + \frac{eA_{0,x}}{\hbar} &= \frac{i\sqrt{2}}{2l_B}(dr^\dagger - dr) \\
k_y + \frac{eA_{0,y}}{\hbar} &= \frac{\sqrt{2}}{2l_B}(dr^\dagger + dr)
\end{aligned} \tag{2-44}$$

in which the operator $dr^\dagger$ is defined as the creation operator of LL states $|n,k\rangle$ in Eq. (2-2). We write the second order interaction Hamiltonian in the second quantization form as

$$\begin{aligned}
H_{2,\text{int}} &= \sum_{n,n',k,k'} \frac{\hbar^2}{4m_0} a_{n'} a_n^* (\alpha+\beta)\langle n,k|[(\boldsymbol{k} + \frac{e\boldsymbol{A}_0}{\hbar})\cdot\frac{e\boldsymbol{A}_{em}}{\hbar} + \frac{e\boldsymbol{A}_{em}}{\hbar}\cdot(\boldsymbol{k} + \frac{e\boldsymbol{A}_0}{\hbar})]|n',k'\rangle c_{n,k}^\dagger c_{n',k'} \\
&+ \sum_{n,n',k,k'} \frac{\hbar^2}{4m_0} b_n^* b_{n'} (\alpha-\beta)\langle n-1,k|[(\boldsymbol{k} + \frac{e\boldsymbol{A}_0}{\hbar})\cdot\frac{e\boldsymbol{A}_{em}}{\hbar} + \frac{e\boldsymbol{A}_{em}}{\hbar}\cdot(\boldsymbol{k} + \frac{e\boldsymbol{A}_0}{\hbar})]|n'-1,k'\rangle c_{n,k}^\dagger c_{n',k'}
\end{aligned} \tag{2-45}$$

Plug the expression of $\boldsymbol{A}_{em}$ into Eq. (2-44) and first consider the case of $n=v-1$, $n'=v$, we obtain

$$\begin{aligned}&\langle n,k|[(\boldsymbol{k}+\frac{e\boldsymbol{A}_0}{\hbar})\cdot\frac{e\boldsymbol{A}_{em}}{\hbar}+\frac{e\boldsymbol{A}_{em}}{\hbar}\cdot(\boldsymbol{k}+\frac{e\boldsymbol{A}_0}{\hbar})]|n',k'\rangle\\&=\frac{e\sqrt{2v}}{2l_B\hbar}[\langle v,k|(A_{em,y}-iA_{em,x})|v,k'\rangle+\langle v-1,k|(A_{em,y}-iA_{em,x})|v-1,k'\rangle]\end{aligned}\tag{2-46}$$

And

$$\begin{aligned}&\langle n-1,k|[(\boldsymbol{k}+\frac{e\boldsymbol{A}_0}{\hbar})\cdot\frac{e\boldsymbol{A}_{em}}{\hbar}+\frac{e\boldsymbol{A}_{em}}{\hbar}\cdot(\boldsymbol{k}+\frac{e\boldsymbol{A}_0}{\hbar})]|n'-1,k'\rangle\\&=\frac{e\sqrt{2(v-1)}}{2l_B\hbar}[\langle v-1,k|(A_{em,y}-iA_{em,x})|v-1,k'\rangle+\langle v-2,k|(A_{em,y}-iA_{em,x})|v-2,k'\rangle]\end{aligned}\tag{2-47}$$

Similarly, in case of $n=v$, $n'=v-1$, we obtain

$$\begin{aligned}&\langle n,k|[(\boldsymbol{k}+\frac{e\boldsymbol{A}_0}{\hbar})\cdot\frac{e\boldsymbol{A}_{em}}{\hbar}+\frac{e\boldsymbol{A}_{em}}{\hbar}\cdot(\boldsymbol{k}+\frac{e\boldsymbol{A}_0}{\hbar})]|n',k'\rangle\\&=\frac{e\sqrt{2v}}{2l_B\hbar}[\langle v,k|(A_{em,y}+iA_{em,x})|v,k'\rangle+\langle v-1,k|(A_{em,y}+iA_{em,x})|v-1,k'\rangle]\end{aligned}\tag{2-48}$$

And

$$\begin{aligned}&\langle n-1,k|[(\boldsymbol{k}+\frac{e\boldsymbol{A}_0}{\hbar})\cdot\frac{e\boldsymbol{A}_{em}}{\hbar}+\frac{e\boldsymbol{A}_{em}}{\hbar}\cdot(\boldsymbol{k}+\frac{e\boldsymbol{A}_0}{\hbar})]|n'-1,k'\rangle\\&=\frac{e\sqrt{2(v-1)}}{2l_B\hbar}[\langle v-1,k|(A_{em,y}+iA_{em,x})|v-1,k'\rangle+\langle v-2,k|(A_{em,y}+iA_{em,x})|v-2,k'\rangle]\end{aligned}\tag{2-49}$$

Adding Eq. (2-47) and Eq. (2-48) together, after some routine calculations we get the second order interaction Hamiltonian as

$$H_{int,2}=\sum_{\eta}\hbar\Omega_{\eta}^{s}(d_{\eta}+d_{\eta}^{\dagger})(a_{\eta}+a_{\eta}^{\dagger})\tag{2-50}$$

with $\Omega_1^s=\Omega_2^s cos(\theta)$ and the second order vacuum Rabi frequency of mode two $(\eta=2)$ is

$$\Omega_2^s = \sqrt{\frac{1}{2\hbar\varepsilon_0\varepsilon\omega_c V}}\frac{e\hbar\sqrt{n_B}}{2m_0 l_B}\left[(\alpha+\beta)a_{\nu-1}^* a_\nu\sqrt{\nu-1}+(\alpha-\beta)b_{\nu-1}^* b_\nu\sqrt{\nu}\right] \tag{2-51}$$

The diamagnetic contribution H_{dia} can be bosonized in a similar way which can be written in form as

$$H_{dia} = \sum_{n,n',k,k'}[a_{n'}a_n^*(\alpha+\beta)\frac{e^2}{4m_0}\langle n-1,k|\boldsymbol{A}_{em}^2|n'-1,k'\rangle + b_{n'}b_n^*(\alpha-\beta)\frac{e^2}{4m_0}\langle n,k|\boldsymbol{A}_{em}^2|n',k'\rangle]c_{n,k}^\dagger c_{n',k'} \tag{2-52}$$

In case of $n=n'$ and $k=k'$, express $\boldsymbol{A}_{em}^2$ in terms of cosine and sine functions, we have

$$\langle n-1,k|\cos^2(\frac{2\pi x}{L})\sin^2(\frac{2\pi x}{L})|n-1,k\rangle = \frac{1}{4}[1+\cos(\frac{4\pi k l_B^2}{L})] \tag{2-53}$$

And

$$\langle n-1,k|\sin^2(\frac{2\pi x}{L})\cos^2(\frac{2\pi y}{L})|n-1,k\rangle = \frac{1}{4}[1-\cos(\frac{4\pi k l_B^2}{L})] \tag{2-54}$$

Plug Eq. (2-52) and Eq. (2-53) into Eq. (2-51), we obtain

$$\begin{aligned}&\langle n-1,k|\boldsymbol{A}_{em}^2|n-1,k\rangle \\ &= \frac{\hbar}{\varepsilon_0\varepsilon\omega_c V}[\cos^2(\theta)(a_1+a_1^\dagger)^2+(a_2+a_2^\dagger)^2-2\cos(\theta)\cos(\frac{4\pi k l_0^2}{L})(a_1+a_1^\dagger)(a_2+a_2^\dagger)]\end{aligned} \tag{2-55}$$

Note that the above expression does not depend on which LL that we apply. Therefore, by setting $n=n'$, $k=k'$ and summing over k provides the LL degeneracy n_B. Replace the number operator $c_{n,k}^\dagger c_{n',k'}$ by the its expectation value $\langle c_{n,k}^\dagger c_{n,k}\rangle = \Theta(\nu-1-n)$ in the electronic ground state $|F\rangle = \prod_{n=0}^{\nu-1}\prod_{k=1}^{n_B}c_{n,k}^\dagger|0\rangle$, finally we can obtain

$$H_{dia} = \sum_{n=0}^{\nu-1}\sum_{k}\frac{e^2\hbar}{4\varepsilon_0\varepsilon\omega_c m_0 V}[a_n a_n^*(\alpha+\beta)+b_n b_n^*(\alpha-\beta)][\cos^2(\theta)(a_1+a_1^\dagger)^2+(a_2+a_2^\dagger)^2] \\ = \sum_{\eta=1,2}\hbar D_\eta(a_\eta+a_\eta^\dagger)^2 \quad (2\text{-}56)$$

with $D_1 = D_2 cos^2(\theta)$ and the diamagnetic terms D_2 of mode two $(\eta = 2)$ is

$$D_2 = \frac{n_B e^2}{4\varepsilon_0\varepsilon\omega_c m_0 V}\sum_{n=0}^{\nu-1}\left[a_n^* a_n(\alpha+\beta)+b_n^* b_n(\alpha-\beta)\right] \quad (2\text{-}57)$$

At this stage, we finally obtain the total Hamiltonian of the system written in second quantization form as

$$H_{total} = \sum_{\eta=1,2}\hbar[\omega_{eg}d_\eta^\dagger d_\eta + \Omega_\eta(d_\eta+d_\eta^\dagger)(a_\eta+a_\eta^\dagger) + D_\eta(a_\eta+a_\eta^\dagger)^2 + V_c\,\chi_\eta(d_\eta+\chi_\eta d_\eta^\dagger)^2] \quad (2\text{-}58)$$

in which the vacuum Rabi frequency $\Omega_\eta = \Omega_\eta^f + \Omega_\eta^s$.

By diagonalizing the kinetic and Coulomb Hamiltonian, we can obtain the Hamiltonian written in magnetoplasmon modes as

$$H_{Coul} + H_L = \sum_{\eta=1,2}\hbar\omega_p g_\eta^\dagger g_\eta + const \quad (2\text{-}59)$$

where $g_\eta = u_\eta d_\eta + v_\eta d_\eta^\dagger$ are called the magnetoplasmon mode annihilation operator, and we have $\omega_p = \sqrt{\omega_{eg}(\omega_{eg}+4V_c)}$, $u_\eta = -\chi_\eta\frac{\omega_p+\omega_{eg}}{2\sqrt{\omega_{eg}\omega_p}}$, $v_\eta = \frac{\omega_{eg}-\omega_p}{2\sqrt{\omega_{eg}\omega_p}}$.

Then we can write the total Hamiltonian describing photonic and magnetoplasmon modes as

$$H_{total} = \sum_{\eta=1,2}\hbar[\omega_p g_\eta^\dagger g_\eta + \omega_c a_\eta^\dagger a_\eta + \tilde{\Omega}_\eta(g_\eta^\dagger + g_\eta)(a_\eta+a_\eta^\dagger) + D_\eta(a_\eta+a_\eta^\dagger)^2] \quad (2\text{-}60)$$

where $\tilde{\Omega}_\eta = (u_\eta - v_\eta)\Omega_\eta$.

Introducing polariton operators $p_{j,\eta} = c_{j,\eta}g_\eta^\dagger + d_{j,\eta}a_\eta^\dagger + e_{j,\eta}g_\eta + f_{j,\eta}a_\eta$, we can write the total Hamiltonian Eq. (2-10) in polariton basis as

$$H_{total} = \sum_{j,\eta} \hbar\omega_{j,\eta} p^{\dagger}_{j,\eta} p_{j,\eta} + const \tag{2-61}$$

here j indicates upper and lower polaritons and the commutation relation $[p_{j,\eta}, p^{\dagger}_{j',\eta}] = \delta_{j,j'}$. By calculating the commutation relation $[p_{j,\eta}, H] = \hbar\omega_{j,\eta} p_{j,\eta}$ we can obtain a 4 by 4 matrix which can be written as

$$\begin{pmatrix} \omega_c + 2D_\eta & \tilde{\Omega}_\eta & -2D_\eta & -\tilde{\Omega}_\eta \\ \tilde{\Omega}_\eta & \omega_p & -\tilde{\Omega}_\eta & 0 \\ 2D_\eta & \tilde{\Omega}_\eta & -\omega_c - 2D_\eta & -\tilde{\Omega}_\eta \\ \tilde{\Omega}_\eta & 0 & -\tilde{\Omega}_\eta & -\omega_p \end{pmatrix} \tag{2-62}$$

By diagonalizing the matrix, we can obtain the eigenfrequency of the polaritons. Meanwhile, the critical value of $\tilde{\Omega}$ beyond which the system may enter super-radiant phase regime is $\tilde{\Omega}_c = \sqrt{\omega_p(\omega_c + 4D)}/2$, the phase transition occur at LL $\nu = 200$ with $B = 0.75T$ which we will show below. Noted that in monolayer MoS_2, similar to graphene, a quantum critical value exist because $D_2\omega_{eg}$ is smaller than Ω_2^2, e.g. with $\nu = 50$ and $B = 1T$, $D_2\omega_{eg}/\Omega_2^2 \approx 0.5$ [24]. Above this critical value, a spontaneous coherence of light and matter appears, the ground state becomes twice degenerate and the system enters superradiant quantum phase.

2.2 Numerical Results and Discussions

As written in Eq. (2-58) , we have obtained the vacuum Rabi frequency of monolayer MoS_2 system and then can characterize the "intrinsic" strength of the transition *i.e.* the ratio between vacuum Rabi frequency Ω_2 with LL transition frequency ω_{eg}, which is shown in Fig. 2-3. The results show that the dimensionless vacuum Rabi frequency Ω_2/ω_{eg} can be comparable to or even larger than 1 for small magnetic field B and large enough doping density ρ. We can conclude that, similar with graphene, monolayer MoS2-cavity system can also enter the ultrastrong coupling regime. Noted that, in our work, the carrier doping is induced by the external electric fields and their relations can be simply calculated according to Ref. [66]. But as discussed in Ref. [64], the external electric field will also influence the electron-hole

asymmetry thus the band structure of MoS_2. For the sake of simplicity, we adopt the formula as used in Ref. [64] which describes the relation between electron-hole asymmetry and electric field.

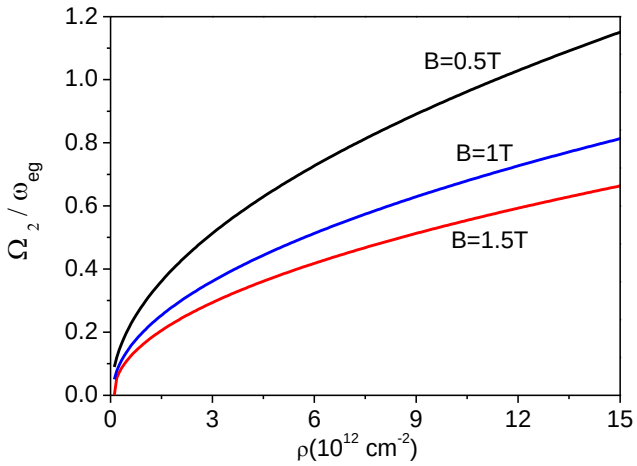

Fig. 2-3 The dimensionless vacuum Rabi frequency Ω_2/ω_{eg} versus the doping density ρ. Other parameters are L_z = 1mm, $L = 8L_z$ and $\omega_c = 0.49$ THz rad^{-1}. ω_{eg} is the cyclotron transition frequency between the last occupied LL with the first unoccupied one.

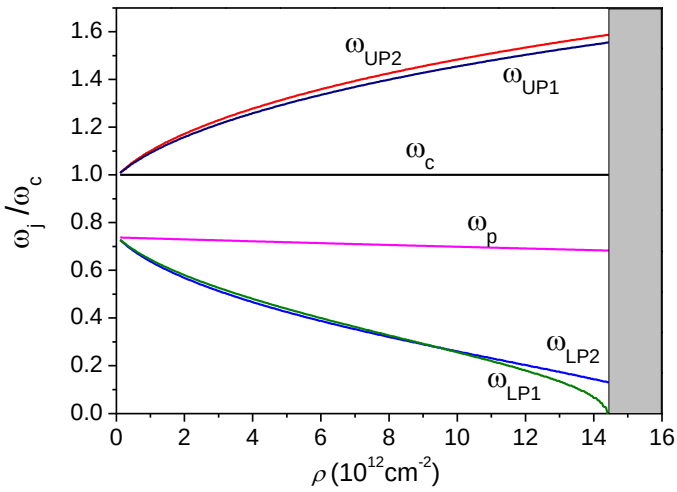

Fig. 2-4 Normalized frequencies of LP and UP branches of magnetopolariton as a function of doping density for $\eta = 1$ and $\eta = 2$. Parameters are B = 0.75T, L_z = 1mm, $L = 8L_z$ and $\omega_c = 0.49$ THz rad^{-1}, the critical density for phase transition is $\rho_c = 1.44\times10^{13} cm^{-2}$.

Using Eq. (2-62) we can calculate the magnetopolariton dispersion. In the Fig. 2-4, we show the carrier density dependences of frequencies of magnetopolariton normalized to the cavity mode, where the low polariton (LP) and upper polariton (UP) branches are the two spectrally separated light-matter eigenstates in strong coupling regime. In contrast to the conventional semiconductor materials (e.g. GaAs), monolayer cavity-MoS_2 resonator, as a 2D semiconductor material, shows the existence of quantum critical point ($\rho_c = 1.44\times10^{13} cm^{-2}$ in our considered parameter) beyond which the normal ground state becomes unstable. This quantum critical point exits in MoS_2 system due to smaller diamagnetic term, i.e., $D_2 < \Omega_2^2/\omega_{eg}$ as discussed in chapter 1.3. In conventional semiconductors, the diamagnetic term is even dominant in ultrastrong coupling regime between a cavity resonator and cyclotron transitions.

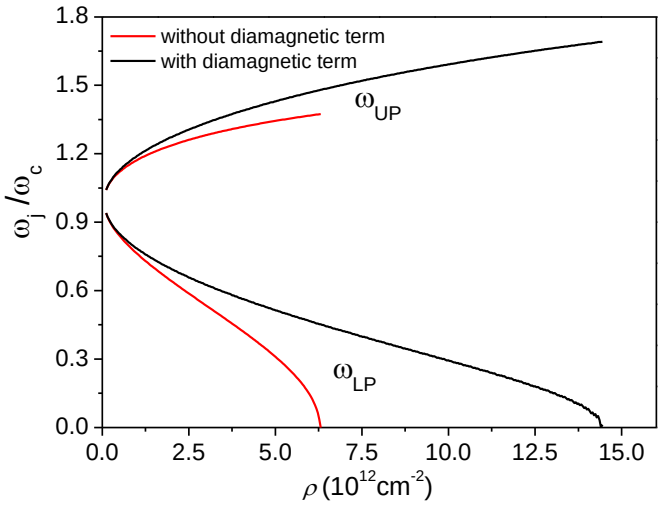

Fig. 2-5 Normalized frequencies of LP and UP branches of magnetopolariton as a function of doping density with and without the diamagnetic term for the second mode $\eta = 2$. Parameters are B = 1T, L_z = 1mm, L = $8L_z$ and ω_c = 0.49 THz rad^{-1}, the critical density for phase transition is $\rho_c = 1.44\times10^{13} cm^{-2}$ and $\rho_c = 6.30\times10^{12} cm^{-2}$ with and without diamagnetic terms respectively.

In contrast to graphene, the diamagnetic term can still play an important role in determining magnetopolariton dispersion for monolayer MoS_2 system, as shown in Fig. 2-5. The quantum critical point of MoS_2 resonator can be greatly increased from

$\rho_c = 6.30\times10^{12}cm^{-2}$ to $\rho_c = 1.44\times10^{13}cm^{-2}$ when considering the diamagnetic term. On the other hand, the diamagnetic term arises from electron-hole asymmetry which indicates that electron-hole asymmetry can influence the quantum phase transition.

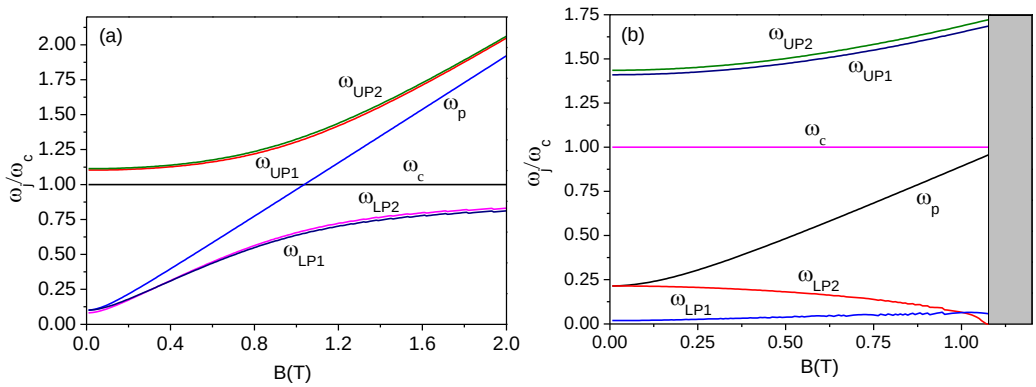

Fig. 2-6 (a) Normalized frequencies of LP and UP branches of magnetopolariton as a function of magnetic field *B*, doping density is $\rho = 2.81\times10^{12}cm^{-2}$ (b) Normalized frequencies of LP and UP branches of magnetopolariton as a function of magnetic field *B*, doping density is $\rho = 1.42\times10^{13}cm^{-2}$ which is just below the critical density, the critical value of magnetic field *B* for phase transition is B_c = 1.06T beyond which the system may enter super-radiant phase regime.

We close the analysis by considering the effect of magnetic field on magnetopolariton at doping density far away from the quantum critical point (Fig. 2-6 (a)) and one just below the critical point (Fig. 2-6 (b)). As a 2D semiconductor material, MoS_2 system has a similar magnetic field dependent magnetopolariton dispersion curve with a 2D electron gas in quantum wells if the doping density is far away from the critical density. However, when doping density is just below the critical point, the dispersion curve is very different as depicted in Fig. 2-6 (b). As the magnetic field increases, a strong asymmetric dispersion is exhibited, which shows the signature of such phase transition.

As a conclusion of the chapter 2, we theoretically investigate the cavity QED in monolayer MoS_2 system under perpendicular magnetic field with the consideration of electron-hole asymmetry. The results show that MoS_2 system can enter the ultrastrong light-matter coupling regime. But, in contrast to conventional semiconductors, the semiconductor monolayer MoS_2 system shows a quantum phase transition. In monolayer MoS_2 resonator, the diamagnetic term can still play an

important role in determining magnetopolariton dispersion which is different from monolayer graphene system. The diamagnetic term arises from electron-hole asymmetry which indicates that electron-hole asymmetry can influence the quantum phase transition. Our study provides a theoretical foundation for the observation and investigation of cavity QED for fundamental studies and quantum applications in MoS_2 system.

3. CAVITY QED OF BLACK PHOSPHORENE

In the previous chapter 2, we investigated the superradiant phase transition in monolayer MoS2-cavity system, and showed that in contrast with normal semiconductor quantum wells, the monolayer MoS2 shows a vacuum instability. Now we can proceed to investigate another 2D material which is the black phosphorene (BP) and show some resemblance and difference compared with the monolayer MoS2. The set up of the cavity-BP system in this chapter follows the chapter 2.

3.1 Theoretical Formulations

The BP has attracted massive attentions because of its unique electronic properties and novel practical applications in nanoelectronics [67]–[71]. The evidence of a large anisotropy on the effective mass has also been explored by researchers using various methods [72]–[74]. With the application of the tight-binding model and the effective $\boldsymbol{k}\cdot\boldsymbol{p}$ Hamiltonian, people also found that the Landau level (LL) spectra of phosphorene under a perpendicular magnetic field are similar with that in conventional semiconductor two dimensional gases [75], [76]. However, the cavity QED properties of such unique anisotropic system remain unexplored. One open question is whether quantum phase transition will occur and how the anisotropic behavior influences the cavity QED properties of the BP system.

Using the tight binding model proposed in Ref. [72] and expanding the structure factors around the Gamma point, retaining the terms up to second-order in wave-vector k, we can get the Hamiltonian as

$$H_k = \begin{pmatrix} u_0+\eta_x k_x^2+\eta_y k_y^2 & \delta+\gamma_x k_x^2+\gamma_y k_y^2+i\chi k_y \\ \delta+\gamma_x k_x^2+\gamma_y k_y^2-i\chi k_y & u_0+\eta_x k_x^2+\eta_y k_y^2 \end{pmatrix} \tag{3-1}$$

in which the parameters are $u_0 = -0.42eV$, $\eta_x = 0.58eV\cdot\text{Å}^2$, $\eta_y = 1.01eV\cdot\text{Å}^2$, $\delta = 0.76eV$, $\chi = 5.25eV\cdot\text{Å}$, $\gamma_x = 3.93eV\cdot\text{Å}^2$ and $\gamma_y = 3.83eV\cdot\text{Å}^2$ [60]. Apply the magnetic field with the gauge $\boldsymbol{A} = (-By, 0, 0)$ perpendicular to the plane of the layer and make the Landau-Peierls substitution $\boldsymbol{k} \to \boldsymbol{k} + \frac{e\boldsymbol{A}}{\hbar}$, define new operators as

$\alpha = \frac{1}{\sqrt{2}l_B}(y + l_B^2 \frac{d}{dy})$, $\alpha^\dagger = \frac{1}{\sqrt{2}l_B}(y - l_B^2 \frac{d}{dy})$ with the magnetic length $l_B \equiv \sqrt{\frac{\hbar}{eB}}$, then perform a Bogoliubov transformation

$$\begin{aligned} c &= \alpha^\dagger \cosh v + \alpha \sinh v \\ c^\dagger &= \alpha \cosh v + \alpha^\dagger \sinh v \end{aligned} \tag{3-2}$$

we can get the parameter v by solving $\tanh 2v = \mu_2 / \mu_1$ with $\mu_1 = \frac{\eta_x + \eta_y + \gamma_x + \gamma_y}{2} + \frac{\chi^2}{4\delta}$ and $\mu_2 = \frac{\eta_x - \eta_y + \gamma_x - \gamma_y}{2} - \frac{\chi^2}{4\delta}$. Finally we can obtain the wave-function for the LLs state by applying the ansatz as [60]

$$\begin{pmatrix} \phi_+ \\ \phi_- \end{pmatrix} = N_o \begin{pmatrix} |n, k_x\rangle \\ \frac{\chi}{2\sqrt{2}\delta l_B}(\alpha - \alpha^\dagger)|n, k_x\rangle \end{pmatrix} \tag{3-3}$$

in which $|n, k_x\rangle$ are LL states defined as $\sqrt{n+1}|n+1, k_x\rangle = c^\dagger |n, k_x\rangle$, N_o is the factor to normalize the wave-function. In this work, we assume the Fermi level is within the conduction band, therefore, the transformed Hamiltonian for the electronic branches can be given as

$$H_L = u_0 + \delta + \hbar\omega_e(c^\dagger c + \frac{1}{2}) \tag{3-4}$$

with $\omega_e = \frac{eB}{\sqrt{m_x^e m_y^e}}$ where the parameters are $m_x^e \equiv \frac{\hbar^2}{2(\eta_x + \gamma_x)}$ and $m_y^e \equiv \frac{\hbar^2}{2(\eta_y + \gamma_y + \chi^2 / 2\delta)}$.

In this work, we assume zero temperature in the rest of the calculations to ensure the cyclotron transition energy is larger than the thermal energy. Furthermore, we consider a rectangular microcavity that has the volume $V = L_z L^2$ with the monolayer BP material placed at the center of the cavity perpendicular to the z direction as depicted in Fig. 3-1 (see Appendix B for more information of this cavity). The cavity length L_z in the z direction is much smaller than the cavity transverse size L.

Therefore, we can restrict our study to the particular photon mode with $n_z = 1$, neglecting all the higher-lying modes $n_z > 1$. As can be read from Eq. (3-1), the light-matter interaction Hamiltonian expanded in first order can be given as

$$H_{\text{int}} = \begin{pmatrix} 0 & i\chi \dfrac{eA_y^{em}}{\hbar} \\ -i\chi \dfrac{eA_y^{em}}{\hbar} & 0 \end{pmatrix} \tag{3-5}$$

in which electromagnetic vector potential of the cavity photon modes can be given as

$$\boldsymbol{A}_{em} = \sum_{\eta=1,2} \sqrt{\frac{\hbar}{2\varepsilon_0 \varepsilon \omega_c V}} \boldsymbol{u}_\eta (a_\eta + a_\eta^\dagger) \tag{3-6}$$

where a_η is the annihilation operator for a given photon mode $\eta = 1,2$, $\varepsilon = 3$ is the cavity dielectric constant for monolayer BP system [77]. Next we apply the lowest cavity mode, which is quasi-resonant to the considered cyclotron LL transition, with wave vector $\boldsymbol{q} = (q_x, q_y, q_z) = (\pi / L, \pi / L, \pi / L_z)$ and the cavity frequency $\omega_c = \pi c / (L_z \sqrt{\varepsilon})$, the modes can be given as

$$u_1 = \begin{pmatrix} 2cos(\pi x / L) sin(\pi y / L) cos(\theta) \\ 2sin(\pi x / L) cos(\pi y / L) cos(\theta) \\ 0 \end{pmatrix}, u_2 = \begin{pmatrix} -2cos(\pi x / L) sin(\pi y / L) \\ 2sin(\pi x / L) cos(\pi y / L) \\ 0 \end{pmatrix} \tag{3-7}$$

where $cos(\theta) = 1/\sqrt{1+8(L_z / L)^2}$.

We can proceed to write the interaction Hamiltonian in second quantization form as

$$\begin{aligned} H_{\text{int}} &= \begin{pmatrix} \phi_+^\dagger & \phi_-^\dagger \end{pmatrix} \begin{pmatrix} 0 & i\chi \dfrac{eA_y^{em}}{\hbar} \\ -i\chi \dfrac{eA_y^{em}}{\hbar} & 0 \end{pmatrix} \begin{pmatrix} \phi_+ \\ \phi_- \end{pmatrix} \\ &= |N_o|^2 [\langle n, k_x | \frac{i\chi^2 eA_y^{em}}{2\sqrt{2}\delta l_B \hbar} (\alpha - \alpha^\dagger) | n', k_x' \rangle + \langle n, k_x | \frac{i\chi^2 e(\alpha - \alpha^\dagger)}{2\sqrt{2}\delta l_B \hbar} A_y^{em} | n', k_x' \rangle] d_{n,k_x}^\dagger d_{n',k_x'} \end{aligned} \tag{3-8}$$

in which $d^{\dagger}_{n,k_x}$ represents the creation operator for the state Eq. (3-3) and summing over k_x provides the LL degeneracy $n_B = 4eBL^2/h$, note that $d^{\dagger}_{n,k_x}$ is different from $c^{\dagger}_{n,k_x}$. Furthermore, we can write H_{int} in LL basis between the transitions $n-1 \to n$ as

$$\begin{aligned} H_{\text{int}} &= \sum_{k_x,k'_x} \frac{i\chi^2 eN_o^2}{2\sqrt{2}\delta\hbar l_B} \langle n,k_x | (\alpha - \alpha^{\dagger}) A_y^{em} | n-1,k'_x \rangle d^{\dagger}_{n,k_x} d_{n-1,k'_x} \\ &+ \sum_{k_x,k'} \frac{i\chi^2 eN_o^2}{2\sqrt{2}\delta\hbar l_B} \langle n-1,k'_x | A_y^{em} (\alpha - \alpha^{\dagger}) | n,k_x \rangle d^{\dagger}_{n-1,k'_x} d_{n,k_x} \end{aligned} \tag{3-9}$$

Starting from Eq. (3-9), we need to simplify the expression

$$\langle n,k_x | (\alpha - \alpha^{\dagger}) A_y^{em} | n-1,k'_x \rangle \tag{3-10}$$

First by the reverse transformation, we can write the operators α ($\alpha^{\dagger}$) in terms of operators c ($c^{\dagger}$) as

$$\begin{aligned} \alpha &= -c\sinh v + c^{\dagger}\cosh v \\ \alpha^{\dagger} &= -c^{\dagger}\sinh v + c\cosh v \end{aligned} \tag{3-11}$$

By substituting the above expression into Eq. (3-10), we get

$$\begin{aligned} &\langle n,k_x | (\alpha - \alpha^{\dagger}) A_y^{em} | n-1,k'_x \rangle \\ &= \langle n,k_x | (\cosh v - \sinh v)(c - c^{\dagger}) A_y^{em} | n-1,k'_x \rangle \\ &= (\cosh v - \sinh v) \sqrt{\frac{n\hbar}{2\varepsilon_0 \varepsilon \omega_c V}} \frac{\cos(\theta)}{2i} (a_1 + a_1^{\dagger}) [\exp(\frac{i\pi l_B^2 (k_x + k'_x)}{L} \delta_{k_x,k'_x - \frac{2\pi}{L}} \\ &- \exp(\frac{i\pi l_B^2 (k_x + k'_x)}{L} \delta_{k_x,k'_x + \frac{2\pi}{L}} - \exp(\frac{-i\pi l_B^2 (k_x + k'_x)}{L} \delta_{k_x,k'_x - \frac{2\pi}{L}} - \exp(\frac{-i\pi l_B^2 (k_x + k'_x)}{L} \delta_{k_x,k'_x + \frac{2\pi}{L}}] \\ &+ [a_2 \text{ mode}] \end{aligned} \tag{3-12}$$

in which [a_2 mode] stands for similar expression for the second optical polarization mode a_2. Bearing in mind that we are dealing with the cyclotron transitions between the last occupied LL $n = v-1$ with the first unoccupied one $n = v$, after some algraba we can get H_{int} as

$$H_{\text{int}} = \frac{i\chi^2 eN_o^2}{\delta l_B}\sqrt{\frac{n}{2\hbar\varepsilon_0\varepsilon\omega_c V}}(\cosh v - \sinh v)\cos(\theta)(a_1 + a_1^\dagger)$$
$$[\sin(+)d^\dagger_{n,k_x} d_{n-1,k_x+\frac{2\pi}{L}} + \sin(-)d^\dagger_{n,k_x} d_{n-1,k_x-\frac{2\pi}{L}} - \sin(+)d^\dagger_{n-1,k_x+\frac{2\pi}{L}} d_{n,k_x} - \sin(-)d^\dagger_{n-1,k_x-\frac{2\pi}{L}} d_{n,k_x}]$$
$$+[a_2 \text{ mode}]$$

(3-13)

in which the simplified symbol $\sin(+) \equiv \sin[\frac{2\pi}{L}(k+\frac{\pi}{L})l_B^2]$ and $\sin(-) \equiv \sin[\frac{2\pi}{L}(k-\frac{\pi}{L})l_B^2]$. We can further define the bosonic mode annihilation operator between the transitions $n-1 \to n$ as

$$b = \sqrt{\frac{1}{n_B}}\sum_{k_x,\pm}\sin[\frac{\pi}{L}(k \pm \frac{\pi}{L})l_B^2]d^\dagger_{n-1,k_x\pm\pi/L} d_{n,k_x} \tag{3-14}$$

which satisfies the commutation relation in the ground state in dilute regime as $[b, b^\dagger] = 1$. With the new defined bosonic operator, we can get the interaction Hamiltonian as

$$H_{\text{int}} = \frac{i\chi^2 eN_o^2}{2\delta l_B}\sqrt{\frac{nn_B}{\hbar\varepsilon_0\varepsilon\omega_c V}}(\cosh v - \sinh v)\cos(\theta)(a_1 + a_1^\dagger)(b^\dagger - b) + [a_2 \text{ mode}]$$

(3-15)

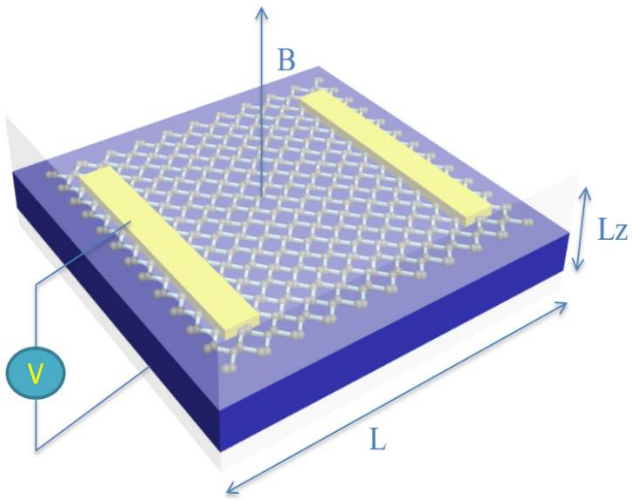

Fig. 3-1 Sketch of a cavity resonator embedding a monolayer BP material with a uniform and static magnetic field B applied perpendicular to the material. Cavity walls in all three directions are perfectly conducting.

Therefore, we can get kinetic Hamiltonian and interaction Hamiltonian shown as

$$H_L = \hbar\omega_e b^\dagger b \tag{3-16}$$

$$H_{\text{int}} = \sum_{\eta=1,2} i\hbar\Omega_\eta (a_\eta + a_\eta^\dagger)(b^\dagger - b) \tag{3-17}$$

where $\Omega_2 = \frac{\chi^2 e N_o^2}{2\delta\hbar l_B}\sqrt{\frac{n_B n}{\varepsilon_0\varepsilon\omega_c\hbar V}}(\cosh v - \sinh v)$, $\Omega_1 = \Omega_2\cos(\theta)$, $\omega_e = \frac{eB}{\sqrt{m_x^e m_y^e}}$ and the Hamiltonian of the cavity fields reads

$$H_{photon} = \sum_{\eta=1,2} \hbar\omega_c a_\eta^\dagger a_\eta \tag{3-18}$$

where $\omega_c = \pi c/(L_z\sqrt{\varepsilon})$ is the frequency of the lowest photon mode.

Introducing polariton operators $p_j = X_j a_1 + Y_j a_2 + Z_j b + \tilde{X}_j a_1^\dagger + \tilde{Y}_j a_2^\dagger + \tilde{Z}_j b^\dagger$, we can write the total Hamiltonian in polariton basis as

$$H = \sum_{j=1,2,3} \hbar\omega_j p_j^\dagger p_j + const. \tag{3-19}$$

Here j indicates three branches of polaritons and we have the commutation relation $[p_j, p_{j'}^\dagger] = \delta_{j,j'}$. By calculating the commutation relation $[p_j, H] = \hbar\omega_j p_j$ we can obtain a 6 by 6 matrix which can be written as

$$\begin{pmatrix} \omega_c & 0 & i\Omega_1 & 0 & 0 & i\Omega_1 \\ 0 & \omega_c & i\Omega_2 & 0 & 0 & i\Omega_2 \\ -i\Omega_1 & -i\Omega_2 & \omega_e & i\Omega_1 & i\Omega_2 & 0 \\ 0 & 0 & i\Omega_1 & -\omega_c & 0 & i\Omega_1 \\ 0 & 0 & i\Omega_2 & 0 & -\omega_c & i\Omega_2 \\ i\Omega_1 & i\Omega_2 & 0 & -i\Omega_1 & -i\Omega_2 & -\omega_e \end{pmatrix} \tag{3-20}$$

by diagonalizing the matrix, we can obtain three branches of polaritons which we name as upper, middle and lower polaritons as depicted in Fig. 3-3.

3.2 Numerical Results and Discussions

Since we obtained the vacuum Rabi frequency of BP system as given in Eq. (3-17), we can characterize the "intrinsic" strength of the transition *i.e.* the ratio between vacuum Rabi frequency Ω_2 with LL transition frequency ω_e, which is shown in Fig. 3-2. The result shows that the dimensionless vacuum Rabi frequency Ω_2 / ω_e can be comparable to or even larger than 1 for small magnetic field B and large enough doping density. We can conclude that, as is the case for other 2D materials, monolayer BP system can also enter the ultrastrong coupling regime.

In the Fig. 3-3, we show the carrier density dependences of frequencies of magnetopolariton normalized to the lowest lying cavity mode, these are three spectrally separated light-matter eigenstates obtained from Eq. (3-20) in strong coupling regime. The Fig. 3-3(a) shows the frequency of the lowest lying branch of polaritons while the Fig. 3-3(b) shows the middle and upper ones. As we can see from Fig. 3-3(a), there exists a quantum critical point ($\rho_c = 1.22 \times 10^{12} cm^{-2}$ in our considered parameter) beyond which the normal ground state becomes unstable. The monolayer BP resonator, as a 2D semiconductor material, shows three branches of polaritons due to the missing of the first order of wave-vector k_x in the tight binding Hamiltonian as shown in Eq. (3-1). Furthermore, in contrast with other 2D materials, this anisotropic feature of its Hamiltonian also results large energy gap between the three branches of polaritons. The energy gap between the lower polariton with the upper one is about the same magnitude as the energy of the cavity mode; meanwhile, the frequency of the middle polariton is exactly the coupling photon frequency ω_c which is just a trivial solution of the Eq. (3-20).

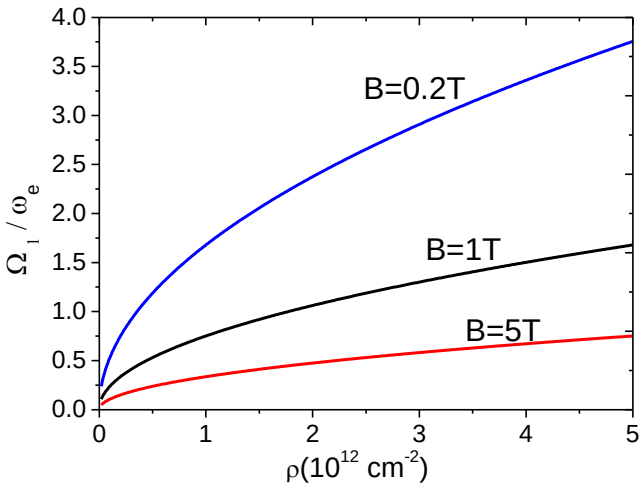

Fig. 3-2 The dimensionless vacuum Rabi frequency Ω_1 / ω_e versus the doping density ρ. Other parameters are L_z = 1mm, L = 8L_z. and $\omega_c = 0.54$ THz rad^{-1}. ω_e is the cyclotron transition frequency between the last occupied LL with the first unoccupied one.

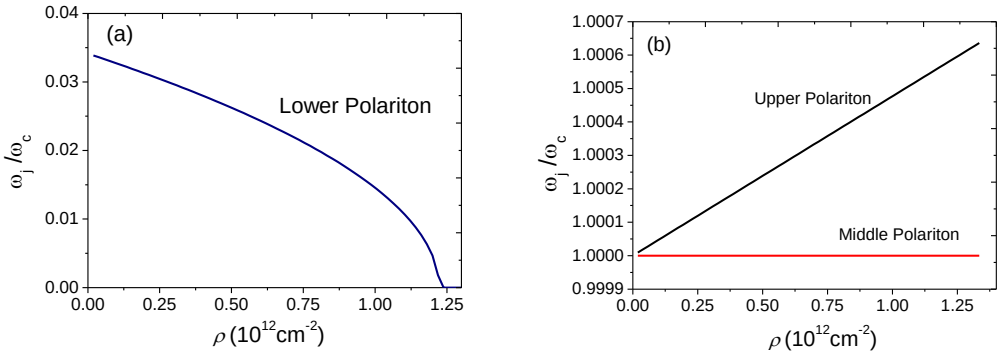

Fig. 3-3 (a) Normalized frequencies of the lower branch of magnetopolariton as a function of doping density, the vacuum instability occurs at $\rho = 1.24\times10^{12} cm^{-2}$ with magnetic field $B = 200mT$. (b) Normalized frequencies of one upper and one middle branches of magnetopolariton as a function of doping density, the Middle branch of polaritons is a trivial solution of the Eq. (3-20).

The Fig. 3-4 shows the magnetic field dependent of the magnetopolariton dispersion curve, the Fig. 3-4(a) shows that the vacuum instability occurs at $B = 258mT$ with doping density $\rho = 1.22\times10^{12} cm^{-2}$. As similar with the carrier density dependences of frequencies of magnetopolariton displayed in Fig. 3-3, the

energy gap between three branches of polaritons is much larger than the other 2D materials [78], [79].

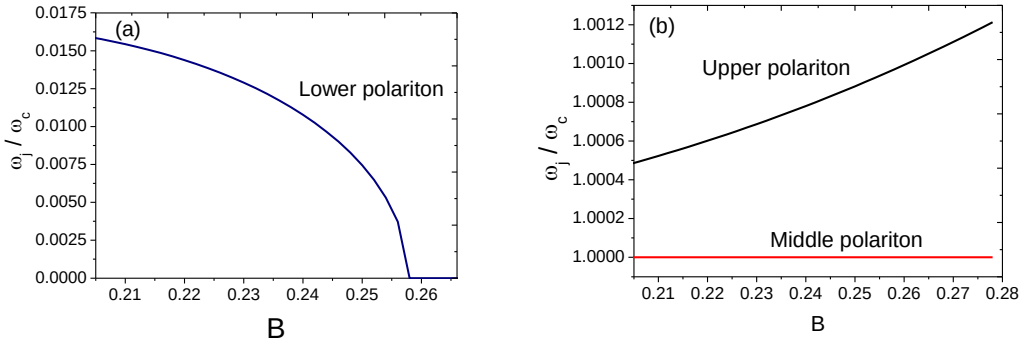

Fig. 3-4 (a) Normalized frequencies of the lower branch of magnetopolariton as a function of magnetic field *B*, the vacuum instability occurs at $B = 258mT$ with doping density $\rho = 1.22 \times 10^{12} cm^{-2}$ and the LL at $n = 50$ (b) Normalized frequencies of one upper and one middle branches of magnetopolariton as a function of magnetic field *B*, doping density is $\rho = 1.22 \times 10^{12} cm^{-2}$, the Middle branch of polaritons is a trivial solution of the Eq. (3-20).

As a conclusion of this chapter, we theoretically investigated the cavity QED in monolayer BP system under a perpendicular magnetic field. The results show that BP system can enter the ultrastrong light-matter coupling regime and, similar with some other 2D materials, the quantum phase transition occurs at a large doping density or a large magnetic field magnitude. However, in contrast with some other 2D materials, the BP system shows three branches of polaritons and the energy gap between these polaritons is much larger, this is caused by the anisotropic behavior displayed in the tight binding Hamiltonian of the BP system. Our study provides a theoretical foundation for the observation and investigation of cavity QED for fundamental studies and quantum applications in monolayer BP system.

4. MULTI-MODE SUPERRADIANT PHASE TRANSITION IN GRAPHENE

In previous chapter, we theoretically investigated the single-mode quantum phase transition in MoS2 and BP systems and showed the characteristics of the normal phase in these materials. In this chapter, we proceed to investigate the multi-mode quantum phase transition in graphene system and show the complete spectrum in both the normal and superradiant phases, furthermore, some differences between the single-mode Dicke model with the multi-mode Dicke model is analyzed in this chapter. The set up of the cavity in this chapter is one-dimentional which is different with previous chapters, we will see in this chapter that such change of the shape of cavity is a necessary condition in order to investigate the multi-modes coupling.

4.1 Theoretical Formulations

Researchers found the two dimensional materials, such as graphene, imbedded in an optical cavity resonator indeed show a quantum instability at certain doping value due to negligible A^2 term [28]. However, such systems can only be described within the normal phase scope so far, an open question is what is beyond the quantum instability point and whether superradiant phase will emerge in such systems. In this chapter, in order to give an answer to this question, we present a microscopic theory to describe the physics of graphene imbedded in an optical cavity resonator under perpendicular magnetic field. We show that the physics behind such system can be modelled as a multi-mode Dicke model and the superradiant phase indeed emerge from the system when passing the vacuum instability point. We also point out that in order to observe the quantum phase transition in the system, one need not to enter the ultra-strong coupling regime, which, in fact, is in contrast with the single mode case.

In the vicinity of the two inequivalent Dirac points K and K' of graphene electronic band structure, the low energy Hamiltonian can be written as $H_L = \hbar v_F (\zeta k_x \sigma_x + k_y \sigma_y)$ where $\sigma_i (i = x, y)$ are Pauli matrices, $v_F \approx 10^6\, m/s$ is the Fermi velocity and $\zeta = \pm$ is the valley index. In this work, a static and uniform magnetic field $\boldsymbol{B}$ is applied along the z axis perpendicularly to the graphene plane. As long as the lattice constant a is much smaller than the magnetic length

$l_0 = \sqrt{\hbar/(eB)}$, we can perform the Landau-Peierls substitution which replace $\hbar\boldsymbol{k}$ with $\boldsymbol{\Pi} = \hbar\boldsymbol{k} + e\boldsymbol{A}_0$ where $\boldsymbol{A}_0(\boldsymbol{r}) = (-By/2, Bx/2, 0)$ is the vector potential in symmetric gauge. This yields the LL states in conduction band in K and K' valleys as $\phi^{\dagger}_{n,l,K} = \left(i\langle n-1,l|, \langle n,l|\right)/\sqrt{2}$ and $\phi^{\dagger}_{n,l,K'} = \left(\langle n,l|, -i\langle n-1,l|\right)/\sqrt{2}$ respectively where n and l are good quantum numbers of LL states in symmetric gauge, and the LL energies in conduction band as $E_n = \hbar\omega_0\sqrt{n}$ where $\omega_0 = \sqrt{2}v_F/l_0$. Each LL has degeneracy $N = 4S/(2\pi l_0^2)$ where S represents the surface of the graphene layer. Note that here we take the spin and valley isospin degeneracy into account. We further define the LL filling factor as $\nu = \rho S/N + 1/2$ where ρ is the electron doping density. In this paper, for the sake of simplicity, we consider the case of integer filling factor with the Fermi level being in the conduction band and zero temperature to avoid thermal effects.

In this work, we consider 1D optical cavity ($L_x \gg L_z \gg L_y$) with graphene monolayer placed in the middle at $z = L_z/2$ as depicted in Fig. 4-1, more information of this cavity can be found in case 2 of Appendix B. This permits us to treat the continuous dispersion along the x axis while keeping a few modes along z axis and neglecting all the modes along the y axis except the lowest one. The vector potential $\boldsymbol{A}_{em}(\boldsymbol{r})$ of cavity electromagnetic field can be written as

$$\boldsymbol{A}_{em}(\boldsymbol{r}) = \sum_{\boldsymbol{q}} \sqrt{\frac{\hbar}{2\varepsilon_0\varepsilon\omega_{\boldsymbol{q}}}}(u_{\boldsymbol{q}}a_{\boldsymbol{q}} + u^*_{\boldsymbol{q}}a^{\dagger}_{\boldsymbol{q}}) \tag{4-1}$$

where ε is the cavity dielectric constant and operators $a_{\boldsymbol{q}}$ are the photon annihilation operators with corresponding wave vector $\boldsymbol{q}$ written as $\boldsymbol{q} = (2\pi n_x/L_x, 0, \pi n_z/L_z)$, the mode spatial profile $u_{\boldsymbol{q}}$ reads

$$u_{\boldsymbol{q}} = \sqrt{\frac{2}{V}}\exp(i\frac{2\pi n_x x}{L_x})\sin(\frac{\pi n_z}{2})(0,1,0) \tag{4-2}$$

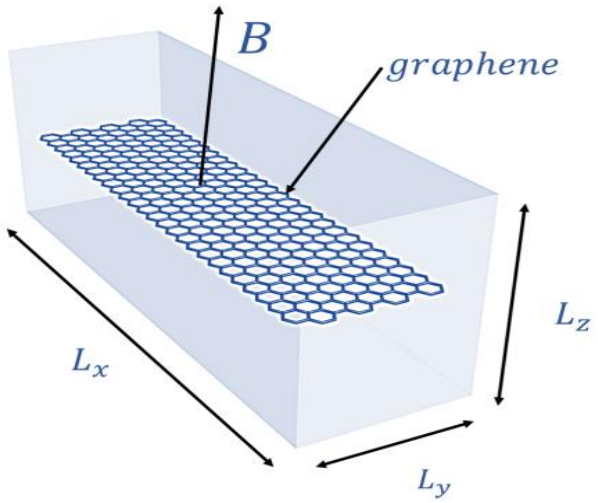

Fig. 4-1 Sketch of a one dimensional cavity embedding graphene sheet, a uniform and static magnetic field *B* is applied along the *z* axis. Cavity walls in y and z directions are perfectly conducting.

Note that only the photonic modes with n_z being the odd integers will be coupled to the LL transitions. The cavity modes frequency are given as

$$\omega_{\boldsymbol{q}} = \frac{c}{\sqrt{\varepsilon}}\sqrt{(\frac{\pi n_z}{L_z})^2 + (\frac{2\pi n_x}{L_x})^2} \tag{4-3}$$

The interaction Hamiltonian for the cavity-graphene system is given as $H_{\text{int}} = ev_F \boldsymbol{A}_{em} \bullet \boldsymbol{\sigma}$, project this Hamiltonian in LL basics of conduction band, we obtain

$$H_{\text{int}} = \sum_{n,l,n',l'} \frac{ev_F}{2}[\langle n,l|\boldsymbol{A}_{\boldsymbol{em}}|n'-1,l'\rangle + \langle n-1,l|\boldsymbol{A}_{\boldsymbol{em}}|n',l'\rangle]c^{\dagger}_{n,l}c_{n',l'} \tag{4-4}$$

where $\boldsymbol{A}_{\boldsymbol{em}}$ is given in Eq. (4-1). Bearing in mind that we are dealing with the cyclotron transitions between the last occupied LL $n = v-1$ with the first unoccupied one $n = v$, therefore the H_{int} can be simplified as

$$H_{\text{int}} = \sum_{l,l'} \frac{ev_F}{2}\langle v-1,l|\boldsymbol{A}_{\boldsymbol{em}}|v-1,l'\rangle(c^{\dagger}_{v,l}c_{v-1,l'} + c^{\dagger}_{v-1,l}c_{v,l'}) \tag{4-5}$$

Since we are dealing with low energy cavity modes, the LL mixing can be neglected [80] and again we need to apply the formula $\langle n,l|\exp(-i\boldsymbol{q}\cdot\boldsymbol{r})|n',l'\rangle = \exp(-|\boldsymbol{q}|^2 l_0^2/2)\chi_{n,n'}(ql_0)\chi_{l,l'}(-q^* l_0)$, we get

$$\frac{H_{\text{int}}}{\hbar} = \sum_{\boldsymbol{q},l} \frac{\Omega_{\boldsymbol{q}}}{\sqrt{N}} \sin(\frac{\pi n_3}{2})(a_{\boldsymbol{q}}^\dagger + a_{\boldsymbol{q}})(c_{v,l}^\dagger c_{v-1,l} + c_{v-1,l}^\dagger c_{v,l}) \tag{4-6}$$

We notice that only cavity modes with n_3 being odd number are coupled with LL transitions. At last, $\sin(\pi n_3/2)$ can be absorbed in photon creation and annihilation operators by transformation $\sin(\pi n_3/2)(a_{\boldsymbol{q}} + a_{\boldsymbol{q}}^\dagger) \to (a_{\boldsymbol{q}} + a_{\boldsymbol{q}}^\dagger)$ due to the fact that $\sin(\pi n_3/2) = \pm 1$, therefore, we obtain

$$\frac{H_{\text{int}}}{\hbar} = \sum_{\boldsymbol{q},l} \frac{\Omega_{\boldsymbol{q}}}{\sqrt{N}} (a_{\boldsymbol{q}}^\dagger + a_{\boldsymbol{q}})(c_{v,l}^\dagger c_{v-1,l} + c_{v-1,l}^\dagger c_{v,l}) \tag{4-7}$$

where the vacuum Rabi frequency is $\Omega_{\boldsymbol{q}} = \frac{ev_F}{2}\sqrt{\frac{N}{\varepsilon_0 \varepsilon \omega_{\boldsymbol{q}} V \hbar}}$ and $V = L_x L_y L_z$ is the cavity volume.

In order to bosonize the LL band excitations, we apply the Hosltein-Primakoff representation [21], where the effective Hamiltonian associated to the system reads

$$\frac{H}{\hbar} = \omega_{\text{eg}} b^\dagger b + \sum_{\boldsymbol{q}} \omega_{\boldsymbol{q}} a_{\boldsymbol{q}}^\dagger a_{\boldsymbol{q}} + \sum_{\boldsymbol{q}} \frac{\Omega_{\boldsymbol{q}}}{\sqrt{N}} (a_{\boldsymbol{q}}^\dagger + a_{\boldsymbol{q}})(b^\dagger \sqrt{N - b^\dagger b} + \sqrt{N - b^\dagger b}\, b) \tag{4-8}$$

where $\omega_{eg} \equiv \omega_0(\sqrt{v} - \sqrt{v-1})$ is the transition frequency between two nearby LLs. This is a multimode Dicke model which can be solved both in normal and superradiant phases [22]. Below the critical point (normal phase), the effective Hamiltonian in normal phase is obtained

$$\frac{H_{\text{No}}}{\hbar} = \omega_{\text{eg}} b^\dagger b + \sum_{\boldsymbol{q}} \omega_{\boldsymbol{q}} a_{\boldsymbol{q}}^\dagger a_{\boldsymbol{q}} + \sum_{\boldsymbol{q}} \Omega_{\boldsymbol{q}} (a_{\boldsymbol{q}}^\dagger + a_{\boldsymbol{q}})(b^\dagger + b) \tag{4-9}$$

Then the excitation spectrum of ω_j is given by solutions to the equation

$$4\omega_{eg} \sum_{\boldsymbol{q}} \frac{\omega_{\boldsymbol{q}} \Omega_{\boldsymbol{q}}^2}{\omega_{\boldsymbol{q}}^2 - \omega_j^2} = \omega_{eg}^2 - \omega_j^2 \tag{4-10}$$

We notice that the excitation energies ω_j are real only for $\eta \equiv \gamma_c / \gamma > 1$ where $\gamma \equiv \sum_q \Omega_q^2 / \omega_q$ and $\gamma_c \equiv \omega_{eg}/4$. The value of $\eta = 1$ separates the normal and superradiant phases. The summation of all the coupling photonic modes in γ shows that the critical Rabi frequency required for quantum phase transition can be reduced compared with single-mode cavity case by coupling matter to a multi-mode cavity.

Above the critical point ($\eta < 1$), we displace the Bosonic modes in Eq. (4-8) by $\tilde{a}_q = a_q \pm \sqrt{\alpha_q}$ and $\tilde{b} = b \mp \sqrt{\beta}$, and eliminate the terms in Eq. (4-8) that are linear in the Bosonic operators by choosing $\beta = \frac{N}{2}(1-\eta)$ and $\alpha_q = \frac{4\beta(N-\beta)\Omega_q^2}{N\omega_q^2}$. Note that we obtain exactly the same values of α_q and β regardless of which sign of the operator displacements we choose. The effective Hamiltonian above the phase transition point becomes

$$\frac{H_{\mathrm{SR}}}{\hbar} = \sum_q \omega_q \tilde{a}_q^\dagger \tilde{a}_q + \tilde{\omega}_{\mathrm{eg}} \tilde{b}^\dagger \tilde{b} + \sum_q \tilde{\Omega}_q (\tilde{a}_q^\dagger + \tilde{a}_q)(\tilde{b}^\dagger + \tilde{b}) + f(\tilde{b}^2 + \tilde{b}^{\dagger 2}) + const \qquad (4\text{-}11)$$

where $\tilde{\omega}_{\mathrm{eg}} = \frac{\omega_{eg}(-\eta^2 + 6\eta + 3)}{4\eta(\eta+1)}$, $\tilde{\Omega}_q = \Omega_q \eta \sqrt{\frac{2}{1+\eta}}$ and $f = \frac{\omega_{eg}(-3\eta^2 + 2\eta + 1)}{8\eta(\eta+1)}$.

Then the excitation spectrum $\tilde{\omega}_j$ above the critical point is given as

$$4(\tilde{\omega}_{eg} - 2f)\sum_q \frac{\omega_q \tilde{\Omega}_q^2}{\omega_q^2 - \tilde{\omega}_j^2} = \tilde{\omega}_{eg}^2 - 4f^2 - \tilde{\omega}_j^2 \qquad (4\text{-}12)$$

Note that beyond the transition point, the parity symmetry of the system has become spontaneously broken. In normal phase, the parity operator reads $\Pi_{\mathrm{No}} = \exp[i\pi(b^\dagger b + \sum_q a_q^\dagger a_q)]$ and it commutes with normal phase Hamiltonian $[\Pi_{\mathrm{No}}, H_{\mathrm{No}}] = 0$ satisfying parity symmetry. In superradiant phase, parity symmetry is broken $[\Pi_{\mathrm{No}}, H_{\mathrm{SR}}] = 0$, and system obeys a new parity symmetry $[\Pi_{\mathrm{SR}}, H_{\mathrm{SR}}] = 0$ where $\Pi_{\mathrm{SR}} = \exp[i\pi(\tilde{b}^\dagger \tilde{b} + \sum_q \tilde{a}_q^\dagger \tilde{a}_q)]$. Note that Eq. (4-10) and Eq. (4-12) give the complete spectrum of the magnetopolaritons in the system for both normal and

superradiant phases. In order to solve Eq. (4-12), we notice that the condition $L_x \gg L_z$ allows us to make replacement: $\sum_{\boldsymbol{q}} \to \sum_{n_z} \int g_{n_z}(\omega) d\omega$ where

$$g_{n_z}(\omega) = \frac{\omega \varepsilon L_x}{\pi c^2 \sqrt{\frac{\omega^2 \varepsilon}{c^2} - (\frac{n_z \pi}{L_z})^2}} \tag{4-13}$$

is the density of the modes, therefore Eq. (4-12) becomes

$$\frac{e^2 v_F^2 \omega_{eg} L_x N \eta}{2\pi c^2 \varepsilon_0 \hbar V} \sum_{n_z} \int_0^\infty \frac{dy}{y^2 + u_{n_z}} = \frac{\omega_{eg}^2 (-\eta^2 + 2\eta + 1)}{2\eta^2} - \tilde{\omega}_j^2 \tag{4-14}$$

where $u_{n_z} \equiv \frac{n_z^2 \pi^2}{L_z^2} - \frac{\varepsilon \tilde{\omega}_j^2}{c^2}$ and $y \equiv \sqrt{\frac{\omega^2 \varepsilon}{c^2} - (\frac{n_z \pi}{L_z})^2}$. In order to perform the integration in the left hand side of Eq. (4-14), we consider the situation $u_{n_z=1} > 0$, therefore we have $\int_0^\infty \frac{dy}{y^2 + u_{n_z}} = \frac{\pi}{2\sqrt{u_{n_z}}}$, thus the spectrum of magnetopolaritons can be obtained under condition $u_{n_z=1} > 0$ which is plotted in Fig. 4-2(a).

4.2 Numerical Results and Discussions

In Fig. 4-2(a) and Fig. 4-2(b), we show the complete spectrum of the magnetopolariton both in normal and superradiant phases as a function of doping density ρ and magnetic field strength B repectively. In Fig. 4-2(a), the superradiant phase transition occurs at $\rho_c = 2.42 \times 10^9 \text{cm}^{-2}$ and in Fig. 4-2(b), the superradiant phase transition occurs at $B = 8mT$ with our considered parameters. By analyzing the behavior of the excited state energy relatively to the ground state in the vicinity of the critical point, we find $\omega_j \sim |\rho - \rho_c|^{z\nu}$, here $z\nu = 1/2$ is the critical exponent. The first derivative of the excited state energy with respect to the doping density is $\frac{d\omega_j}{d\rho} \sim |\rho - \rho_c|^{-1/2}$ which diverges at the critical value, this marks the second order quantum phase transition. Meanwhile, we calculate the scaled ground state energy as $E_G / (N\omega_c) = -(1-\eta)^2 \hbar \omega_{eg} / (4\eta \omega_c)$ shown in Fig. 4-2(c) and Fig. 4-2(d) where we

scale this quantity by N followed by normalization with respect to the lowest lying cavity mode frequency $\omega_c \equiv c\pi/(L_z\sqrt{\varepsilon})$. As we can see in Fig. 4-2(c) and Fig. 4-2(d), the system indeed shows a qualitative change of the ground state energy at the phase transition point beyond which the system tends to stabilize itself into the superradiant phase.

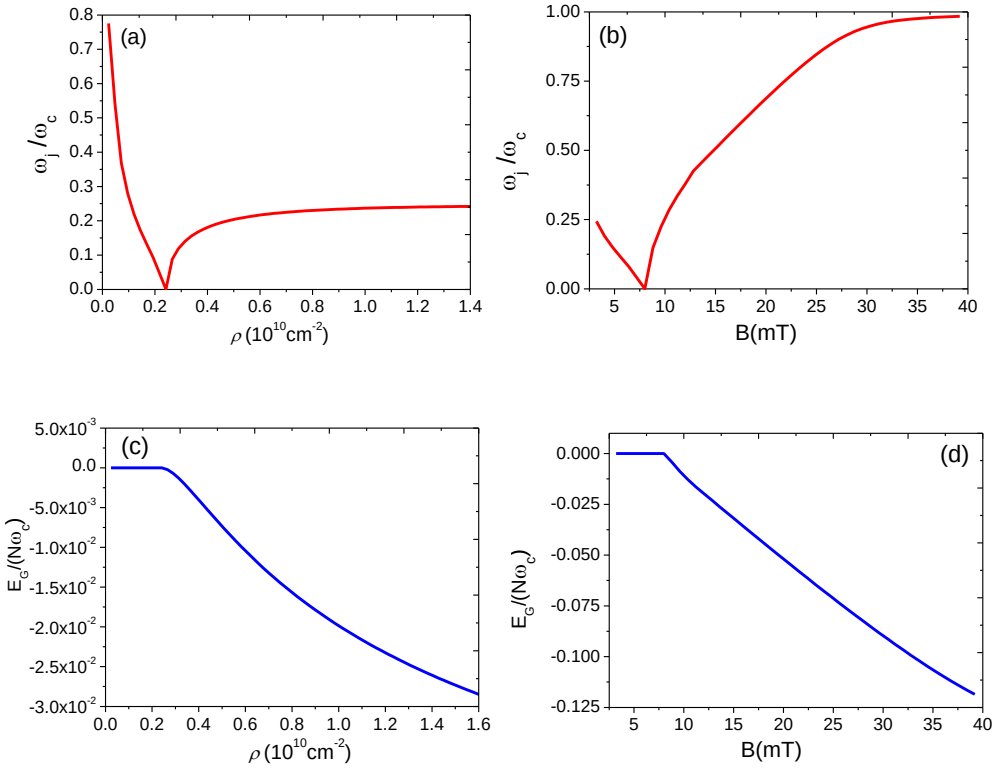

Fig. 4-2 (a) Normalized frequencies of magnetopolariton both in normal and superradiant phases as a function of doping density ρ with $B = 8mT$ and the critical density for phase transition is ρ=2.42×10^{9}cm^{-2}. (b) Normalized frequencies of magnetopolariton both in normal and superradiant phases as a function of magnetic field B with doping density ρ=2.40×10^{9}cm^{-2} and the critical value of magnetic field for phase transition is $B = 8mT$ (c) The scaled ground state energy both in normal and superradiant phases as a function of doping density ρ with $B = 8mT$. (d) The scaled ground state energy both in normal and superradiant phases as a function of magnetic field B with doping density ρ=2.40×10^{9}cm^{-2}. The rest parameters are $L_z = 100\mu m$, $L_x = 25L_z$, $L_y = L_z/5$ and $\omega_c = 4.7\text{THz rad}^{-1}$ being the lowest lying cavity mode frequency. With these parameters, only one branch of magnetopolaritons shows up (as shown in Fig. 4-2 (a), (b)) and this result is obtained with a cutoff value of $n_z < 7$.

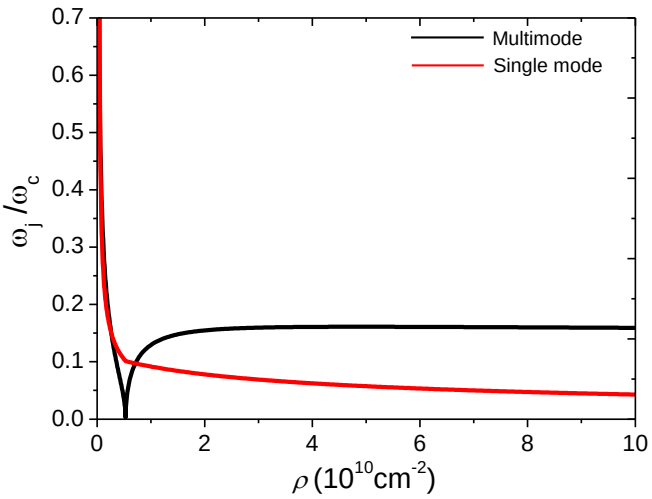

Fig. 4-3 Normalized frequencies of magnetopolariton for multimode versus single-mode as a function of doping density ρ. Parameters for multimode case are $B=8mT$, $L_z=100\mu m$, $L_x=25L_z$, $L_y=L_z/5$ and $\omega_c=4.7\mathrm{THz\,rad}^{-1}$ is the lowest lying cavity mode frequency. For the single mode case, the photonic mode frequency $\omega=\omega_c=4.7\mathrm{THz\,rad}^{-1}$. The critical density for phase transition in the multimode case is $\rho_c=5.32\times10^{9}\mathrm{cm}^{-2}$, this result is obtained with $n_z=1$. Note that the critical density for the single mode phase transition is $\rho_c=4.38\times10^{11}\mathrm{cm}^{-2}$ which is around 100 times larger than the critical density in multi-mode case.

Fig. 4-3 shows the magnetopolariton frequencies calculated from the cases of multiple cavity modes coupling and single mode coupling as function of doping density. The result shows that the critical doping density required for superradiant phase transition is much smaller in multiple modes coupling than that in single mode coupling. This implies that we should consider a multimode cavity to experimentally observe the superradiant phase transition. Since we here consider the Landau transition of graphene under strong magnetic field, we think no graphene plasmonic mode will be excited in this THz range. As well, we have considered the collective excitation of graphene by considering the many-body interactions, the collective excitation of Plasmon is included in our model.

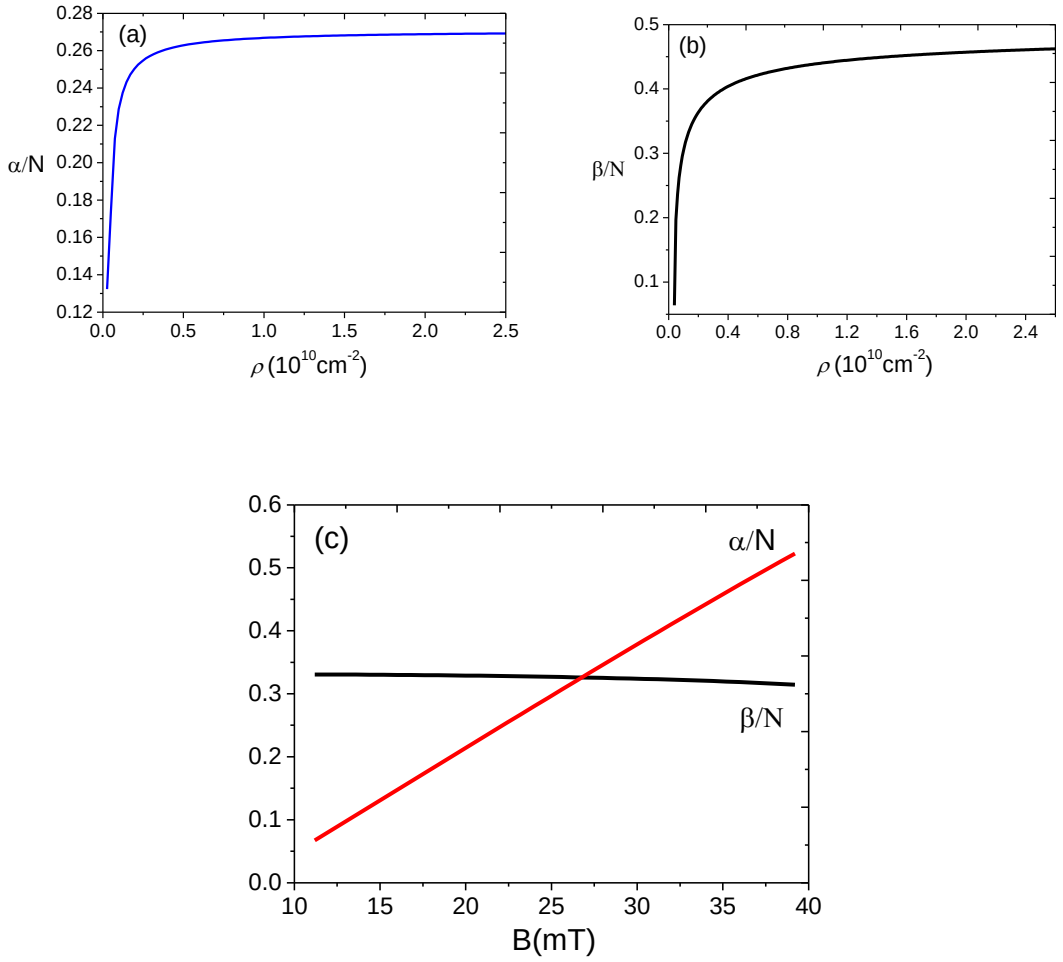

Fig. 4-4 (a) The scaled mean photon number as a function of doping density ρ with magnetic field $B = 8mT$. (b) electronic inversion as a function of doping density ρ with magnetic field $B = 8mT$. (c) The scaled mean photon number and the electronic inversion as a function of the magnetic field B with doping density ρ=2.40×10^{9}cm^{-2} . The rest parameters are $L_z = 200\mu m$, $L_x = 50L_z$ and $L_y = L_z / 5$.

In Fig. 4-4, we plot scaled mean photon number $\alpha = \sum_{\boldsymbol{q}} \langle a_{\boldsymbol{q}}^{\dagger} a_{\boldsymbol{q}} \rangle$ and electronic inversion $\langle b^{\dagger} b \rangle = \beta$. This figure clearly illustrates that, in the normal phase, the system is only microscopically excited, whereas above a certain critical doping density both the field and electronic ensemble acquire macroscopic excitations. In the Fig. 4-4(c), since the degenercy $N = 4S / (2\pi l_0^2)$ has a linear dependence of the magnetic field B, therefore, we get the nearly linear dependence of the scaled quantities α and β . Noted that photons in the ground state of superradiant regime

are virtual and they cannot be escaped from the cavity in the case of time-independent Hamiltonians [8]. So multimode coupling of cavity photon and cyclotron transition can dramatically enhance the superradiant emission if we fast modulate the Hamiltonian compared with single mode case.

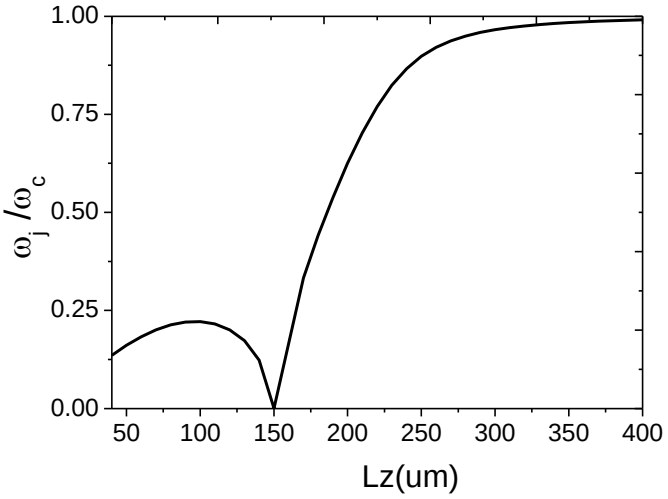

Fig. 4-5 Normalized frequencies of magnetopolariton both in normal and superradiant phases as a function of cavity dimension L_z with $B = 8mT$ and the doping density is $\rho_c = 1.06\times10^{9}\text{cm}^{-2}$. The critical value of cavity dimensional for phase transition is $L_z = 150\mu m$. The other parameters are $L_x = 25L_z$, $L_y = L_z / 5$.

In Fig. 4-5, we plot the normalized magnetopolariton frequency versus the cavity thickness L_z. $\omega_c \equiv c\pi / (L_z\sqrt{\varepsilon})$ is the lowest cavity mode frequency which also depends on the cavity thickness L_z, as we can see, the frequency of this lowest mode increases as the cavity size decreases. Note that for large cavities, the frequencies of the cavity modes become continuous, in such scenario, we cannot discard some higher order modes frequencies when we calculate the magnetopolariton frequencies. Therefore, the results become inaccurate for larger cavities. The Fig. 4-5 is plotted with a cutoff range with $L_z < 400\mu m$.

As a conclusion of chapter 4, we theoretically present the excitation spectrum of graphene embedded in an optical cavity under perpendicular magnetic field. We consider the coupling of cyclotron transition and a multimode cavity described by a

multimode Dicke model. The model predicts a superradiant phase transition will occur in graphene while such quantum phase transition does not exist in conventional semiconductors. The complete excitation spectrum in both the normal phase and superradiant phase regimes is given. In contrast to the single mode case, multimode coupling of cavity photon and cyclotron transition can greatly reduce the critical vacuum Rabi frequency required for quantum phase transition, and dramatically enhance the superradiant emission by fast modulating the Hamiltonian.

5. THEORETICAL STUDY OF AHARONOV-BOHM EFFECT FROM QUANTUM FIELD THEORY APPROACH

In this chapter, we open a new research topic on the aharonov-bohm effect which is a diversion from the previous chapters; this topic is motivated by the author's own interest in foundations of physics. For a problem with one charged quantum particle P moving in an electromagnetic vector potential $\hat{A}_\mu = (\hat{\phi}, -\hat{\boldsymbol{A}})$ created by some other charged particles, the evolution of particle P can be described by the one particle quantum mechanics (OPQM), however, we can also treat this as a multi-particles problem in the framework of quantum field theory by providing a full quantization of the source that producing the classical vector potential $\hat{A}_\mu = (\hat{\phi}, -\hat{\boldsymbol{A}})$. These two methods need to be equavalent, i.e., they produce the same result for the evolution of P. One open question is how to describe the evolution of P within the framework of quantum field theory and show that these two methods yield the same result? In this section, first we start with the discussions on the classical electromagnetic theory then review the Aharonov-Bohm (AB) effect within the one particle quantum mechanics (OPQM) framework. After that, we study the AB effect within the quantum field theoy framework. We provide a quantum treatment of the source of the electromagnetic potential and argue that the underlying mechanism in AB effect can be viewed as interactions between electrons described by QED theory where the interactions are mediated by virtual photons. On further analysis, we show that the framework of one particle quantum mechanics (OPQM) can be given, in general, as a mathematically approximated model which is reformulated from QED theory while the AB effect scheme provides a platform for our derivations. In addition, the classical Maxwell equations are derived from QED scattering process while both classical electromagnetic fields and potentials serve as mathematical tools that are constructed to approximate the interactions among elementary particles described by QED physics. Conclusions are given at the last of this chapter.

5.1 Review of AB Effect From One Particle Quantum Mechanics

Aharonov-Bohm effect has attracted tremendous research interest due to the conceptually importance it bears since its discovery [81], [82]. It is a fundamental

phenomenon of quantum interference influenced by a closed loop pierced by a magnetic flux, this effect was experimentally observed in metal rings in 1985 [83] and later in carbon nanotubes [84]. Besides its fundamental significance for quantum theory, it's importance for applications in mesoscopic interferometric devices is omnipresent [85]–[89].

For the AB effect, as is shown in Fig. 5-1, the magnetic field vanishes whereas the charged particle travel, however, this charged particle still feels an effect acted by the electromagnetic potential. Since the electromagnetic potential is not gauge-invariant and it cannot represent a physical entity, it is generally believed that the motion of a charged particle can be influenced by the electromagnetic fields confined to regions from which the particle is rigorously excluded; this attracts some researches and debates on the nonlocal feature in the quantum theory [90]–[99]. In the following sections, we are not going to join these discussions over the nonlocal feature of OPQM; instead we show that an alternative interpretation underlying the mechanism can be revealed provided a full quantum treatment of the source of the electromagnetic potential is undertaken within the framework of QED. Throughout this chapter, we use natural units in which the light velocity as well as Planck constant is equal to unity.

Before we present the AB effect, let us first take a look at classical electrodynamics theory. In classical theory, the Hamiltonian of a charged particle in presence of classical potential $A_\mu(t,\boldsymbol{x})$ can be given as

$$H = \frac{1}{2m}[\,\boldsymbol{p} - q\boldsymbol{A}(t,\boldsymbol{x})]^2 + q\phi(t,\boldsymbol{x}) \tag{5-1}$$

This gives the Lorentz equation of motion as

$$m\frac{d^2\boldsymbol{x}}{d^2t} = q[-\vec{\nabla}\phi - \frac{\partial \boldsymbol{A}}{\partial t} + \vec{\nabla}(\boldsymbol{v}\cdot\boldsymbol{A}) - (\boldsymbol{v}\cdot\vec{\nabla})\boldsymbol{A}] \tag{5-2}$$

The electromagnetic field (EMF) can be introduced as

$$\begin{aligned} \boldsymbol{B}(t,\boldsymbol{x}) &\equiv \vec{\nabla}\times\boldsymbol{A}(t,\boldsymbol{x}) \\ \boldsymbol{E}(t,\boldsymbol{x}) &\equiv -\vec{\nabla}\phi(t,\boldsymbol{x}) - \frac{\partial \boldsymbol{A}(t,\boldsymbol{x})}{\partial t} \end{aligned} \tag{5-3}$$

Therefore, Eq. (5-2) can be written in a more elegant form as

$$m\frac{d^2\boldsymbol{x}}{d^2t} = q\boldsymbol{E}(t,\boldsymbol{x}) + q\boldsymbol{v}\times\boldsymbol{B}(t,\boldsymbol{x}) \tag{5-4}$$

For the OPQM theory, we replace $\boldsymbol{p}$ with $-i\vec{\nabla}$ in Eq. (5-1) and obtain the Hamiltonian of an electron in non-relativistic limit as

$$H = \frac{1}{2m}[-i\vec{\nabla} + e\boldsymbol{A}(t,\boldsymbol{x})]^2 - e\phi(t,\boldsymbol{x}) \tag{5-5}$$

For the AB effect depicted in Fig. 5-1, in case of non-time-varying potential $\boldsymbol{A}(\boldsymbol{x})$ in radiation gauge, before the magnetic field is turned on in the solenoid, the electron P with wave-vector $\boldsymbol{k}$ travelling along two different paths is in a super-positioned state as

$$\psi_{\boldsymbol{k}}(\boldsymbol{x}) = \exp(i\boldsymbol{k}\cdot\boldsymbol{x}_1) + \exp(i\boldsymbol{k}\cdot\boldsymbol{x}_2) \tag{5-6}$$

In which $\boldsymbol{x}_1$ and $\boldsymbol{x}_2$ denote two separable paths as shown in the figure, the phase difference between the two plane waves is $\Delta\theta = \boldsymbol{k}\cdot(\boldsymbol{x}_1 - \boldsymbol{x}_2)$. After turning on the magnetic field, one can verify that the state of the electron P becomes

$$\psi'(\boldsymbol{x}) = \exp[i(\boldsymbol{k}\cdot\boldsymbol{x}_1 - \int_0^{\boldsymbol{x}_1} e\boldsymbol{A}(\boldsymbol{x}')\cdot d\boldsymbol{x}')] + \exp[i(\boldsymbol{k}\cdot\boldsymbol{x}_2 - \int_0^{\boldsymbol{x}_2} e\boldsymbol{A}(\boldsymbol{x}')\cdot d\boldsymbol{x}')] \tag{5-7}$$

And the phase difference will acquire a shifted value as

$$\Delta\theta' = \oint e\boldsymbol{A}(\boldsymbol{x}')\cdot d\boldsymbol{x}' = \iint e\boldsymbol{B}\cdot d\boldsymbol{S} = e\Phi_m \tag{5-8}$$

in which the first integral is the circle enclosing the solenoid. Therefore, the electron traveling enclosing a circle will pick up a phase shift that can be measured which is $e\Phi_m$ where Φ_m is the total magnetic flux through the closed surface.

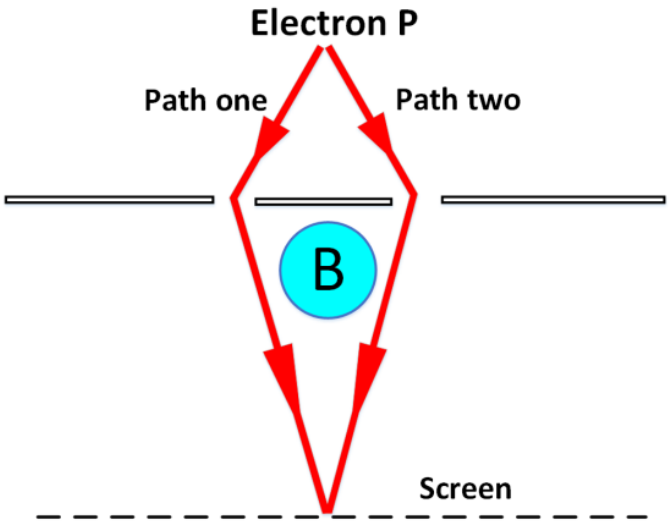

Fig. 5-1. Sketch of a double-slit experiment in which the Aharonov-Bohm effect can be observed.

5.2 Study of AB Effect Based on Quantum Field Theory

In this section, we are going to derive the classical four-potential from QED scattering physics while the AB effect scheme provides a platform for our discussions. The Hamiltonian of QED theory without free electroic magnetic field (FEMF) is

$$\hat{H} = \int d^3\boldsymbol{x}[\hat{\bar{\psi}}(-i\boldsymbol{\gamma}\cdot\vec{\nabla} - e\gamma^{\mu}\hat{A}_{\mu} + m_e)\hat{\psi}] \tag{5-9}$$

in which $\hat{\bar{\psi}} \equiv \hat{\psi}^{\dagger}\gamma^0$, $\hat{A}_{\mu} = (\hat{\phi}, -\hat{\boldsymbol{A}})$ is the quantum electromagnetic four-potential, e is the coupling coefficient which is a positive constant, m_e is electron's rest energy and γ^{μ} are four Dirac Gamma matrices. In radiation gauge, the electromagnetic vector potential and Dirac electron field with fixed spin in the interaction picture are

$$\hat{\boldsymbol{A}}_I(\boldsymbol{x},t) = \int \frac{d^3\boldsymbol{k}}{(2\pi)^3}\frac{1}{\sqrt{2\omega_{\boldsymbol{k}}}}\sum_{\lambda=1,2}[\hat{a}_{\boldsymbol{k}}^{\lambda}\boldsymbol{\nu}^{\lambda}e^{-i(\omega_{\boldsymbol{k}}t-\boldsymbol{k}\cdot\boldsymbol{x})} + \hat{a}_{\boldsymbol{k}}^{\lambda\dagger}\boldsymbol{\nu}^{\lambda}e^{i(\omega_{\boldsymbol{k}}t-\boldsymbol{k}\cdot\boldsymbol{x})}] \tag{5-10}$$

$$\hat{\psi}_I(\boldsymbol{x},t) = \int \frac{d^3\boldsymbol{k}}{(2\pi)^3}\frac{1}{\sqrt{2\omega_{\boldsymbol{k}}}}\hat{c}_{\boldsymbol{k}}u_{\boldsymbol{k}}e^{-i(\omega_{\boldsymbol{k}}t-\boldsymbol{k}\cdot\boldsymbol{x})} \tag{5-11}$$

where $\hat{a}_{\boldsymbol{k}}^{\lambda}$ and $\hat{c}_{\boldsymbol{k}}$ are photon and electron annihilation operators that satisfy commutation relation $[\hat{a}_{\boldsymbol{k}}^{\lambda}, \hat{a}_{\boldsymbol{k}'}^{\lambda'\dagger}] = (2\pi)^3\delta^{\lambda\lambda'}\delta^3(\boldsymbol{k}-\boldsymbol{k}')$ and anti-commutation relation

$\{\hat{c}_{\boldsymbol{k}}, \hat{c}^{\dagger}_{\boldsymbol{k}'}\} = (2\pi)^3 \delta^3(\boldsymbol{k} - \boldsymbol{k}')$ respectively, the rest symbols are $u_{\boldsymbol{k}} = \begin{pmatrix} \xi\sqrt{\omega_{\boldsymbol{k}} - \boldsymbol{k}\cdot\boldsymbol{\sigma}} \\ \xi\sqrt{\omega_{\boldsymbol{k}} + \boldsymbol{k}\cdot\boldsymbol{\sigma}} \end{pmatrix}$ where we take the positive root of each eigenvalue when taking the square root of the matrix in $u_{\boldsymbol{k}}$ and $\xi = \begin{pmatrix} 1 \\ 0 \end{pmatrix}$, $\boldsymbol{\sigma}$ are Pauli matrices; $\boldsymbol{\nu}^{\lambda=1} = \frac{1}{\sqrt{k_1^2 + k_2^2}}(k_2, -k_1, 0)$ and $\boldsymbol{\nu}^{\lambda=2} = \frac{1}{\sqrt{(k_1^2 + k_2^2)|\boldsymbol{k}|^2}}(k_1 k_3, k_2 k_3, -k_1^2 - k_2^2)$ are two polarization directions of photons. Note that we omitted the positrons part in Eq. (5-11) just for simplicity of presentation. The free and interaction Hamiltonians are $\hat{H}_0 = \int d^3\boldsymbol{x}[\hat{\bar{\psi}}(-i\boldsymbol{\gamma}\cdot\vec{\nabla} + m_e)\hat{\psi}]$ and $\hat{H}_{\text{int}} = \int d^3\boldsymbol{x}(-e\hat{\bar{\psi}}\gamma^{\mu}\hat{A}_{\mu}\hat{\psi})$ respectively. In the interaction picture, the time evolution operator $\hat{U}(t, t_0)$ obey equation $i\frac{\partial}{\partial t}\hat{U}(t, t_0) = \hat{H}_I(t)\hat{U}(t, t_0)$ with $\hat{H}_I(t) = e^{i\hat{H}_0(t-t_0)}\hat{H}_{\text{int}}e^{-i\hat{H}_0(t-t_0)}$, the time-dependent perturbation theory to second order gives

$$\hat{U}(t, t_0) = 1 + (-i)\int_{t_0}^{t} dt_1 \hat{H}_I(t_1) + (-i)^2 \int_{t_0}^{t} dt_1 \int_{t_0}^{t_1} dt_2 \hat{H}_I(t_1)\hat{H}_I(t_2) \tag{5-12}$$

Before we give the QED description of the AB effect, let us take a look at the scattering of two electrons governed by QED theory. The leading order which is the second order of perturbations gives

$$\langle \boldsymbol{k}', \boldsymbol{p}' | T[\frac{(-i)^2}{2}\int_{-\infty}^{\infty} dt_1 \int_{-\infty}^{\infty} dt_2 \hat{H}_I(t_1)\hat{H}_I(t_2)] | \boldsymbol{p}, \boldsymbol{k} \rangle = (2\pi)^4 \delta^4(\tilde{p} + \tilde{k} - \tilde{p}' - \tilde{k}')\sum \tag{5-13}$$

in which the symbol T represents the time-ordering operator, we have the scattering matrix element $\sum = \frac{ie^2}{(\omega_{\boldsymbol{p}} - \omega_{\boldsymbol{p}'})^2 - |\boldsymbol{p} - \boldsymbol{p}'|^2}\bar{u}_{\boldsymbol{p}'}\gamma^{\mu}u_{\boldsymbol{p}}\eta_{\mu\nu}\bar{u}_{\boldsymbol{k}'}\gamma^{\nu}u_{\boldsymbol{k}}$ where $\eta_{\mu\nu}$ is the Minkowski metric tensor with $\eta_{00} = -\eta_{ii} = 1\,(i = 1, 2, 3)$ and energy-momentum four-vector $\tilde{p} \equiv (\omega_{\boldsymbol{p}}, \boldsymbol{p})$ with $\omega_{\boldsymbol{p}}^2 = m_e^2 + \boldsymbol{p}^2$ for on-shell electrons. The incoming and outgoing states are $|\boldsymbol{p}, \boldsymbol{k}\rangle = 2\sqrt{\omega_{\boldsymbol{p}}\omega_{\boldsymbol{k}}}c_{\boldsymbol{p}}^{\dagger}c_{\boldsymbol{k}}^{\dagger}|0\rangle$ and $\langle \boldsymbol{k}', \boldsymbol{p}'| = \langle 0|2\sqrt{\omega_{\boldsymbol{p}'}\omega_{\boldsymbol{k}'}}c_{\boldsymbol{k}'}c_{\boldsymbol{p}'}$ which

describe two electrons with the same spin and different momentum as $\boldsymbol{p}(\boldsymbol{p}')$ and $\boldsymbol{k}(\boldsymbol{k}')$ respectively. We can divide Σ separately into two parts as

$$\Sigma = \frac{ie^2}{(\omega_{\boldsymbol{p}} - \omega_{\boldsymbol{p}'})^2 - |\boldsymbol{p} - \boldsymbol{p}'|^2} (\bar{u}_{\boldsymbol{p}'} \gamma^0 u_{\boldsymbol{p}} \bar{u}_{\boldsymbol{k}'} \gamma^0 u_{\boldsymbol{k}} - \bar{u}_{\boldsymbol{p}'} \gamma^i u_{\boldsymbol{p}} \bar{u}_{\boldsymbol{k}'} \gamma^i u_{\boldsymbol{k}}) \tag{5-14}$$

In the non-relativistic limit, $\omega_{\boldsymbol{p}} - \omega_{\boldsymbol{p}'} \approx 0$ and the second term $\bar{u}_{\boldsymbol{k}'} \gamma^i u_{\boldsymbol{k}} \approx 0$, the first term gives $\Sigma = -i4m_e^2 \frac{e^2}{|\boldsymbol{p} - \boldsymbol{p}'|^2}$ which is a matrix element of Coulomb potential expanded in momentum basis with some constant factors, i.e., $\langle \boldsymbol{p}' | \frac{1}{|\hat{\boldsymbol{x}}|} | \boldsymbol{p} \rangle \propto \frac{1}{|\boldsymbol{p} - \boldsymbol{p}'|^2}$ with Fourier expansion formula $\frac{1}{4\pi |\boldsymbol{x}|} = \int \frac{d^3 \boldsymbol{p}}{(2\pi)^3} \frac{\exp(i\boldsymbol{p} \cdot \boldsymbol{x})}{|\boldsymbol{p}|^2}$; therefore, the Coulomb potential arises from two electrons scattering process described by QED theory. Note that in Eq. (5-13), we exclude the exchange interaction, that is, the transition from $\boldsymbol{p} \to \boldsymbol{k}'$ and $\boldsymbol{k} \to \boldsymbol{p}'$, later on we will explain that this transition is not allowed due to the constraint that we impose on the system which is that the two electrons can be distinguished, i.e., each of them are confined in a separable region and such constraint is indeed satisfied in the AB effect. Meanwhile the static EMF can be given as $\boldsymbol{E}(\boldsymbol{x}) = -\vec{\nabla} \frac{e}{4\pi |\boldsymbol{x}|}$, and this EMF together with Coulomb potential are nothing but mathematical idealisations that approximate, to the second order perturbations, the interaction which is mediated by virtual photons propagating between the two electrons.

Now let us analyse what is happening for the AB effect using QED theory. In the schematic of double-slit experiment in which the AB effect can be observed as depicted in Fig. 5-1, the EMF is confined in the cylindrical solenoid. Suppose that this EMF is originally from spin and motion effects of an ensemble of electrons which are confined in the solenoid; this enormous number of electrons, in principle, can be mathematically constructed as a quantum state $|\Psi\rangle$, and we denote the state of an electron with momentum $\boldsymbol{p}$ traveling outside of the solenoid as $|\boldsymbol{p}\rangle \equiv \sqrt{2\omega_{\boldsymbol{p}}} c_{\boldsymbol{p}}^\dagger |0\rangle$ in

which $|0\rangle$ is the vacuum state, we will name this traveling electron as P in all subsequent discussions. Note that for AB effect, we have the condition that the quantum state $|\Psi\rangle$ is confined in the solenoid and the electron P does not penetrate into the solenoid; this is the separable constraint that we mentioned below Eq. (5-14), that is, the electron P is distinguishable from each electron in system $|\Psi\rangle$. It is clear that constructing an exact mathematical expression of $|\Psi\rangle$ which involves a macroscopic ensemble of electrons in real world would be a highly non-trivial task, however, our target here is to provide a qualitative analysis of what happens for P using QED theory.

As stated above, we express the whole system which includes P and the ensemble of electrons as a quantum state $|\Psi, \boldsymbol{p}\rangle$, we further assume that the interaction energy between P and $|\Psi\rangle$ is much smaller than the free energy of P (this is due to the macroscopic distance between P and $|\Psi\rangle$), then the evolution of P can be known, theoretically, using perturbation theory. We further assume that the combined system $|\Psi, \boldsymbol{p}\rangle$ is kept in an isolated situation and the ensemble of the electrons is in a macroscopically equilibrium state; therefore we expect that the state $|\Psi\rangle$ does not vary macroscopically throughout the whole experimental time. Such physical idealization is a good approximation provided that there are no dramatic disturbances caused by the environment as well as significant external forces acted on $|\Psi, \boldsymbol{p}\rangle$ from other systems, later on we will see that this approximation can lead us to derive a non-time-varying classical potential $A_\mu(\boldsymbol{x})$. Therefore, we can obtain the evolution of system $|\Psi, \boldsymbol{p}\rangle$ up to second order of perturbations as

$$\langle \boldsymbol{p}', \Psi' | \hat{U}(t, t_0) | \Psi, \boldsymbol{p} \rangle = \langle \boldsymbol{p}', \Psi' | \Psi, \boldsymbol{p} \rangle + (-i)\int_{t_0}^{t} dt_1 \langle \boldsymbol{p}', \Psi' | \hat{H}_I(t_1) | \Psi, \boldsymbol{p} \rangle + (-i)^2 \int_{t_0}^{t} dt_1 \int_{t_0}^{t_1} dt_2 \langle \boldsymbol{p}', \Psi' | \hat{H}_I(t_1) \hat{H}_I(t_2) | \Psi, \boldsymbol{p} \rangle \tag{5-15}$$

Since we do not include the photon field into the system, the first order perturbation term $\langle \boldsymbol{p}', \Psi' | \hat{H}_I(t_1) | \Psi, \boldsymbol{p} \rangle = 0$. In the second order expression we have

$$\langle \boldsymbol{p}', \Psi' | \hat{H}_I(t_1)\hat{H}_I(t_2) | \Psi, \boldsymbol{p} \rangle =$$
$$\langle \boldsymbol{p}', \Psi' | \int d^3\boldsymbol{x} d^3\boldsymbol{y} [e^2 \hat{\bar{\psi}}_I(\boldsymbol{x}, t_1)\gamma_\mu \hat{A}_I^\mu(\boldsymbol{x}, t_1)\hat{\psi}_I(\boldsymbol{x}, t_1)\hat{\bar{\psi}}_I(\boldsymbol{y}, t_2)\gamma_\nu \hat{A}_I^\nu(\boldsymbol{y}, t_2)\hat{\psi}_I(\boldsymbol{y}, t_2)] | \Psi, \boldsymbol{p} \rangle$$

(5-16)

There are many terms arising from Eq. (5-16), most of them are originally from interactions between electrons inside of $|\Psi\rangle$ while leaving P as unaffected, that is,

$$\langle \Psi' | \int d^3\boldsymbol{x} d^3\boldsymbol{y} [e^2 \hat{\bar{\psi}}_I(\boldsymbol{x}, t_1)\gamma_\mu \hat{A}_I^\mu(\boldsymbol{x}, t_1)\hat{\psi}_I(\boldsymbol{x}, t_1)\hat{\bar{\psi}}_I(\boldsymbol{y}, t_2)\gamma_\nu \hat{A}_I^\nu(\boldsymbol{y}, t_2)\hat{\psi}_I(\boldsymbol{y}, t_2)] | \Psi \rangle \langle \boldsymbol{p}' | \boldsymbol{p} \rangle$$

(5-17)

which do not contribute to the evolution of P. Thus, in all subsequent discussions, the results obtained from Eq. (5-16) only include the interactions between $|\Psi\rangle$ and P. Note that solving Eq. (5-16) would be highly non-trivial, however, we can compare this expression with Eq. (5-13) and see that the underlying mechanism would not be different with the scattering between two electrons described by QED theory, the interaction between states $|\Psi\rangle$ and $|\boldsymbol{p}\rangle$ is mediated by the virtual photons propagating between them.

Next we are going to show how the classical four-potential arise from the framework of QED. We note that in the interaction picture, the field operators of Eq. (5-10) and Eq. (5-11) display a rotating-time-dependence through the mathematical expression $e^{i\omega t}$, for the macroscopically stationary system $|\Psi\rangle$, this rotating-time-dependence would allow us to make an approximation as $\hat{U}(t+\mathrm{T}, t_0)|\Psi, \boldsymbol{p}\rangle = \hat{U}(t, t_0)|\Psi, \boldsymbol{p}\rangle$ in which $\mathrm{T} \gg 2\pi/\omega$ which means that the effects on P caused by the variations of any electrons' state inside of $|\Psi\rangle$ would be cancelled away in a long term by other variations within the state $|\Psi\rangle$ itself; this is the mean field approximation. Therefore we can remove this rotating-time-dependence by integrating over an infinite time period; this integration would usually generate an overall energy conservation constraint given by a Dirac delta function as displayed in Eq. (5-13). Thus, For the second order term in Eq. (5-15), we replace the state $\langle \boldsymbol{p}', \Psi' |$ with $\langle \boldsymbol{p}', \Psi |$ which is the tensor product of a free state of P with momentum $\boldsymbol{p}'$ and the initial state $|\Psi\rangle$, i.e., $\langle \boldsymbol{p}', \Psi | \equiv \langle 0 | \sqrt{2\omega_{\boldsymbol{p}'}} c_{\boldsymbol{p}'} \otimes \langle \Psi |$, we obtain the result as

$$S_2^{QED}(\boldsymbol{p}', \boldsymbol{p}) \equiv T[\frac{(-i)^2}{2}\int_{-\infty}^{\infty} dt_1 \int_{-\infty}^{\infty} dt_2 \left\langle \boldsymbol{p}', \Psi \middle| \hat{H}_I(t_1)\hat{H}_I(t_2) \middle| \Psi, \boldsymbol{p} \right\rangle] \tag{5-18}$$

in which $S_2^{QED}(\boldsymbol{p}', \boldsymbol{p})$ is a function of the initial and final momentum of the electron P and note that $S_2^{QED}(\boldsymbol{p}', \boldsymbol{p})$ does not cover the internal interactions expressed by Eq. (5-17). By tracing out $|\Psi\rangle$, the mathematical structure of function $S_2^{QED}(\boldsymbol{p}', \boldsymbol{p})$ depends on the configurations of the ensemble of electrons which can be seen as a generating source. Note that it is legitimate to perform the time integration over an infinite period provided that the state $|\Psi\rangle$ is macroscopically stationary, the methods above will not be valid in cases of a time-varying state $|\Psi(t)\rangle$ driven by some other external forces generated by a third party system interacting with $|\Psi\rangle$. Furthermore, we obtain the matrix elements of evolution operator expanded in momentum basis up to the second order as

$$S_0^{QED}(\boldsymbol{p}', \boldsymbol{p}) + S_2^{QED}(\boldsymbol{p}', \boldsymbol{p}) = \left\langle \boldsymbol{p}', \Psi \middle| \hat{U}(\infty, -\infty) \middle| \Psi, \boldsymbol{p} \right\rangle \tag{5-19}$$

in which $S_0^{QED}(\boldsymbol{p}', \boldsymbol{p}) \equiv \left\langle \boldsymbol{p}', \Psi \middle| \Psi, \boldsymbol{p} \right\rangle$ and $\hat{U}(\infty, -\infty)$ is just Eq. (5-12) with $t = \infty$ and $t_0 = -\infty$, next we are going to show how the classical potentials arise from $S_2^{QED}(\boldsymbol{p}', \boldsymbol{p})$.

For AB effect described within OPQM framework, the system now in consideration is the electron P, in case of a static four-potential $A_\mu(\boldsymbol{x})$, the OPQM Hamiltonian can be given as

$$H = \gamma^0[-i\boldsymbol{\gamma}\cdot\vec{\nabla} - e\gamma^\mu A_\mu(\boldsymbol{x}) + m_e] \tag{5-20}$$

in which the interaction energy is $H_{\text{int}}(\boldsymbol{x}) = -e\gamma^0\gamma^\mu A_\mu(\boldsymbol{x})$ with $A_\mu(\boldsymbol{x}) = [\phi(\boldsymbol{x}), -\boldsymbol{A}(\boldsymbol{x})]$ and free energy is $H_0 = \gamma^0(-i\boldsymbol{\gamma}\cdot\vec{\nabla} + m_e)$. By comparison, we note that the photon field operator $\hat{A}_\mu$ in Eq. (5-9) has been replaced by a function $A_\mu(\boldsymbol{x})$ in Eq. (5-20); next we are going to explain how the function $A_\mu(\boldsymbol{x})$ arises from QED theory. In the interaction picture of OPQM, we have the interaction energy and evolution operator as

$$H_I(t) = \exp[iH_0(t-t_0)]H_{\text{int}}(\boldsymbol{x})\exp[-iH_0(t-t_0)]$$
$$U(t,t_0) = T\{\exp[-i\int_{t_0}^{t} dt' H_I(t')]\} \tag{5-21}$$

Similar as Eq. (5-12), we can expand $U(t,t_0)$ in perturbation series up to the leading order which is the first order as

$$U(t,t_0) = 1 + (-i)\int_{t_0}^{t} dt_1 H_I(t_1) \tag{5-22}$$

In order to make a comparison of the dynamical formalism of the electron P between QED and OPQM, we need to apply the same method to remove the rotating-time-dependence in Eq. (5-22). By integrating over an infinite time period then we can obtain the matrix elements of $U(t,t_0)$ expanded in momentum basis as $\langle \boldsymbol{p}'|U(\infty,-\infty)|\boldsymbol{p}\rangle$. After plugging $H_I(t)$ from Eq. (5-21) into $\langle \boldsymbol{p}'|U(\infty,-\infty)|\boldsymbol{p}\rangle$, we get results containing $2\pi\delta(\omega_{\boldsymbol{p}'} - \omega_{\boldsymbol{p}})$ which put an energy conservation constraint on the initial and final state of the electron P, this appears as a serious problem in the formalism of OPQM since we nearly get an identity matrix $U(\infty,-\infty)$. One may notice that this problem can be fixed by introducing another subsystem interacting with P, under this condition, the free energy H_0 in Eq. (5-21) will cover both the electron P and this subsystem, the overall energy is conserved by performing the time integration. Bearing in mind that our target is to derive the classical four-potential $A_\mu(\boldsymbol{x})$ from QED process, therefore, we can just focus on the dynamical evolutions of the electron P described by QED and OPQM respectively. We get the dynamical transition matrix expanded in momentum basis up to the first order of perturbations as

$$S_0(\boldsymbol{p}', \boldsymbol{p}) + S_1(\boldsymbol{p}', \boldsymbol{p}) = \langle \boldsymbol{p}'|U(\infty,-\infty)|\boldsymbol{p}\rangle \tag{5-23}$$

in which $S_1(\boldsymbol{p}', \boldsymbol{p}) \equiv -iC_1\langle \boldsymbol{p}'|H_{\text{int}}(\boldsymbol{x})|\boldsymbol{p}\rangle$ is the first order transition matrix. The constant factor C_1 carries an inverse energy dimension which may indicate the overall energy conservation obtained from the infinite-time-integration technique. For the zeroth order perturbation expansion $S_0(\boldsymbol{p}', \boldsymbol{p}) \equiv \langle \boldsymbol{p}'|\boldsymbol{p}\rangle$, if we attach the other

subsystem such as $|\Psi\rangle$, we would obtain an additional term as $\langle\Psi|\Psi\rangle$ which also appears in Eq. (5-19). The information of a non-trivial dynamical transition between the states of electron P is carried by the first order perturbation term $S_1(\boldsymbol{p}', \boldsymbol{p})$. For the AB effect depicted in Fig. 5-1, in order to get the OPQM transition matrix from QED theory, we divide the combined system $|\Psi, \boldsymbol{p}\rangle$ into two separable systems, that is,

$$\hat{U}_{QED}|\Psi, \boldsymbol{p}\rangle = \hat{U}_{QED}|\Psi\rangle \otimes \hat{U}|\boldsymbol{p}\rangle \tag{5-24}$$

in which $\hat{U}$ is Eq. (5-22) and $\hat{U}_{QED}$ is Eq. (5-12) and the right hand side of Eq. (5-24) is a tensor product of two systems which are $|\Psi\rangle$ and the electron P. The left hand side of Eq. (5-24) is the evolution of the combined system $|\Psi, \boldsymbol{p}\rangle$ governed by the QED theory, the right hand side is the evolution of $|\Psi\rangle$, which is governed by QED theory, and the evolution of P which is governed by OPQM theory, these two kinds of descriptions of the evolution of system $|\Psi, \boldsymbol{p}\rangle$ need to be equivalent. Practically, if we are only interested in the evolution of P, then we need to construct the OPQM theory to describe P which is $\hat{U}|\boldsymbol{p}\rangle$, however, we still get another system $|\Psi\rangle$, thus, we just tensor product it with P. The Eq. (5-24) holds under the condition that the electron P is distinguishable from any electron inside of the system $|\Psi\rangle$, this means that the state of P, which is $|\boldsymbol{p}\rangle \equiv \sqrt{2\omega_{\boldsymbol{p}}}c_{\boldsymbol{p}}^{\dagger}|0\rangle$, is orthogonal with any electron's state inside of $|\Psi\rangle$ during the evolution and the exchanging between the electron P with any electron inside of $|\Psi\rangle$ is not allowed, such separable condition, the same as what we mentioned below Eq. (5-14), is satisfied in the AB effect since the electron P is travelling outside of the solenoid while the system $|\Psi\rangle$ is confined in the solenoid as depicted in Fig. 5-1. Moreover, the Eq. (5-24) holds under the approximation that the influence on system $|\Psi\rangle$ acted by the electron P is negligible, therefore, the evolution of the system $|\Psi\rangle$ is fully controlled by the internal interactions expressed by $\hat{U}_{QED}|\Psi\rangle$. Indeed, for a macroscopic system $|\Psi\rangle$ involving N electrons, the

evolution of any electron inside of $|\Psi\rangle$ is controlled by the other $N-1$ electrons plus the electron P, therefore, it would be reasonable that we only omit the effect caused by the single electron P in case that $N \to \infty$. The Eq. (5-24) will not be valid in cases of a time-varying state $|\Psi(t)\rangle$ driven by some other external forces generated by a third party system interacting with $|\Psi\rangle$, this is due to the fact that the evolution of system $|\Psi\rangle$ cannot be expressed as $\hat{U}_{QED}|\Psi\rangle$ in presence of some external forces. Meanwhile, the influence on P caused by the system $|\Psi\rangle$ is expressed by the OPQM evolution operator $\hat{U}$, therefore, this $\hat{U}$ is dependent on the system $|\Psi\rangle$ and our target is to construct the appropriate $\hat{U}$ to satisfy the Eq. (5-24). Furthermore, we product the state $\langle \boldsymbol{p}', \Psi| \equiv \langle 0|\sqrt{2\omega_{\boldsymbol{p}'}}c_{\boldsymbol{p}'} \otimes \langle \Psi|$ from left on both sides of Eq. (5-24) and get

$$\langle \boldsymbol{p}', \Psi|\hat{U}_{QED}|\Psi, \boldsymbol{p}\rangle = \langle \Psi|\hat{U}_{QED}|\Psi\rangle\langle \boldsymbol{p}'|\hat{U}|\boldsymbol{p}\rangle \tag{5-25}$$

in which $\langle \boldsymbol{p}', \Psi|$ is the tensor product of an free state of P with momentum $\boldsymbol{p}'$ and the initial state of system $|\Psi\rangle$, the right hand side can be given as the product of two matrix elements under the separable condition. To be specific, we denote the N electrons state $|\Psi\rangle$ as

$$|\Psi\rangle \equiv 2^{\frac{N}{2}}\sqrt{\omega_{\boldsymbol{k}_1}\omega_{\boldsymbol{k}_2}\cdots\omega_{\boldsymbol{k}_N}}\,c^{\dagger}_{\boldsymbol{k}_1}c^{\dagger}_{\boldsymbol{k}_2}\cdots c^{\dagger}_{\boldsymbol{k}_N}|0\rangle \tag{5-26}$$

in which $c^{\dagger}_{\boldsymbol{k}_j}$ ($j = 1, 2, \cdots, N$) represents the creation operator of a free electron state with momentum $\boldsymbol{k}_j$, we have the condition that any two electrons' states are orthogonal, i.e., $\langle 0|c_{\boldsymbol{k}_i}c^{\dagger}_{\boldsymbol{k}_j}|0\rangle \propto \delta_{ij}$, by Pauli exclusion principle. The left hand side of Eq. (5-25) can be written as

$$\langle \boldsymbol{p}', \Psi|\hat{U}_{QED}|\Psi, \boldsymbol{p}\rangle = \langle \boldsymbol{p}', \Psi|\hat{S}_0^{QED}|\Psi, \boldsymbol{p}\rangle + \langle \boldsymbol{p}', \Psi|\hat{S}_2^{QED}|\Psi, \boldsymbol{p}\rangle + \cdots \tag{5-27}$$

in which $\langle \boldsymbol{p}', \Psi | \hat{S}_0^{QED} | \Psi, \boldsymbol{p} \rangle = \langle \Psi | \Psi \rangle \langle \boldsymbol{p}' | \boldsymbol{p} \rangle$ under the separable condition, note that the first order $\langle \boldsymbol{p}', \Psi | \hat{S}_1^{QED} | \Psi, \boldsymbol{p} \rangle = 0$. The second order term can be written as two parts, that is,

$$\begin{aligned} &\langle \boldsymbol{p}', \Psi | \hat{S}_2^{QED} | \Psi, \boldsymbol{p} \rangle \\ &= \langle \Psi | \hat{S}_2^{QED} | \Psi \rangle \langle \boldsymbol{p}' | \boldsymbol{p} \rangle + \sum_{i=1}^{N} \sum_{j=1}^{N} (-1)^{i+j} \langle \boldsymbol{p}', \boldsymbol{k}_i | \hat{S}_2^{QED} | \boldsymbol{k}_j, \boldsymbol{p} \rangle \langle \Psi - i | \Psi - j \rangle \end{aligned} \tag{5-28}$$

in which $|\boldsymbol{k}_j, \boldsymbol{p}\rangle \equiv 2\sqrt{\omega_{\boldsymbol{p}} \omega_{\boldsymbol{k}_j}} c_{\boldsymbol{k}_j}^{\dagger} c_{\boldsymbol{p}}^{\dagger} |0\rangle$ and $\langle \boldsymbol{p}', \boldsymbol{k}_i | \equiv \langle 0 | 2\sqrt{\omega_{\boldsymbol{p}'} \omega_{\boldsymbol{k}_i}} c_{\boldsymbol{p}'} c_{\boldsymbol{k}_i}$. The first term on the right hand side of Eq. (5-28) is the internal interactions inside of system $|\Psi\rangle$ leaving the electron P unaffected which is the same as Eq. (5-17), the second term express the interactions between P and the system $|\Psi\rangle$, later on we will see that the first order OPQM transition matrix arise from this term. $|\Psi - j\rangle$ is defined as the state of the remaining system after the removal of $|\boldsymbol{k}_j\rangle$, that is,

$$|\Psi - j\rangle \equiv 2^{\frac{N-1}{2}} \sqrt{\omega_{\boldsymbol{k}_1} \ldots \omega_{\boldsymbol{k}_{j-1}} \omega_{\boldsymbol{k}_{j+1}} \cdots \omega_{\boldsymbol{k}_N}} c_{\boldsymbol{k}_1}^{\dagger} \cdots c_{\boldsymbol{k}_{j-1}}^{\dagger} c_{\boldsymbol{k}_{j+1}}^{\dagger} \cdots c_{\boldsymbol{k}_N}^{\dagger} |0\rangle \tag{5-29}$$

Similarly, the state $|\Psi - i\rangle$ is

$$\langle \Psi - i | \equiv \langle 0 | 2^{\frac{N-1}{2}} \sqrt{\omega_{\boldsymbol{k}_1} \ldots \omega_{\boldsymbol{k}_{i-1}} \omega_{\boldsymbol{k}_{i+1}} \cdots \omega_{\boldsymbol{k}_N}} c_{\boldsymbol{k}_N} \cdots c_{\boldsymbol{k}_{i+1}} c_{\boldsymbol{k}_{i-1}} \cdots c_{\boldsymbol{k}_1} \tag{5-30}$$

The right hand side of Eq. (5-27) expanded in leading order of perturbations can be given as

$$\begin{aligned} &\langle \boldsymbol{p}' | \hat{U} | \boldsymbol{p} \rangle \langle \Psi | \hat{U}_{QED} | \Psi \rangle \\ &= \langle \boldsymbol{p}' | \boldsymbol{p} \rangle \langle \Psi | \Psi \rangle + \langle \boldsymbol{p}' | \boldsymbol{p} \rangle \langle \Psi | \hat{S}_2^{QED} | \Psi \rangle + \langle \boldsymbol{p}' | \hat{S}_1 | \boldsymbol{p} \rangle \langle \Psi | \Psi \rangle + \cdots \end{aligned} \tag{5-31}$$

Compare Eq. (5-31) with Eq. (5-29) and Eq. (5-30), we get

$$\langle \boldsymbol{p}' | \hat{S}_1 | \boldsymbol{p} \rangle = \sum_{i=1}^{N} \sum_{j=1}^{N} (-1)^{i+j} \frac{\langle \Psi - i | \Psi - j \rangle}{\langle \Psi | \Psi \rangle} \langle \boldsymbol{p}', \boldsymbol{k}_i | \hat{S}_2^{QED} | \boldsymbol{k}_j, \boldsymbol{p} \rangle \tag{5-32}$$

For the terms with $i \neq j$, $\langle \Psi - i | \Psi - j \rangle = 0$ due to the Pauli exclusion principle, therefore, we get

$$\langle \boldsymbol{p}' | \hat{S}_1 | \boldsymbol{p} \rangle = \sum_{j=1}^{N} \frac{\langle \boldsymbol{p}', \boldsymbol{k}_j | \hat{S}_2^{QED} | \boldsymbol{k}_j, \boldsymbol{p} \rangle}{\langle \boldsymbol{k}_j | \boldsymbol{k}_j \rangle} \tag{5-33}$$

For a two electrons system $|\Psi, \boldsymbol{p}\rangle = |\boldsymbol{k}, \boldsymbol{p}\rangle$, the first order transition matrix can be given as

$$\langle \boldsymbol{p}' | \hat{S}_1 | \boldsymbol{p} \rangle = \frac{\langle \boldsymbol{p}', \boldsymbol{k} | \hat{S}_2^{QED} | \boldsymbol{k}, \boldsymbol{p} \rangle}{\langle \boldsymbol{k} | \boldsymbol{k} \rangle} \tag{5-34}$$

Thus, in order to determine the mathematical structure of $A_\mu(\boldsymbol{x})$, we can divide $S_1(\boldsymbol{p}', \boldsymbol{p}) \equiv \langle \boldsymbol{p}' | \hat{S}_1 | \boldsymbol{p} \rangle$ into two terms as

$$S_1(\boldsymbol{p}', \boldsymbol{p}) = ieC_1(\langle \boldsymbol{p}' | \phi(\boldsymbol{x}) | \boldsymbol{p} \rangle - \langle \boldsymbol{p}' | \gamma^0 \boldsymbol{\gamma} \cdot \boldsymbol{A}(\boldsymbol{x}) | \boldsymbol{p} \rangle) \tag{5-35}$$

To be more specific, let us take a review of two electrons' scattering process governed by QED physics. By comparing Eq. (5-35) with Eq. (5-14), note that in this case $C_1 = 2\pi\delta(\omega_{p'} + \omega_{k'} - \omega_p - \omega_k)$, $|\Psi\rangle = |\boldsymbol{k}\rangle \equiv \sqrt{2\omega_k} c_k^\dagger |0\rangle$, the state of the electron P is $\langle \boldsymbol{x} | \boldsymbol{p} \rangle = u_p e^{i\boldsymbol{p}\cdot\boldsymbol{x}}$ with $\langle \boldsymbol{x}| \equiv \langle 0 | \hat{\psi}(\boldsymbol{x})$ and $|\boldsymbol{p}\rangle \equiv \sqrt{2\omega_p} c_p^\dagger |0\rangle$, with the application of Eq. (5-34), the classical potentials can be given as

$$\begin{aligned} \phi_k(\boldsymbol{x}) &= \frac{-e}{2\omega_k} \int \frac{d^3\boldsymbol{q}}{(2\pi)^3} \frac{\bar{u}_k \gamma^0 u_k}{|\boldsymbol{q}|^2} \exp(i\boldsymbol{q}\cdot\boldsymbol{x}) \\ A_k^i(\boldsymbol{x}) &= \frac{-e}{2\omega_k} \int \frac{d^3\boldsymbol{q}}{(2\pi)^3} \frac{\bar{u}_k \gamma^i u_k}{|\boldsymbol{q}|^2} \exp(i\boldsymbol{q}\cdot\boldsymbol{x}) \end{aligned} \tag{5-36}$$

with $\boldsymbol{q} \equiv \boldsymbol{p}' - \boldsymbol{p}$. Note that the classical four-potential given above is negative due to the positive coupling constant e, this agrees with what we have been taught in classical physics: the electrons which carry negative charges create negative potentials. One may also notice that in the above expression of $A_k^\mu(\boldsymbol{x})$, we neglected $(\omega_p - \omega_{p'})^2$ in the denominator, this is due to the fact that the potential $A_k^\mu(\boldsymbol{x})$ cannot

be formulated as space-coordinate functions by including $(\omega_{\boldsymbol{p}} - \omega_{\boldsymbol{p}'})^2$, therefore, the mathematical structure of OPQM fails to provide a precise description of the high energy particles' interactions since the potential $A_{\boldsymbol{k}}^{\mu}(\boldsymbol{x})$ cannot be well defined in the high energy domain and it only arise from low energy physical phenomena, more discussions over such point of view can be seen in Appendix D. The electron static four-current can be given as

$$j_{\boldsymbol{k}}^{\mu}(\boldsymbol{x}) \equiv \frac{-e}{2\omega_{\boldsymbol{k}}} \int \frac{d^3\boldsymbol{q}}{(2\pi)^3} \bar{u}_{\boldsymbol{k}} (\gamma^{\mu} - \frac{\boldsymbol{\gamma} \cdot \boldsymbol{q}}{\boldsymbol{q}}) u_{\boldsymbol{k}} \exp(i\boldsymbol{q} \cdot \boldsymbol{x}) \tag{5-37}$$

this gives the static classical Maxwell equations as

$$\vec{\nabla}^2 A_{\boldsymbol{k}}^{\mu}(\boldsymbol{x}) - \vec{\nabla}\vec{\nabla} \cdot \boldsymbol{A}_{\boldsymbol{k}}(\boldsymbol{x}) = -j_{\boldsymbol{k}}^{\mu}(\boldsymbol{x}) \tag{5-38}$$

Note that we have the expression $\gamma^{\mu} - \frac{\boldsymbol{\gamma} \cdot \boldsymbol{q}}{\boldsymbol{q}}$ inside of the four-current $j_{\boldsymbol{k}}^{\mu}(\boldsymbol{x})$ given above, that is, we subtract the component which is parallel to the momentum $\boldsymbol{q}$, this ensures the total classical charge conservation given as $\partial_{\mu} j_{\boldsymbol{k}}^{\mu}(\boldsymbol{x}) = 0$. Meanwhile, the transition matrix $S_1(\boldsymbol{p}', \boldsymbol{p})$ obtained from $S_2^{QED}(\boldsymbol{p}', \boldsymbol{p})$ via Eq. (5-34) does not depend on the gauge that we choose, however, the four-potential $A_{\boldsymbol{k}}^{\mu}(\boldsymbol{x})$ given in Eq. (5-36) do depend on the gauge, which is the Feynman gauge in our case, that we apply to calculate $S_2^{QED}(\boldsymbol{p}', \boldsymbol{p})$, one can also try to apply other gauges to derive different mathematical expressions of $A_{\boldsymbol{k}}^{\mu}(\boldsymbol{x})$.

As we can see, the expression $A_{\boldsymbol{k}}^{\mu}(\boldsymbol{x})$ obtained from Eq. (5-36) carries a state $|\boldsymbol{k}\rangle$ dependency, this agrees with what we mentioned earlier below Eq. (5-18), i.e., the structure of $S_2^{QED}(\boldsymbol{p}', \boldsymbol{p})$ depends on the configuration of $|\Psi\rangle$. As we can see now, the "source" of the stationary classical four-potential $A_{\mu}(\boldsymbol{x})$ can be traced back to a relativistic quantum field, i.e., the Dirac electron field which we denoted as state $|\Psi\rangle$ in this scenario, the mathematical expressions of $A_{\mu}(\boldsymbol{x})$ appear to be completely arbitrary in real situations due to the fact that the limitless configurations of the state $|\Psi\rangle$ can be found in real world. Note that the infinite-time-integration approach

cannot be applied in case of a time-varying function $A_\mu(t,\boldsymbol{x})$ to the derivations from Eq. (5-22) to Eq. (5-23). Indeed, we expect to obtain a time-varying function $A_\mu(t,\boldsymbol{x})$ in case of a macroscopically-varying state $|\Psi(t)\rangle$ driven by some external forces and such external forces would be generated by a third party system interacting with $|\Psi\rangle$, some specific examples with external forces can be a subject for future investigations. Now it is clear that, in the AB effect, it does not matter whether the EMF are zero or not in the region where P can enter, the underlying mechanism is the interactions between P and $|\Psi\rangle$ while such interactions are mediated by virtual photons.

In summary, since the basic building blocks of nature are mathematically constructed as relativistic fields in quantum field theory framework, we believe that the macroscopic phenomenon or classical and OPQM theories originally arise from the collective effects among these fundamental quantum fields. With this belief, we reviewed physical theories from microscopic world to macroscopic world, that is from Eq. (5-9) to Eq. (5-20), i.e., from QED to OPQM then from OPQM, we now see clearly how physical quantities, such as the classical potential $A_\mu(t,\boldsymbol{x})$ and EMF introduced from Eq. (5-3), were developed step by step. Since we showed that the OPQM is just an approximated model which arises from quantum field theory, therefore all the physical phenomena that are predicted by OPQM can find their counterpart explanations in quantum field theory, including the AB effect. In fact, the nonlocal feature in AB effect can be interpreted as the manifestation of virtual photons propagating between electrons in the framework of QED. At last, we note that the introduction of EMF from Eq. (5-3) become essential only in classical physics since, as we can see in Eq. (5-4), the EMF is directly linked with velocity and acceleration, which can be easily measured, of macroscopic objects.

6. CONCLUSIONS

As conclusions of this thesis, we theoretically investigated the cavity QED in some 2D materials such as monolayer MoS_2, BP and graphene systems under perpendicular magnetic field. The results show that these systems can enter the ultrastrong light-matter coupling regime. But, in contrast to conventional semiconductors, these 2D systems show a quantum phase transition. In monolayer MoS_2 resonator, electron-hole asymmetry can still play an important role in determining magnetopolariton dispersion which is different from monolayer graphene system. Moreover, in contrast with some other 2D materials, the monolayer BP system shows three branches of polaritons and the energy gap between these polaritons is much larger, this is caused by the anisotropic behavior displayed in the tight binding Hamiltonian of the BP system. For the graphene system, we considered the coupling of cyclotron transition and a multimode cavity described by a multimode Dicke model. In contrast to the single mode case, multimode coupling of cavity photon and cyclotron transition can greatly reduce the critical vacuum Rabi frequency required for quantum phase transition, and dramatically enhance the superradiant emission by fast modulating the Hamiltonian. Our study provides a theoretical foundation for the observation and investigation of cavity QED for fundamental studies and quantum applications in these 2D systems.

At the last chapter, we studied the AB effect within the quantum field theoy framework. We provide a quantum treatment of the source of the electromagnetic potential and showed that the underlying mechanism in AB effect can be viewed as interactions between electrons described by QED theory where the interactions are mediated by virtual photons. We further showed that the framework of one particle quantum mechanics (OPQM) can be given, in general, as a mathematically approximated model which is reformulated from QED theory. In addition, the classical Maxwell equations are derived from QED scattering process while both classical electromagnetic fields and potentials serve as mathematical tools that are constructed to approximate the interactions among elementary particles described by QED physics. This work serves as a link from quantum field theory to one particle quantum mechanics and also shed a new light on the nature of the electromagnetic vector potentials.

APPENDIX A

In this appendix, we are going to briefly introduce the concept of LLs which comprise important parts in the first part of our work and meanwhile plays a major role in the magnetic properties of solid materials. For a charged particle placed in a constant magnetic field $\boldsymbol{B} = (0, 0, B)$ which lies along the z axis, the Hamiltonian can be given as

$$H = \frac{\boldsymbol{p}^2}{2m} \tag{A1}$$

In which the canonical momentum $\boldsymbol{p}$ is

$$\boldsymbol{p} \equiv -i\hbar\vec{\nabla} - q\boldsymbol{A} \tag{A2}$$

Landau levels in Landua gauge

In Landau gauge with the electromagnetic vector potential $\boldsymbol{A} = (0, Bx, 0)$, the Schrödinger equation becomes

$$H\psi = \frac{(-i\hbar\vec{\nabla} - q\boldsymbol{A})^2}{2m}\psi = E\psi \tag{A3}$$

Upon substitution of $\boldsymbol{A} = (0, Bx, 0)$ into Eq. (A3), we get

$$\frac{\hbar^2}{2m}[-\nabla_x^2 + (i\nabla_y + \frac{qBx}{\hbar})^2]\psi(x, y) = E\psi(x, y) \tag{A4}$$

Now we see that this Hamiltonian is independent of y , therefore, we can separate the wavefunction $\psi(x, y) = \exp(iky)\phi(x)$. Upon the introduction of the cyclotron frequency $\omega_c \equiv \frac{qB}{m}$, the Eq. (A4) can be written in a more elgant form as

$$[-\frac{\hbar^2}{2m}\nabla_x^2 + \frac{m\omega_c^2}{2}(x + \frac{i\hbar\nabla_y}{m\omega_c})^2]\psi(x, y) = E\psi(x, y) \tag{A5}$$

Next we replace $\psi(x, y)$ using $\exp(iky)\phi(x)$, we obtain

$$[-\frac{\hbar^2}{2m}\nabla_x^2+\frac{m\omega_c^2}{2}(x-\frac{\hbar k}{m\omega_c})^2]\phi(x)=E\phi(x) \tag{A6}$$

Notice that Eq. (A6) is the Schrödinger equation of 1-D quantum harmonic oscillator except with the minimum of the potential shifted in coordinate space by $x_0=\frac{\hbar k}{m\omega_c}$.

Thus, the energy spectrum is identical to those of the standard quantum harmonic oscillator problem with

$$E_n=\hbar\omega_c(n+\frac{1}{2}) \tag{A7}$$

In which n can be any non-negative integers. Meanwhile, the eigenstates can be given as

$$\psi(x,y)=\exp(iky)\phi_n(x-x_0) \tag{A8}$$

In which $\phi_n(x-x_0)$ is the wavefunction of the standard quantum harmonic oscillator $\phi_n(x)$ with the coordinated space shifted by x_0.

Landau levels in symmetric gauge

In symmetric gauge, the vector potential can be written as

$$\boldsymbol{A}=\frac{1}{2}(-By,Bx,0) \tag{A9}$$

With this choice of vector potential, the Hamiltonian of the charged particle in the magnetic field can be given as

$$H=\frac{\hbar^2}{2m}[(i\nabla_x-\frac{qBy}{2\hbar})^2+(i\nabla_y+\frac{qBx}{2\hbar})^2] \tag{A10}$$

Introducing new operators

$$\begin{aligned} a&=\frac{1}{\sqrt{2}}[(\frac{y}{2l_B}+l_B\nabla_y)-i(\frac{x}{2l_B}+l_B\nabla_x)] \\ a^\dagger&=\frac{1}{\sqrt{2}}[(\frac{y}{2l_B}-l_B\nabla_y)+i(\frac{x}{2l_B}-l_B\nabla_x)] \end{aligned} \tag{A11}$$

in which $l_B \equiv \sqrt{\frac{\hbar}{qB}}$ is the magnetic length and the bosonic operators satisfy the communation relation $[a, a^\dagger] = 1$. Upon substitution of new operators into Eq. (A10), we obtain

$$H = \hbar\omega_c (a^\dagger a + \frac{1}{2}) \tag{A12}$$

Therefore, the energy spectrum can be given as

$$E_n = \hbar\omega_c (n + \frac{1}{2}) \tag{A13}$$

in which n indicate the Landau level index.

APPENDIX B

In this appendix, we discussed three quantization cases for the optical modes in the cavity following the Ref. [100].

The cavities that we are going to discuss are enclosed by rectangular walls having length L_x, L_y and L_z in three directions respectively. The electromagnetic vector potential in the cavity can be written as

$$\boldsymbol{A}_{em} = \sum_{\eta=1,2} \sqrt{\frac{\hbar}{2\varepsilon_0 \varepsilon \omega_c}} (\boldsymbol{u}_\eta a_\eta + \boldsymbol{u}_\eta^\dagger a_\eta^\dagger) \tag{B1}$$

In which ω_c is the frequency of the electromagnetic fields, ε_0 is the dielectric constant of the vacuum and ε is the dielectric constant of the 2D material under study. Following the discussion of Ref. [100], we are going to discuss three cases of cavities.

Case 1. We assume that L_x, $L_y \gg L_z$ and the wall in the z direction is perfectly conducting. The wave-vector in this case can be given as

$$\boldsymbol{k} = \left(\frac{2\pi n_x}{L_x}, \frac{2\pi n_y}{L_y}, \frac{\pi n_z}{L_z}\right) \tag{B2}$$

in which (n_x, n_y, n_z) are integers and the two independent cavity modes in Eq. (B1) can be given as

$$u_1 = \sqrt{\frac{2}{V}} e^{ik_x x} e^{ik_y y} \begin{pmatrix} i\sin(k_z z)\cos(\theta)\cos(\phi) \\ i\sin(k_z z)\cos(\theta)\sin(\phi) \\ -\cos(k_z z)\sin(\theta) \end{pmatrix}, u_2 = \sqrt{\frac{2}{V}} e^{ik_x x} e^{ik_y y} \begin{pmatrix} -i\sin(k_z z)\sin(\phi) \\ i\sin(k_z z)\cos(\phi) \\ 0 \end{pmatrix} \tag{B3}$$

In which V is the volume of the cavity and the spherical angle (θ, ϕ) can be determained upon specific values of (n_x, n_y, n_z) using the relation $\boldsymbol{k} = |\boldsymbol{k}|(\sin\theta\cos\phi, \sin\theta\sin\phi, \cos\phi)$ with Eq. (B2).

Case 2. We assume that the wall in the y and z direction are perfectly conducting. The wave-vector in this case can be given as

$$\boldsymbol{k} = (\frac{2\pi n_x}{L_x}, \frac{\pi n_y}{L_y}, \frac{\pi n_z}{L_z}) \tag{B4}$$

The two independent cavity modes can be given as

$$\begin{aligned} u_1 &= \frac{2}{\sqrt{V}} e^{ik_x x} \begin{pmatrix} i\sin(k_z z)\sin(k_y y)\cos(\theta)\cos(\phi) \\ i\sin(k_z z)\cos(k_y y)\cos(\theta)\sin(\phi) \\ -\cos(k_z z)\sin(k_y y)\sin(\theta) \end{pmatrix} \\ u_2 &= \frac{2}{\sqrt{V}} e^{ik_x x} \begin{pmatrix} -i\sin(k_z z)\sin(k_y y)\sin(\phi) \\ \sin(k_z z)\cos(k_y y)\cos(\phi) \\ 0 \end{pmatrix} \end{aligned} \tag{B5}$$

Note that in this case, for the situation $k_y = 0$ or $k_z = 0$, $\frac{2}{\sqrt{V}}$ in Eq. (B5) needs to be replaced by $\sqrt{\frac{2}{V}}$.

Case 3. We assume that the walls in all three directions are perfectly conducting. The wave-vector in this case can be given as

$$\boldsymbol{k} = (\frac{\pi n_x}{L_x}, \frac{\pi n_y}{L_y}, \frac{\pi n_z}{L_z}) \tag{B6}$$

The two independent cavity modes can be given as

$$\begin{aligned} u_1 &= \sqrt{\frac{8}{V}} \begin{pmatrix} \sin(k_z z)\sin(k_y y)\cos(k_x x)\cos(\theta)\cos(\phi) \\ \sin(k_z z)\cos(k_y y)\sin(k_x x)\cos(\theta)\sin(\phi) \\ -\cos(k_z z)\sin(k_y y)\sin(k_x x)\sin(\theta) \end{pmatrix} \\ u_2 &= \sqrt{\frac{8}{V}} \begin{pmatrix} -\sin(k_z z)\sin(k_y y)\cos(k_x x)\sin(\phi) \\ \sin(k_z z)\cos(k_y y)\sin(k_x x)\cos(\phi) \\ 0 \end{pmatrix} \end{aligned} \tag{B7}$$

APPENDIX C

Here, we are going to obtain the classical EMF from the multi-particle interactions treated in the framework of QED theory. The following discussions will be based on

a mathematical model chosen for convenience and the complex real-world situations would be comprised of all kinds of configurations of atoms that involve other quantum particles, such as protons and neutrons, which are beyond our discussions. Therefore, the "source" of the classical potential $A_\mu(\boldsymbol{x})$ are made of N electrons which can be constructed as a quantum state $|\Psi\rangle$; note that N is a very large number in order to produce some significant effects on P at a macroscopic distance as shown in Fig. 5-1. We now write $|\Psi\rangle$ in Slater determinant form as

$$|\Psi\rangle = \frac{1}{\sqrt{N!}} \begin{vmatrix} |\psi_1\rangle_1 & |\psi_2\rangle_1 & \cdots & |\psi_N\rangle_1 \\ |\psi_1\rangle_2 & |\psi_2\rangle_2 & \cdots & |\psi_N\rangle_2 \\ \vdots & \vdots & \ddots & \vdots \\ |\psi_1\rangle_N & |\psi_2\rangle_N & \cdots & |\psi_N\rangle_N \end{vmatrix} \tag{C1}$$

in which $|\psi_j\rangle_i$ represents that the electron i is in state $|\psi_j\rangle$. For the second order perturbation term of Eq. (5-16), we have

$$\langle \boldsymbol{p}', \Psi | \int d^3\boldsymbol{x} d^3\boldsymbol{y} [e^2 \hat{\bar{\psi}}_I(\boldsymbol{x}, t_1) \gamma_\mu \hat{A}_I^\mu(\boldsymbol{x}, t_1) \hat{\psi}_I(\boldsymbol{x}, t_1) \hat{\bar{\psi}}_I(\boldsymbol{y}, t_2) \gamma_\nu \hat{A}_I^\nu(\boldsymbol{y}, t_2) \hat{\psi}_I(\boldsymbol{y}, t_2)] | \Psi, \boldsymbol{p} \rangle \tag{C2}$$

Plug Eq. (C1) into Eq. (C2), we can exclude the terms arising from interactions between the N electrons within $|\Psi\rangle$ since these interactions are irrelevant to the evolution of P. Next we are going to find out how the multi-particle classical potentials emerge from Eq. (C2). For macroscopically charged particles, they are well localized in space, this localization can be matched by demanding that the state of each electron j is confined in a different small volume x_j^3 such that the orthogonal condition $\langle \psi_i | \psi_j \rangle \propto \delta_{ij}$ is valid, therefore, Eq. (C2) can be transformed into

$$\sum_{j=1}^{N} \langle \boldsymbol{p}', \psi_j | \int d^3\boldsymbol{x} d^3\boldsymbol{y} [e^2 \hat{\bar{\psi}}_I(\boldsymbol{x}, t_1) \gamma_\mu \hat{A}_I^\mu(\boldsymbol{x}, t_1) \hat{\psi}_I(\boldsymbol{x}, t_1) \hat{\bar{\psi}}_I(\boldsymbol{y}, t_2) \gamma_\nu \hat{A}_I^\nu(\boldsymbol{y}, t_2) \hat{\psi}_I(\boldsymbol{y}, t_2)] | \psi_j, \boldsymbol{p} \rangle \tag{C3}$$

up to a factor $\prod_{m\neq j}^{N}\langle\psi_m|\psi_m\rangle$, which is contributed from the rest $N-1$ electrons, in front of each summation term in Eq. (C3). The Eq. (C3) indeed displays a very clear physical picture, the potential energy of P in the presence of N electrons is the summation over all individual contributions of these electrons, we can also find its counterpart in classical physics, i.e., the electrostatic potential energy of a point charge q in the presence of other N point charges equals to the summation over all the contributions of these point charges. Therefore, in order to simplify the subsequent calculations without losing the physical insight, we replace the general state $|\psi_j\rangle$ with a free quantum state $|\boldsymbol{k}_j\rangle$, perform the infinite-time-integration for Eq. (C3), by using Eq. (5-33) we obtain the first order scattering matrix of OPQM as

$$S_1(\boldsymbol{p}',\boldsymbol{p})=\sum_{j=1}^{N}\frac{-i(2\pi)^4e^2\exp[-i(\boldsymbol{p}'-\boldsymbol{p})\cdot\boldsymbol{x}_j]}{\langle\boldsymbol{k}_j|\boldsymbol{k}_j\rangle|\boldsymbol{p}-\boldsymbol{p}'|^2}(\bar{u}_{\boldsymbol{p}'}\gamma^0u_{\boldsymbol{p}}\bar{u}_{\boldsymbol{k}_j}\gamma^0u_{\boldsymbol{k}_j}-\bar{u}_{\boldsymbol{p}'}\gamma^iu_{\boldsymbol{p}}\bar{u}_{\boldsymbol{k}_j}\gamma^iu_{\boldsymbol{k}_j}) \tag{C4}$$

in which the factor $\exp[-i(\boldsymbol{p}'-\boldsymbol{p})\cdot\boldsymbol{x}_j]$ is to indicate that each electron's state $|\boldsymbol{k}_j\rangle$ in the ensemble is well localized in a small volume x_j^3. Similar as what we have done for two electrons scattering case and notice that $\langle\boldsymbol{k}_j|\boldsymbol{k}_j\rangle=(2\pi)^3 2\omega_{\boldsymbol{k}_j}$, the 2π inside of Eq. (C4) will be cancelled by the factor C_1 in Eq. (5-23). Hence, with Feynman gauge applied, after a short algebra we can obtain the classical multi-particle potentials as

$$\begin{aligned}\phi(\boldsymbol{x})&=\sum_{j=1}^{N}\frac{-e\bar{u}_{\boldsymbol{k}_j}\gamma^0u_{\boldsymbol{k}_j}}{2\omega_{\boldsymbol{k}_j}}\int\frac{d^3\boldsymbol{q}}{(2\pi)^3}\frac{1}{|\boldsymbol{q}|^2}\exp[i\boldsymbol{q}\cdot(\boldsymbol{x}-\boldsymbol{x}_j)]\\ A^i(\boldsymbol{x})&=\sum_{j=1}^{N}\frac{-e\bar{u}_{\boldsymbol{k}_j}\gamma^iu_{\boldsymbol{k}_j}}{2\omega_{\boldsymbol{k}_j}}\int\frac{d^3\boldsymbol{q}}{(2\pi)^3}\frac{1}{|\boldsymbol{q}|^2}\exp[i\boldsymbol{q}\cdot(\boldsymbol{x}-\boldsymbol{x}_j)]\end{aligned} \tag{C5}$$

The above expression can be brought into a more elegant form as

$$A^\mu(\boldsymbol{x})=\sum_{j=1}^{N}\frac{-e\bar{u}_{\boldsymbol{k}_j}\gamma^\mu u_{\boldsymbol{k}_j}}{8\pi\omega_{\boldsymbol{k}_j}|\boldsymbol{x}-\boldsymbol{x}_j|} \tag{C6}$$

the electron static four-current can be given as

$$j^{\mu}(\boldsymbol{x}) \equiv \sum_{j=1}^{N} \frac{-e}{2\omega_{\boldsymbol{k}_j}} \int \frac{d^3\boldsymbol{q}}{(2\pi)^3} \bar{u}_{\boldsymbol{k}_j} (\gamma^{\mu} - \frac{\boldsymbol{\gamma}\cdot\boldsymbol{q}}{\boldsymbol{q}}) u_{\boldsymbol{k}_j} \exp[i\boldsymbol{q}\cdot(\boldsymbol{x}-\boldsymbol{x}_j)] \tag{C7}$$

this gives the static classical Maxwell equations as

$$\vec{\nabla}^2 A^{\mu}(\boldsymbol{x}) - \vec{\nabla}\vec{\nabla}\cdot\boldsymbol{A}(\boldsymbol{x}) = -j^{\mu}(\boldsymbol{x}) \tag{C8}$$

The classical fields $\boldsymbol{E}(\boldsymbol{x})$ and $\boldsymbol{B}(\boldsymbol{x})$ can be introduced following the relation defined in Eq. (5-3) as

$$\begin{aligned} \boldsymbol{E}(\boldsymbol{x}) &= \sum_{j=1}^{N} \frac{-e(\boldsymbol{x}-\boldsymbol{x}_j)}{4\pi\left|\boldsymbol{x}-\boldsymbol{x}_j\right|^3} \\ \boldsymbol{B}(\boldsymbol{x}) &= \sum_{j=1}^{N} \frac{-e\bar{u}_{\boldsymbol{k}_j}\boldsymbol{\gamma}\times(\boldsymbol{x}-\boldsymbol{x}_j)u_{\boldsymbol{k}_j}}{8\pi\omega_{\boldsymbol{k}_j}\left|\boldsymbol{x}-\boldsymbol{x}_j\right|^3} \end{aligned} \tag{C9}$$

Note that the electric field does not depend on the energy of the electrons in the ensemble due to $\bar{u}_{\boldsymbol{k}_j}\gamma^0 u_{\boldsymbol{k}_j} = 2\omega_{\boldsymbol{k}_j}$. Again, the classical fields given in Eq. (C9) will play significant roles in classical physics formulated as Lorentz equation of motion and they play no role in the theoretically formulation of both QED and OPQM. We can further obtain the static Maxwell equations written in EMF form as

$$\begin{aligned} \vec{\nabla}\cdot\boldsymbol{E}(\boldsymbol{x}) &= j^0(\boldsymbol{x}) \\ \vec{\nabla}\times\boldsymbol{B}(\boldsymbol{x}) &= \vec{j}(\boldsymbol{x}) \end{aligned} \tag{C10}$$

which are Gauss' Law and Ampere's Law respectively for static classical electromagnetic fields.

In the low energy interaction process, we have $\bar{u}_{\boldsymbol{k}_j}\gamma^i u_{\boldsymbol{k}_j} \approx 0$, then the Eq. (C6) reduces to the multi-electron Coulomb potential as $\phi(\boldsymbol{x}) = \sum_{j=1}^{N} \frac{-e}{4\pi\left|\boldsymbol{x}-\boldsymbol{x}_j\right|}$. This is what we expected earlier: the dynamical evolution of one electron governed by OPQM with the classical potentials agrees with QED theory up to the leading order of perturbations.

APPENDIX D

One may believe that the EMF correspond to some real entities of nature, contrary to this belief, we are going to provide more evidence here to show that EMF is nothing but a calculation tool. Before we present our argument, let us try to locate the origin of the misleading conception. In classical theory, we argue that the necessity for the introduction of EMF through Eq. (5-3) which also induces people to believe that EMF corresponds to real entities of nature lies inside of Eq. (5-4). As we can see, the fields

$\boldsymbol{E}(t,\boldsymbol{x})$ and $\boldsymbol{B}(t,\boldsymbol{x})$ can be uniquely identified through Eq. (5-4) with the information of the acceleration and velocity of the charged particle. This fact induces people to believe that function $\boldsymbol{E}(t,\boldsymbol{x})$ and $\boldsymbol{B}(t,\boldsymbol{x})$ correspond to some real entities of nature since they seem can be uniquely valued at every space-time point. However, this follows the belief that the acceleration and velocity of the charged particle correspond to some real quantities and can be uniquely valued at every space-time point along the trajectory. Now we see that in order to uniquely identify one quantity we need to uniquely identify another since these quantities are bonded together in one equation, measuring quantities $\boldsymbol{E}(t,\boldsymbol{x})$ and $\boldsymbol{B}(t,\boldsymbol{x})$ precisely at every space-time point request us to treat the particle as a single space-time point which has no size, this condition is too unrealistic to be satisfied in classical physics, it demands more internal structures of the macroscopic particle. However, we know that for microscopic particles, the velocity along a trajectory is not well defined due to uncertainty principle, this makes Eq. (5-4) as well as the bond break down in the micro-world. Therefore, for AB effect depicted in Fig. 5-1 based on OPQM theory in radiation gauge, we get the wave-function of the electron as $|\psi\rangle = \exp(-i\int_0^x e\boldsymbol{A}(\boldsymbol{x}')\cdot d\boldsymbol{x}')|\boldsymbol{p}\rangle$ in case of non-time-varying vector potential, the electron traveling enclosing a circle will pick up a phase shift that can be measured which is $\int_S e\boldsymbol{B}(\boldsymbol{x})\cdot d\boldsymbol{S} = e\Phi_m$ where Φ_m is the total magnetic flux through the closed surface, however, remind that two wave-functions with the phase difference of $2n\pi$ ($n = \pm 1, \pm 2\cdots$) still cannot be distinguished. Therefore, neither classical physics nor quantum physics can uniquely quantify $\boldsymbol{E}(t,\boldsymbol{x})$ and $\boldsymbol{B}(t,\boldsymbol{x})$ precisely at every space-time point. This comes as expected actually, since we already argued that the classical potential $A_\mu(t,\boldsymbol{x})$ together with classical EMF defined by Eq. (5-3) is emergent property and arises from QED process. In Eq. (5-4), EMF is introduced to approximate the interactions between charged particles governed by quantum physics.

At this stage, we argue that different physical quantities along with different theories arise at different spatial-temporal scales, the most fundamental nature law at the deepest level may be unique; however, the ignorance of the detailed structures at smaller scales permits physicists to create theories that are approximately effective at

larger scales. Moreover, physicists create mathematical equations which give predictions of the evolutions of nature and the mathematical form of the physical quantities on both sides of the equation needs to be constructed consistently in order to fit the equation form. As we can see from our derivations of the classical potentials given in Eq. (C6), this mathematical form of the classical four-potential is constructed to fit the framework of OPQM in order to give the same predictions with QED theory in low energy limit. Hence, if we view the physical laws from micro-world to macro-world, the emergence of $A_\mu(t,\boldsymbol{x})$ follows from the mathematical construction of the framework of OPQM while the EMF follows from the Lorentz force equation, or equivalently we can say these quantities are bonded with the framework of OPQM and framework of Lorentz force equation respectively. This is the same situation as the two different approaches, which are based on Hamiltonian (Heisenberg approach) and Lagrangian (Feynman Path Integral), to quantum mechanics, these two approaches are equivalent, one should not be confused over this ill-defined question: whether Hamiltonian or Lagrangian are real entities of nature; since these quantities are bonded in the framework of the two different approaches respectively, in a sense that these quantities cannot be divorced from their frameworks and nature does not specify what they are without referring to what roles that they play in the frameworks. To be more specific, let us just simply multiply by 2 on both sides of Eq. (5-4) and rescale the quantities $m'=2m$, $\boldsymbol{E}'(t,\boldsymbol{x})=2\boldsymbol{E}(t,\boldsymbol{x})$ and $\boldsymbol{B}'(t,\boldsymbol{x})=2\boldsymbol{B}(t,\boldsymbol{x})$ such that the equivalence relation with the rescaled quantities still holds [that is, if we revalue the mass of every macroscopic object in our universe, the EMF has to be revalued accordingly], in this way, the new equation with the rescaled quantities works just as good as the old one in a sense that nature does not tell us which one we should use and which quantity, that is $\boldsymbol{E}'(t,\boldsymbol{x})$ or $\boldsymbol{E}(t,\boldsymbol{x})$, should be defined as the real physical entity of nature. Therefore, in this case we can safely speak that, at this macroscopic scale, only the equivalence relation in Eq. (5-4) is the real thing that we should stick with, any transformation of Eq. (5-4) with new defined quantities must mathematically maintain such equivalence relation in order to give the same physical measurement predictions, this is also what happens from Eq. (5-2) to Eq. (5-4). Alternatively, we can rescale the strength of EMF and the charge q instead of m in Eq. (5-4) then the above argument also applies. Moreover, quantities defined at one

scale may break down at another scale, such as color or the temperature of an object which cannot be well defined at the microscopic scale since they are originally from something else that are more fundamental, the similar argument applies to the classical potential $A_\mu(t,\boldsymbol{x})$ and EMF which arise originally from low energy QED physics. In addition, EMF plays no role in the mathematical constructions of OPQM and QED framework, QED and OPQM are complete theories even without the EMF as we can see in Eq. (5-9) and Eq. (5-20). Next we are going to provide another evidence which reaffirm our statement.

Suppose that there exist a static classical field $\boldsymbol{E}(\boldsymbol{x})\neq 0$ and $\boldsymbol{B}(t,\boldsymbol{x})=0$ somewhere in the "source" free region, for simplicity, we assume that the polarization of $\boldsymbol{E}(\boldsymbol{x})$ is in the z direction in reference frame $(t,\boldsymbol{x})$, i.e., $E_x(\boldsymbol{x})=E_y(\boldsymbol{x})=0$. Therefore, the static field $E_z(\boldsymbol{x})$ can be given as

$$E_z(\boldsymbol{x})=i\int\frac{d\omega d^3\boldsymbol{k}}{(2\pi)^3}[\tilde{E}_z(\omega,\boldsymbol{k})e^{-i(\omega t-\boldsymbol{k}\cdot\boldsymbol{x})}-\tilde{E}_z^{\dagger}(\omega,\boldsymbol{k})e^{i(\omega t-\boldsymbol{k}\cdot\boldsymbol{x})}] \tag{D1}$$

in order to get a non-time-varying function $E_z(\boldsymbol{x})$, we require $\tilde{E}_z(\omega,\boldsymbol{k})=\delta(\omega)\tilde{f}(\boldsymbol{k})$ in which $\delta(\omega)$ is the Dirac-Delta function and $\tilde{f}(\boldsymbol{k})$ is a function of wave-vector $\boldsymbol{k}$. Next we perform a Lorentz boost with velocity v in z direction and obtain a new field $E'_z(t',\boldsymbol{x}')$ written in $(t',\boldsymbol{x}')$ frame with relation

$$E'_z(t',\boldsymbol{x}')=E_z(t,\boldsymbol{x}) \tag{D2}$$

The modes expansion of $E'_z(t',\boldsymbol{x}')$ can be given as

$$E'_z(t',\boldsymbol{x}')=i\int\frac{d\omega' d^3\boldsymbol{k}'}{(2\pi)^3}[\tilde{E}'_z(\omega',\boldsymbol{k}')e^{-i(\omega' t'-\boldsymbol{k}'\cdot\boldsymbol{x}')}-\tilde{E}'^{\dagger}_z(\omega',\boldsymbol{k}')e^{i(\omega' t'-\boldsymbol{k}'\cdot\boldsymbol{x}')}] \tag{D3}$$

In the new reference frame we have $\begin{Bmatrix}t'=\gamma(t+vz)\\ z'=\gamma(z+vt)\end{Bmatrix}$ and $\begin{Bmatrix}\omega'=\gamma(\omega+vk_z)\\ k'_z=\gamma(k_z+v\omega)\end{Bmatrix}$ with $\gamma=1/\sqrt{1-v^2}$. Therefore, we can obtain the relation $\tilde{E}_z(\omega,\boldsymbol{k})=\tilde{E}'_z(\omega',\boldsymbol{k}')$ as a result of Eq. (D2) and $e^{i(\omega' t'-\boldsymbol{k}'\cdot\boldsymbol{x}')}=e^{i(\omega t-\boldsymbol{k}\cdot\boldsymbol{x})}$, i.e., the Fourier components of field $E_z(\boldsymbol{x})$ does not change in the new reference frame. This result is also what we expect in quantum

field theory: the probability corresponding to measurement outcomes must be a Lorentz invariant. Plug relation $\tilde{E}_z'(\omega', \boldsymbol{k}') = \delta(\omega)\tilde{f}(\boldsymbol{k})$ into Eq. (D3), after integrating over frequency ω' we find a nonzero value at $\omega' = \gamma v k_z$. Therefore, we have brought a non-time-varying field $E_z(\boldsymbol{x})$ into a time-varying field $E_z'(t', \boldsymbol{x}')$ by a Lorentz boost. Furthermore, we note that something interesting appears: measured in reference frame $(t', \boldsymbol{x}')$, the phase velocity of the modes $e^{-i(\omega' t' - \boldsymbol{k}'\cdot\boldsymbol{x}')}$ in $E_z'(t', \boldsymbol{x}')$ can be given as $u' = \frac{\gamma v k_z}{|\boldsymbol{k}'|}$, therefore, the modes which comprise the field $E_z'(t', \boldsymbol{x}')$ are propagating at speed $u' \le v$ which is slower than light. Thus, the modes in $E_z'(t', \boldsymbol{x}')$ cannot be photons, in fact, neither $E_z'(t', \boldsymbol{x}')$ nor $E_z(\boldsymbol{x})$ can be quantized to bring out photons. The reason is, as we showed in our main text of this article, the EMF are emergent quantities and are not directly linked with some elementary particles, i.e., photons in this scenario.

At this stage, one may wonder whether it is still necessary to treat the EMF as Lorentz tensors which follow the Lorentz transformation rules. To answer this question, let us focus our attention on Eq. (5-20). As we can see from Eq. (5-20) (a more clear observation will be from its Lagrangian rather than Hamiltonian), in order to give a self-consistent theory, the potentials $A_\mu(t, \boldsymbol{x})$ need to follow the transformation the same way as ∂_μ do which is a Lorentz space-time four-gradient. At first sight, we seem to run into some kind of troubles here since the theory request us to treat these emergent quantities as Lorentz tensors. Indeed, our physical theories demands that the mathematical form of physical entities need to be constructed as tensors which transform following the Lorentz transformation rules. However, we are also allowed to attach a tensor-form function to an "imagined" physical entity, such as classical potential $A_\mu(t, \boldsymbol{x})$ and EMF, since we can transform this function in any way we demand without any inconsistencies appearing within the mathematical structure itself, just recall what we have done above. Therefore, we have justified reasons to request the mathematical expressions which represent these emergent quantities, such as $A_\mu(t, \boldsymbol{x})$ and EMF, to obey Lorentz transformation rules as the Eq. (5-20) demands.

For the FEMF introduced following Eq. (5-3) and Eq. (5-10), we have

$$\begin{aligned}\boldsymbol{E}(t,\boldsymbol{x}) &= i\int \frac{d^3\boldsymbol{k}}{(2\pi)^3}\sqrt{\frac{\omega_{\boldsymbol{k}}}{2}}\sum_{\lambda=1,2}[\tilde{E}_{\boldsymbol{k}}^{\lambda}\boldsymbol{\nu}^{\lambda}e^{-i(\omega_{\boldsymbol{k}}t-\boldsymbol{k}\cdot\boldsymbol{x})}-\tilde{E}_{\boldsymbol{k}}^{\lambda\dagger}\boldsymbol{\nu}^{\lambda}e^{i(\omega_{\boldsymbol{k}}t-\boldsymbol{k}\cdot\boldsymbol{x})}] \\ \boldsymbol{B}(t,\boldsymbol{x}) &= i\int \frac{d^3\boldsymbol{k}}{(2\pi)^3}\frac{1}{\sqrt{2\omega_{\boldsymbol{k}}}}\sum_{\lambda=1,2}[\tilde{B}_{\boldsymbol{k}}^{\lambda}\boldsymbol{k}\times\boldsymbol{\nu}^{\lambda}e^{-i(\omega_{\boldsymbol{k}}t-\boldsymbol{k}\cdot\boldsymbol{x})}-\tilde{B}_{\boldsymbol{k}}^{\lambda\dagger}\boldsymbol{k}\times\boldsymbol{\nu}^{\lambda}e^{i(\omega_{\boldsymbol{k}}t-\boldsymbol{k}\cdot\boldsymbol{x})}]\end{aligned} \tag{D4}$$

Note that these quantities above are totally different with EMF in Eq. (5-4). In Eq. (D4), the FEMF is defined from a Lorentz vector in the quantized form as Eq. (5-10), therefore, the FEMF are just two different mathematical constructions that are built of photons, and they, as a result, form a real Lorentz tensor. In addition, the FEMF also plays an essential role in the mathematical formulation of QED theory. However, there is no counterpart of EMF in quantum physics and the EMF emerges in macro-world due to the collective effects from micro-world. Now we see that the FEMF and EMF possess totally different physical meanings, the FEMF are made up of photons which are elementary particles of nature while EMF only serve as mathematical tool in classical physics. The difference in physical meanings between FEMF and EMF originates from the differences between $\hat{A}_{\mu}$ in Eq. (5-9) and $A_{\mu}(\boldsymbol{x})$ in Eq. (5-20) which is a derived quantity; indeed it would be less confusing if people historically have denoted the EMF and FEMF using two different symbols since they hold unrelated physical meanings. Moreover, the mathematical structure of $\hat{A}_{\mu}$ and FEMF are fixed, while $A_{\mu}(\boldsymbol{x})$ and EMF appear to be completely arbitrary in real world. In fact, we should be more careful over the differences of their mathematical structures rather than what historically people have symbolized it, since only their mathematical structures tell us what these quantities really are. At last, speaking of the concept of the physical entity, we do not deny the possibility that the quantum elementary particles are just collective phenomena and arise from some unknown physical processes which are more fundamental; nevertheless, the quantum field theory is the most fundamental tool that people have at current stage to reveal nature's mystery after all.

PUBLICATIONS

1. **B. Li,** T. Liu, D. W. Hewak, Z. Shen and Q. J. Wang, "Ultrastrong light-matter coupling of cyclotron transition in monolayer MoS2," *Phys. Rev. B*, vol. 93, 045420, 2016.
2. **B. Li,** D. W. Hewak, and Q. J. Wang, "A study of Aharonov-Bohm effect: from quantum electrodynamics to one particle quantum mechanics," *arXiv*, 1607.03501, 2016.
3. **B. Li**, T. Liu, D. W. Hewak, and Q. J. Wang, "Superradiant phase transition with graphene embedded in one dimensional optical cavity," Conference on *Lasers and Electro-Optics (CLEO)*, San Jose Convention Center, USA, 15/May-19/May, 2017
4. **B. Li**, Tao Liu, Daniel W. Hewak, and Q. J. Wang, "Superradiant phase transition with graphene embedded in one dimensional optical cavity", Superlattices and Microstructures, 113, 401-408, (2018).
5. **B. Li**, D. W. Hewak, and Q. J. Wang, "The transition from quantum field theory to one-particle quantum mechanics and a proposed interpretation of Aharonov-Bohm effect," Foundations of Physics, 48(7), 837-852 (2018).

BIBLIOGRAPHY

[1] H. Deng, G. Weihs, D. Snoke, J. Bloch, and Y. Yamamoto, "Polariton lasing vs. photon lasing in a semiconductor microcavity.," *Proc. Natl. Acad. Sci. U. S. A.*, vol. 100, no. 26, pp. 15318–15323, 2003.

[2] C. Schneider *et al.*, "An electrically pumped polariton laser," *Nature*, vol. 497, pp. 348–352, 2013.

[3] Y. Kim, S. Yu, and N. Park, "Low-dimensional gap plasmons for enhanced light-graphene interactions," *Sci. Rep.*, vol. 7, no. 43333, 2017.

[4] J. Z. HUA LU, XUETAO GAN, BAOHUA JIA, DONG MAO, "Tunable high-efficiency light absorption of monolayer graphene via Tamm plasmon polaritons," *Opt. Lett.*, vol. 41, no. 20, pp. 4743–4746, 2016.

[5] H. Lu, "Plasmonic characteristics in nanoscale graphene resonator-coupled waveguides," *Appl. Phys. B*, vol. 118, pp. 61–67, 2015.

[6] G. Scalari *et al.*, "Ultrastrong Coupling of the Cyclotron Transition of a 2D Electron Gas to a THz Metamaterial," *Science (80-.).*, vol. 335, no. 6074, pp. 1323–1326, 2012.

[7] I. C. Cristiano Ciuti, Gérald Bastard, "Quantum vacuum properties of the intersubband cavity polariton field," *Phys. Rev. B - Condens. Matter Mater. Phys.*, vol. 72, p. 115303, 2005.

[8] S. De Liberato, C. Ciuti, and I. Carusotto, "Quantum vacuum radiation spectra from a semiconductor microcavity with a time-modulated vacuum rabi frequency," *Phys. Rev. Lett.*, vol. 98, p. 103602, 2007.

[9] R. H. Dicke, "Coherence in Spontaneous Radiation Processes," *Phys. Rev.*, vol. 93, no. 1, pp. 99–110, 1954.

[10] C. Emary and T. Brandes, "Chaos and the quantum phase transition in the Dicke model.," *Phys. Rev. E. Stat. Nonlin. Soft Matter Phys.*, vol. 67, p. 66203, 2003.

[11] N. Lambert, C. Emary, and T. Brandes, "Entanglement and the phase transition in single-mode superradiance.," *Phys. Rev. Lett.*, vol. 92, no. February, p. 73602, 2004.

[12] K. Hepp, R. Field, E. H. Lieb, and K. Etudes, "Equilibrium Statistical Mechanics of Matter Interacting with the Quantized Raljiation Field," *Phys. Rev. A*, vol. 8, no. 5, p. 2517, 1973.

[13] F. T. Hioe, "Phase Transitions in Some Generalized Dicke Models of Snperradiance," *Phys. Rev. A*, vol. 8, no. 3, pp. 1440–1445, 1973.

[14] G. C. Duncan, "Effect of antiresonant atom-field interactions on phase transitions in the Dicke mode," *Phys. Rev. A*, vol. 9, pp. 418–421, 1974.

[15] K. Rzqzewski and K. Wodkiewicz, "Phase Transitions, Two-Level Atoms, and the A2 Term," *Phys. Rev. Lett.*, vol. 35, no. 7, pp. 432–434, 1975.

[16] V. I. Emeljanov and Y. L. Klimontovich, "Appearance of collective polarisation as a result of phase transition in an ensemble of two-level atoms,

interacting through electromagnetic field," *Phys. Lett. A,* vol. 59, no. 5, pp. 366–368, 1976.

[17] H. J. Kimble and L. Mandel, "Theory of resonance fluorescence," *Phys. Rev. A,* vol. 13, no. 6, p. 2123, 1976.

[18] B. V Thompson, "Soft modes and the counter-rotating terms of the Dicke model," *J. Phys. A. Math. Gen.*, vol. 10, no. 11, p. L179, 1977.

[19] R. Gilmore, "Structural stability of the phase transition in Dicke-like models," *J. Math. Phys.*, vol. 18, pp. 17–22, 1977.

[20] B V Thompson, "A canonical transformation theory of the generalized Dicke model," *J. Phys. A Math. Gen.*, vol. 10, pp. 89–97, 1977.

[21] T. Holstein and H. Primakoff, "Field Dependence of the Intrinsic Domain Magnetization of a Ferromagnet," *Phys. Rev.*, vol. 58, p. 1098, 1940.

[22] D. Tolkunov and D. Solenov, "Quantum phase transition in the multimode Dicke model," *Phys. Rev. B - Condens. Matter Mater. Phys.*, vol. 75, p. 24402, 2007.

[23] N. Bogolubov, "On the theory of superfluidity," *J. Phys.*, vol. USSR, pp. 23–32, 1947.

[24] P. Nataf and C. Ciuti, "No-go theorem for superradiant quantum phase transitions in cavity QED and counter-example in circuit QED.," *Nat. Commun.*, vol. 1, p. 1069, 2010.

[25] D. Hagenmuller, S. De Liberato, and C. Ciuti, "Ultrastrong coupling between a cavity resonator and the cyclotron transition of a 2D electron gas in a semiconductor," *Phys. Rev. B,* vol. 81, p. 235303, 2010.

[26] A. H. Castro Neto, F. Guinea, N. M. R. Peres, K. S. Novoselov, and A. K. Geim, "The electronic properties of graphene," *Rev. Mod. Phys.*, vol. 81, pp. 109–162, 2009.

[27] T. Liu and Q. J. Wang, "Magnetopolariton in bilayer graphene: A tunable ultrastrong light-matter coupling," *Phys. Rev. B - Condens. Matter Mater. Phys.*, vol. 89, p. 125306, 2014.

[28] D. Hagenmüller and C. Ciuti, "Cavity QED of the graphene cyclotron transition," *Phys. Rev. Lett.*, vol. 109, no. 26, p. 267403, 2012.

[29] A. Amo *et al.*, "Collective fluid dynamics of a polariton condensate in a semiconductor microcavity," *Nature,* vol. 457, no. 7227, pp. 291–295, 2009.

[30] S. Information, "Superfluidity of polaritons in semiconductor microcavities," *Nat. Phys.*, vol. 5, no. 11, p. 805, 2009.

[31] J. Kasprzak *et al.*, "Bose-Einstein condensation of exciton polaritons.," *Nature,* vol. 443, no. 7110, pp. 409–414, 2006.

[32] W. H. Nitsche *et al.*, "Algebraic order and the Berezinskii-Kosterlitz-Thouless transition in an exciton-polariton gas," *Phys. Rev. B - Condens. Matter Mater. Phys.*, vol. 90, no. 205430, 2014.

[33] K. S. Daskalakis, S. A. Maier, and S. K??na-Cohen, "Spatial Coherence and Stability in a Disordered Organic Polariton Condensate," *Phys. Rev. Lett.*,

vol. 115, no. 35301, 2015.

[34] D. Sanvitto and S. Kéna-Cohen, “The road towards polaritonic devices,” *Nat. Mater.*, vol. 15, pp. 1061–1073, 2016.

[35] J. L. O’Brien, A. Furusawa, and J. Vučković, “Photonic quantum technologies,” *Nat. Photonics*, vol. 3, pp. 687–695, 2009.

[36] K. Baumann, C. Guerlin, F. Brennecke, and T. Esslinger, “Dicke quantum phase transition with a superfluid gas in an optical cavity,” *Nature*, vol. 464, no. 7293, pp. 1301–1306, 2010.

[37] K. Baumann, R. Mottl, F. Brennecke, and T. Esslinger, “Exploring symmetry breaking at the Dicke quantum phase transition,” *Phys. Rev. Lett.*, vol. 107, no. 140402, 2011.

[38] P. P. Vasil’ev, R. V Penty, and I. H. White, “Pulse generation with ultra-superluminal pulse propagation in semiconductor heterostructures by superradiant-phase transition enhanced by transient coherent population gratings,” *Light Sci. Appl.*, vol. 5, p. e16086, 2016.

[39] B. M. Garraway, “The Dicke model in quantum optics: Dicke model revisited.,” *Philos. Trans. A. Math. Phys. Eng. Sci.*, vol. 369, pp. 1137–1155, 2011.

[40] A. Dreismann *et al.*, “A sub-femtojoule electrical spin-switch based on optically trapped polariton condensates,” *Nat. Mater.*, vol. 15, no. 10, pp. 1074–1078, 2016.

[41] H. Zeng, J. Dai, W. Yao, D. Xiao, and X. Cui, “Valley polarization in MoS2 monolayers by optical pumping,” *Nature Nanotechnology*, vol. 7, no. 8. pp. 490–493, 2012.

[42] H. Yuan *et al.*, “Generation and electric control of spin–valley-coupled circular photogalvanic current in WSe2,” *Nat. Nanotechnol.*, vol. 9, no. 10, pp. 851–857, 2014.

[43] T. Cheiwchanchamnangij and W. R. L. Lambrecht, “Quasiparticle band structure calculation of monolayer, bilayer, and bulk MoS 2,” *Phys. Rev. B - Condens. Matter Mater. Phys.*, vol. 85, p. 205302, 2012.

[44] A. Kormányos, V. Zólyomi, N. D. Drummond, P. Rakyta, G. Burkard, and V. I. Fal’Ko, “Monolayer MoS2: Trigonal warping, the Γ valley, and spin-orbit coupling effects,” *Phys. Rev. B - Condens. Matter Mater. Phys.*, vol. 88, p. 45416, 2013.

[45] K. F. Mak, C. Lee, J. Hone, J. Shan, and T. F. Heinz, “Atomically thin MoS2: A new direct-gap semiconductor,” *Phys. Rev. Lett.*, vol. 105, p. 136805, 2010.

[46] A. Splendiani *et al.*, “Emerging photoluminescence in monolayer MoS2,” *Nano Lett.*, vol. 10, pp. 1271–1275, 2010.

[47] Q. H. Wang, K. Kalantar-Zadeh, A. Kis, J. N. Coleman, and M. S. Strano, “Electronics and optoelectronics of two-dimensional transition metal dichalcogenides,” *Nat. Nanotechnol.*, vol. 7, no. 11, pp. 699–712, 2012.

[48] K. F. Mak, K. L. McGill, J. Park, and P. L. McEuen, “The valley Hall effect

in MoS2 transistors," *Science (80-.).*, vol. 344, no. 6191, pp. 1489–1492, 2014.

[49] G. Aivazian *et al.*, "Magnetic Control of Valley Pseudospin in Monolayer WSe2," *Nat. Phys.*, vol. 11, pp. 148–152, 2015.

[50] A. Srivastava, M. Sidler, A. V Allain, D. S. Lembke, A. Kis, and A. Imamo, "Valley Zeeman effect in elementary optical excitations of monolayer WSe2," *Nat. Phys.*, vol. 11, no. 2, pp. 141–147, 2015.

[51] Y. Li *et al.*, "Valley splitting and polarization by the zeeman effect in monolayer MoSe2," *Phys. Rev. Lett.*, vol. 113, p. 266804, 2014.

[52] D. Macneill *et al.*, "Breaking of valley degeneracy by magnetic field in monolayer MoSe2," *Phys. Rev. Lett.*, vol. 114, p. 37401, 2015.

[53] T. Cao *et al.*, "Valley-selective circular dichroism of monolayer molybdenum disulphide," *Nat. Commun.*, vol. 3, p. 887, 2012.

[54] A. M. Jones *et al.*, "Optical generation of excitonic valley coherence in monolayer WSe2," *Nature Nanotechnology*, vol. 8, no. 9. pp. 634–638, 2013.

[55] J. S. Ross *et al.*, "Electrical control of neutral and charged excitons in a monolayer semiconductor.," *Nature communications*, vol. 4. p. 1474, 2013.

[56] D. Xiao, G. Bin Liu, W. Feng, X. Xu, and W. Yao, "Coupled spin and valley physics in monolayers of MoS2 and other group-VI dichalcogenides," *Phys. Rev. Lett.*, vol. 108, p. 196802, 2012.

[57] X. Liu *et al.*, "Strong light–matter coupling in two-dimensional atomic crystals," *Nat. Photonics*, vol. 9, no. 1, pp. 30–34, 2015.

[58] D. X. and T. F. H. Xiaodong Xu, Wang Yao, "Spin and pseudospins in transition metal dichalcogenides," *Nat. Phys.*, vol. 10, pp. 343–350, 2014.

[59] X. Xu, W. Yao, D. Xiao, and T. F. Heinz, "Spin and pseudospins in layered transition metal dichalcogenides," *Nature Physics*, vol. 10, no. 5. pp. 343–350, 2014.

[60] H. Liu, Y. Du, Y. Deng, and P. D. Ye, "Semiconducting Black Phosphorus: Synthesis, Transport Properties and Electronic Applications," *Chem. Soc. Rev.*, vol. 44, pp. 2732–2743, 2014.

[61] G. Liu, D. Xiao, Y. Yao, X. X. De, W. Yao, and D. Xiao, "Electronic structures and theoretical modelling of two-dimensional group-VIB transition metal dichalcogenides," *Chem. Soc. Rev.*, vol. 44, no. 9, pp. 2643–2663, 2014.

[62] G. Bin Liu, W. Y. Shan, Y. Yao, W. Yao, and D. Xiao, "Three-band tight-binding model for monolayers of group-VIB transition metal dichalcogenides," *Phys. Rev. B - Condens. Matter Mater. Phys.*, vol. 88, p. 85433, 2013.

[63] F. Rose, M. O. Goerbig, and F. Piéchon, "Spin- and valley-dependent magneto-optical properties of MoS2," *arXiv*, vol. 1307.2884v, 2013.

[64] H. Rostami, A. G. Moghaddam, and R. Asgari, "Effective lattice Hamiltonian for monolayer MoS2: Tailoring electronic structure with

perpendicular electric and magnetic fields," *Phys. Rev. B - Condens. Matter Mater. Phys.*, vol. 88, p. 85440, 2013.

[65] D. HAGENMÜLLER, "Doctor thesis," 2012.

[66] C. Lu, G. Li, J. Mao, L. Wang, and E. Y. Andrei, "Bandgap and doping effects in MoS2 measured by Scanning Tunneling Microscopy and Spectroscopy," *arXiv*, vol. 1405.2367, 2014.

[67] P. D. Y. Han Liu, Adam T. Neal, Zhen Zhu, Zhe Luo, Xianfan Xu, David Tomanek, "Phosphorene : An Unexplored 2D Semiconductor with a High Hole Mobility," *ACS Nano*, vol. 8, no. 4, pp. 4033–4041, 2014.

[68] S. Das, M. Demarteau, A. Roelofs, N. Material, H. E. Physics, and U. States, "Ambipolar Phosphorene Field E ff ect Transistor," *ACS Nano*, vol. 8, no. 11, pp. 11730–11738, 2014.

[69] M. Venkata Kamalakar, B. N. Madhushankar, A. Dankert, and S. P. Dash, "Low schottky barrier black phosphorus field-effect devices with ferromagnetic tunnel contacts," *Small*, vol. 11, no. 18, pp. 2209–2216, 2015.

[70] Z. Wang *et al.*, "Black phosphorus nanoelectromechanical resonators vibrating at very high frequencies," *Nanoscale*, vol. 7, no. 3, pp. 877–884, 2015.

[71] H. Liu, Y. Du, Y. Deng, and P. D. Ye, "Semiconducting Black Phosphorus: Synthesis, Transport Properties and Electronic Applications," *Chem. Soc. Rev.*, vol. 44, p. 2732, 2015.

[72] A. N. Rudenko and M. I. Katsnelson, "Quasiparticle band structure and tight-binding model for single- and bilayer black phosphorus," *Phys. Rev. B - Condens. Matter Mater. Phys.*, vol. 89, p. 201408(R), 2014.

[73] Q. Liu, X. Zhang, L. B. Abdalla, A. Fazzio, and A. Zunger, "Switching a normal insulator into a topological insulator via electric field with application to phosphorene," *Nano Lett.*, vol. 15, no. 2, pp. 1222–1228, 2015.

[74] K. Dolui and S. Y. Quek, "Quantum-confinement and Structural Anisotropy result in Electrically-Tunable Dirac Cone in Few-layer Black Phosphorous.," *Sci. Rep.*, vol. 5, no. April, p. 11699, 2015.

[75] X. Y. Zhou *et al.*, "Landau levels and magneto-transport property of monolayer phosphorene," *Sci. Rep.*, vol. 5, p. 12295, 2015.

[76] J. M. Pereira and M. I. Katsnelson, "Landau levels of single-layer and bilayer phosphorene," *Phys. Rev. B - Condens. Matter Mater. Phys.*, vol. 92, p. 75437, 2015.

[77] P. Kumar, B. S. Bhadoria, S. Kumar, S. Bhowmick, Y. S. Chauhan, and A. Agarwal, "Thickness and electric field dependent polarizability and dielectric constant in phosphorene," *Phys. Rev. B*, vol. 93, p. 195428, 2016.

[78] D. Hagenmüller and C. Ciuti, "Cavity QED of the graphene cyclotron transition," *Phys. Rev. Lett.*, vol. 109, p. 267403 (2012), 2012.

[79] B. Li, T. Liu, D. W. Hewak, Z. Shen, and Q. J. Wang, "Ultrastrong light-matter coupling of cyclotron transition in monolayer Mo S2," *Phys. Rev. B*, vol. 93, no. 4, p. 45420, 2016.

[80] R. Roldán, J. N. Fuchs, and M. O. Goerbig, “Spin-flip excitations, spin waves, and magnetoexcitons in graphene Landau levels at integer filling factors,” *arXiv*, vol. 1008.5304v, 2010.

[81] Y. Aharonov and D. Bohm, “Significance of Electromagnetic Potentials in the Quantum Theory,” *Phys. Rev.*, vol. 115, no. 3, pp. 485–491, 1959.

[82] D. Y. Aharonov, Bohm, “Further Considerations on Electromagnetic Potentials in the Quantum Theory,” *Phys. Rev.*, vol. 123, no. 4, pp. 1511–1524, 1961.

[83] and R. B. L. R. A. Webb, S. Washburn, C. P. Umbach, “Observation of h/e Aharonov-Bohm Oscillations in Normal-Metal Rings,” vol. 54, no. 25, pp. 2696–2699, 1985.

[84] A. Bachtold, C. Strunk, J. Salvetat, Â. Forro, T. Nussbaumer, and J. Bonard, “Aharonov Bohm oscillations in carbon nanotubes,” *Nature*, vol. 397, pp. 673–675, 1999.

[85] T. Haug, H. Heimonen, R. Dumke, L.-C. Kwek, and L. Amico, “The Aharonov-Bohm effect in mesoscopic Bose-Einstein condensates,” *arXiv*, p. 1706.05180, 2017.

[86] R. Zhang, Z. Wu, X. J. Li, and K. Chang, “Aharonov-Bohm effect in monolayer phosphorene nanorings,” *Phys. Rev. B*, vol. 95, p. 125418, 2017.

[87] D. Oliveira, J. Fu, L. Villegas-Lelovsky, A. C. Dias, and F. Qu, “Valley Zeeman energy in monolayer MoS2 quantum rings: Aharonov-Bohm effect,” *Phys. Rev. B*, vol. 93, p. 205422, 2016.

[88] P. R. and B. orn T. jorg Schelter, “The Aharonov-Bohm effect in graphene rings,” *arXv*, p. 1201.6200, 2012.

[89] C.-S. Park, “Aharonov–Bohm effect in bilayer graphene,” *Phys. Lett. Sect. A Gen. At. Solid State Phys.*, vol. 381, pp. 1831–1836, 2017.

[90] L. Vaidman, “Role of potentials in the Aharonov-Bohm effect,” *Phys. Rev. A*, vol. 86, p. 040101(R), 2012.

[91] Y. Aharonov, E. Cohen, and D. Rohrlich, “Comment on ‘role of potentials in the Aharonov-Bohm effect,’” *Phys. Rev. A*, vol. 92, p. 26101, 2015.

[92] L. Vaidman, “Reply to a Comment on ‘Role of Potentials in the Aharonov-Bohm Effect,’” *arXiv*, p. 1508.00743, 2015.

[93] Y. Aharonov, E. Cohen, and D. Rohrlich, “Nonlocality of the Aharonov-Bohm effect,” *Phys. Rev. A*, vol. 93, p. 42110, 2016.

[94] Sandu Popescu, “Dynamical quantum non-locality,” *Nat. Phys.*, vol. 6, pp. 151–153, 2010.

[95] A. M. Stewart, “Role of the non-locality of the vector potential in the Aharonov- Bohm effect,” *arXiv*, p. 1209.2050, 2012.

[96] D. Lin, “Partial Wave Analysis of Scattering with Nonlocal Aharonov-Bohm Effect and Anomalous Cross Section Induced by Quantum Interference,” *Phys. Lett. A*, vol. 320, pp. 207–214, 2003.

[97] K. Moulopoulos, “Beyond the Dirac phase factor: Dynamical Quantum

Phase-Nonlocalities in the Schr¨ odinger Picture," *J. Mod. Phys.*, vol. 2, pp. 1250–1271, 2011.

[98] P. Pearle and A. Rizzi, "Quantum Mechanical Inclusion of the Source in the Aharonov-Bohm Effect," *Phys. Rev. A,* vol. 95, p. 52123, 2017.

[99] P. Pearle and A. Rizzi, "Quantized vector potential and alternative views of the magnetic Aharonov-Bohm phase shift," *Phys. Rev. A,* vol. 95, p. 52124, 2017.

[100] K. K. and Y. S. Kim, "Quantization of electromagnetic fields in cavities and spontaneous emission," *Phys. Rev. A,* vol. 50, no. 2, pp. 1830–1839, 1994.